The Astrophysical Journal Supplement Series, 182:143–204, 2009 May doi:10.1088/0067-0049/182/1/143

THE LEGACY OF SCUPOL: 850 μm IMAGING POLARIMETRY FROM 1997 TO 2005

Brenda C. Matthews[1], Christie A. McPhee[1], Laura M. Fissel[1,2], and Rachel L. Curran[3,4]
[1] Herzberg Institute of Astrophysics, National Research Council of Canada, 5071 W. Saanich Road, Victoria, BC V9E 2E7, Canada; brenda.matthews@nrc-cnrc.gc.ca
[2] Department of Astronomy, University of Toronto, 50 St. George St., Toronto, ON M5S 3H4, Canada
[3] Dublin Institute for Advanced Studies, 31 Fitzwilliam Place, Dublin 2, Republic of Ireland
Received 2008 August 12; accepted 2009 March 19; published 2009 April 30

ABSTRACT

SCUPOL, the polarimeter for SCUBA on the James Clerk Maxwell Telescope, was the most prolific thermal imaging polarimeter built to date. Between 1997 and 2005, observations of 104 regions were made at 850 μm in the mapping mode. The instrument has produced ∼50 refereed journal publications, and that number is still growing. We have systematically re-reduced all imaging polarimetry made in the standard "jiggle-map" mode from the SCUBA archive (2800+ individual observations) to produce a catalog of SCUPOL images and tables. We present the results of our analysis with figures and data tables produced for all 83 regions where significant polarization was detected. In addition, the reduced data cubes and data tables can be accessed online. In many cases, the data included in this paper have been previously published elsewhere. However, this publication includes unpublished data sets, in whole or in part, toward 39 regions, including cores in ρ Ophiuchus, Orion's OMC-2 region, several young stellar objects, and the galaxy M87.

Key words: ISM: clouds – ISM: magnetic fields – polarization – stars: formation – submillimeter

Online-only material: machine-readable tables

1. INTRODUCTION

One of the outstanding questions in the study of star formation concerns the relative importance of magnetic fields in the formation and evolution of clouds, cores and finally protostars (see McKee & Ostriker 2007, for a recent theoretical review). Magnetic fields are thought to provide support against gravitational collapse on large scales, even regulating the filamentary structures observed within molecular clouds (e.g., Fiege & Pudritz 2000a; Carlqvist & Kristen 1997; Nakamura et al. 1993). The process of ambipolar diffusion has been proposed to regulate the collapse of dense cores to form protostars (Shu et al. 1987). However, some magnetic field must be retained within the protostellar system, since models predict that protostellar outflows are collimated by magnetic fields (e.g., Pudritz 1985; Uchida & Shibata 1985; Shu et al. 1994; Fiege & Hendricksen 1996) and the final products, stars, have strong magnetic fields.

Thermal emission from aligned, spinning dust grains is anisotropic and hence polarized. Polarization data reveal no direct information about the field strength, since the degree of polarization is dependent on other factors such as grain shape, composition, and degree of alignment. The degree of polarization is in essence a measure of how effectively the grains have been aligned (see Lazarian 2007 and references therein). Even in theories where the aligning mechanism is not the magnetic field (for instance, an isotropic radiation field; Draine & Weingartner 1996, 1997), the grains are still expected to be oriented with their long axes perpendicular to the magnetic field in each grain's vicinity, allowing the use of the measured polarization angle to infer the presence and orientation of the magnetic field.

Continuum polarization data are the principal means of probing the geometry of the magnetic field in star-forming clouds or other dusty systems. Each individual dust grain produces polarized emission perpendicular to its local field direction (Hildebrand et al. 1998). All dust polarization data probe only the plane-of-sky component (denoted $B_\perp$, or B_{pos}) of a three-dimensional magnetic field, but the polarization vectors measured may be either *parallel or perpendicular* to $B_\perp$, depending on whether the polarization data are due to absorption of background light by dust grains ($\lambda < 25$ μm), or thermal emission from the grains themselves ($\lambda > 25$ μm). Hildebrand (1988) contains a thorough review. At far-infrared and submillimeter wavelengths, dust emission is optically thin toward all but the densest cores. Therefore, observed polarized emission represents the vector sum of the radiation contributed by all dust grains through the depth of the cloud along a line of sight.

Where field geometries are simple and the direction of the magnetic field does not vary through the cloud depth, the polarized emission detected is perpendicular to the mean magnetic field and the latter can be inferred simply by rotating the polarization vectors by 90°. If the field has a more complex, nonuniform geometry, then interpretation becomes more difficult. In such cases, it is best to compare directly the polarization maps with polarization patterns predicted from a physical model of a magnetized cloud. For example, the Integral-shaped Filament of Orion A is clearly filamentary, so core models are inappropriate. Fiege & Pudritz (2000a) present a model for a filamentary cloud in which a helical magnetic field threads the filament and plays an important role in determining the radial density structure. This model predicts an r^{-2} density profile, which has been observed in several clouds, including the Integral-shaped Filament (Johnstone & Bally 1999) and several clouds in Cygnus (Lada et al. 1999; Alves et al. 1999). Fiege & Pudritz (2000b) present predicted polarization patterns for cases in which the field is either poloidally or toroidally dominated.

Polarimetry from the far-IR to the submillimeter has progressed with each new generation of detectors. Early work was limited, by detector sensitivity, to observations of bright and/or compact, usually massive, cores (e.g., Hildebrand et al. 1984;

[4] Present Address: Osservatorio Astronomico di Palermo, Piazza del Parlamento 1, 90134 Palermo, Italy.

Flett & Murray 1991; Greaves et al. 1994; Holland et al. 1996; Dotson et al. 2000; Matthews 2005). SCUPOL represented a step forward due to its imaging capability at 850 μm, a wavelength readily accessible from the ground. This paper summarizes the vast majority of observations made with SCUPOL over its lifetime, with the exception of photometric and raster map observations. In total, over 2800 individual observations were analyzed for this catalog. The observational summary and data reduction are described in Section 2, along with a description of potential planetary calibration. The results of our analysis for each region are presented in Section 3. The instructions for obtaining the reduced data cubes online for independent analysis are described in Section 4 along with recommendations for such use as well as that of included data tables. We summarize the results of the project in Section 5.

2. OBSERVATIONS AND DATA REDUCTION

2.1. SCUPOL Observations

The observations summarized in this paper span the entire operational period of the SCUBA polarimeter, SCUPOL (Greaves et al. 2003; Jenness et al. 2000), which was commissioned on the James Clerk Maxwell Telescope (JCMT) in 1997 and was used until the retirement of the SCUBA camera in 2005 July. Although SCUBA simultaneously observed at 850 and 450 μm (Holland et al. 1999), use of the 450 μm polarimetry data was minimal, in part due to the stricter weather requirements to obtain useable data ($\tau_{225} < 0.05$) and the absence of full characterization of the short-wavelength array for instrumental polarization effects. We include only 850 μm data in this paper.

Here we present a re-reduction of all 850 μm observations obtained with SCUPOL in the "jiggle-mapping" imaging mode, as obtained from the JCMT Archive.[5] The observations are summarized in Table 1. The science targets are listed in order of increasing right ascension, and include the SCUBA archive names, reference positions of the reduced maps, the dates observed, and the number of observations deemed useable, bad (i.e., incomplete, corrupted, or nonstandard/unprocessible) and unusable due to unstable sky opacity over the period of observation. Toward some targets, both photometry and imaging SCUPOL data exist; data obtained in a photometry mode (i.e., undersampled with variable noise across the array) are *not included* in this analysis. The science targets are classified into one of the following categories: Bok globule (BG), starless or prestellar core (SC/PC), star-forming region (SFR), young stellar object (YSO), post-asymptotic giant branch star (AGB), planetary nebula (PN), supernova remnant (SNR), external galaxy (GAL), or the Galactic center (GC).

Maps made with the "jiggle-mapping mode" yielded fully sampled maps for all 37 long-wavelength bolometers by executing a 16-point jiggle pattern within the area of the array with approximately 6″ spacing (Holland et al. 1999).[6] In order to remove sky noise and atmospheric emission from observations, chopping and nodding techniques were used (Holland et al. 1999; Greaves et al. 2003; Zemcov et al 2005). Chopping was done by pointing the telescope on and off the source (ideally onto "empty" sky) at a frequency of 7.8 Hz. The off-source signal is subtracted from the on-source signal. The length of the chop, called the chop throw, is typically 30, 45, 60, 90, or 120 arcsec, with a maximum possible chop throw of 180 arcsec. Selection of chop throws vary for the observations in the archive, particularly due to the varying levels of surrounding extended structure for different sources. The effect on the beam and flux calibration factors for different throws was summarized for SCUBA by Jenness et al. (2002). Nodding refers to the technique of switching the position of the source in the chop pattern, resulting in a mean off-position taken on either side of the pointing center of each observation. Chopping occurs continually and both nod positions are used for each point in the 16-point jiggle pattern, for a total of 32 measurements. For polarimetry observations this sequence must be completed for each of 16 waveplate angles (from 0° in steps of 22.°5), sampled in a step-and-integrate approach (Greaves et al. 2003). A full polarization observation (one rotation of the waveplate) required 12 minutes of observing time, including overheads (i.e., plate rotation).

2.2. Data Reduction

We have reduced the data using the Starlink software packages SURF, KAPPA, POLPACK, and CURSA. POLPACK is designed specifically for polarization data obtained with bolometric arrays. The data reduction includes the standard dual-beam combination, extinction corrections, and flatfielding required for all SCUBA data. For extinction correction, we used 225 GHz tau measurements of zenith opacity from the Caltech Submillimeter Observatory (CSO) as modeled to extrapolate the 345 GHz tau values (Jenness et al. 2002). These are least squares polynomial fits to CSO tau measurements using the lowest polynomial order that gives a satisfactory result. For those observations for which no fit was possible, the sky opacity was deemed unstable, and the science data associated with these periods are not included in further processing. The data omitted may still be useable, and in some cases, are included in existing publications, but would require too much individual assessment to meet the requirements of this systematic re-reduction.

Different relations are used to derive the 345 GHz tau values from the fitted CSO values depending on the SCUBA filters used for the observations. In 2000, "wide" filters were installed in addition to the "narrow" bandpass filters with which SCUBA had been commissioned. The filter profiles are compared by Archibald et al. (2002). During the period from 1999 December 25 to 2000 October 25 observations could be taken with either the narrow or the wide filters; later data sets use the "wide" filters exclusively. The tau relations for the two filters differ and are summarized in Archibald et al. (2002). Using derived tau values for 345 GHz, the data were extinction corrected.

We were very aggressive in the removal of noisy bolometers from the individual SCUPOL observations. The choice of noisy bolometers was an interactive process involving noise observations of the array. Noise observations repeatedly measure the mean and variance of the chop and internal calibrator signals for each bolometer while the detector is looking at a cold load. The noise measurement is the rms level for each pixel after 64 s of integration time. All bolometers with an rms level near or above the ∼100 nV were removed. Also, any bolometers which had an rms obviously larger than the majority of the bolometers was typically removed. The noise in the array can change over the course of a single observing night, so bolometers found to be noisy at any time of night were often flagged over the whole night, as well as additional bolometers which were noisy in individual observations. Our systematic approach of re-reducing all data sets sequentially allowed trends in poor bolometer

[5] The JCMT archive is maintained by the Canadian Astronomy Data Centre.

[6] Large raster, also known as "scan" or "on-the-fly" SCUPOL maps do exist in the archive but are not included in our analysis. There are inherent, systematic uncertainties in extracting the Stokes parameters from these data, and they were ultimately deemed unquantifiable.

Table 1
Summary of Science Targets

Source/ Region	Object[a] Type	SCUBA Archive Name(s)	Coordinates of (0,0) pixel R.A. (J2000)	Decl. (J2000)	Date(s) Observed[b] (YYYYMMDD)	Used Obs.	Bad/N-S Obs.	Unstable tau
CB 3	BG	cb3	00 28 42.10	+56 41 59.9	19980810	1	0	0
L1287	SC/PC	l1287	00 36 47.00	+63 28 52.1	19990706	3	0	0
W3	SFR	w33	02 25 35.44	+62 06 16.4	19980718, 19980719, 20010804	13	0	0
W3 North	SFR	w3_n	02 26 53.00	+62 16 05.0	20010805	9	0	0
W3 OH	SFR	w3_oh	02 27 03.83	+61 52 24.8	20010804	5	0	0
AFGL 333	SFR	afgl333	02 28 08.81	+61 29 25.0	20010804, 20010805	29	0	0
GL 437	SFR	gl437	03 07 24.28	+58 30 46.9	20001010	5	0	0
L1448	YSO	l1448, l1448c	03 25 38.80	+30 44 05.4	20000103*, 20000224, 20030109, 20030111, 20030112, 20030203, 20030213, 20031212, 20031215	51	23	7
L1455	SFR	l1455	03 27 41.31	+30 12 39.4	20030109, 20030112, 20030203, 20030206, 20031214	52	15	0
NGC 1333	SFR	ngc1333,ngc1333_iras4b, ngc1333-iras	03 29 11.11	+31 13 20.2	19991224, 20000224, 20000823, 20000825, 20011224, 20011231, 20020101	72	4	0
IRAS 03282+3035	YSO	iras03282+30	03 31 20.94	+30 45 32.0	20030109, 20030111, 20030112	18	0	0
Barnard 1	SFR	b1	03 33 17.88	+31 09 32.9	19991011*, 19991012, 19991013	34	0	24
HH211/IC348	SFR	hh211,ic348	03 43 56.70	+32 00 51.9	20011224, 20011229, 20020101	72	0	0
CB 17	BG	cb17	04 04 37.99	+56 56 41.1	19980811	1	0	0
L1498	SC/PC	l1498	04 10 52.60	+25 10 00.0	19990914, 19990915, 20040202	46	2	0
L1551	YSO	l1551irs5,l1551ne	04 31 34.14	+18 08 05.1	19980906, 19980908	11	0	0
L1527	YSO	l1527	04 39 53.90	+26 03 10.0	1990901, 19990916, 20000118, 20011224, 20011229, 20021003, 20030203, 20030206, 20030211, 20030213, 20030302, 20030315, 20031214, 20031215	91	14	0
IRAM 04191+1522	YSO	iram04191	04 21 56.91	+15 29 46.1	20020930, 20021001, 20021002	75	3	0
L1517B	SC/PC	l1517b	04 55 16.50	+30 37 03.9	19990913, 19990914, 19990915, 20040202, 20040203	41	0	0
CB 26	BG	cb_26	04 59 50.19	+52 04 45.3	19980811, 20000303, 20000304	25	2	0
L1544	SC/PC	l1544	05 04 17.23	+25 10 43.7	19990913, 19990915, 19990916	48	1	0
RNO 43	SFR	rno43	05 32 19.41	+12 49 41.8	19990916, 2000118	12	0	0
Crab Nebula	SNR	crab,taurusa	05 34 30.50	+22 01 00.0	19971028, 20000104	5	3	0
OMC-1	SFR	omc1,omc1_ne2,omc1nz	05 35 14.5	−05 22 33.0	19990114, 19990122, 19990123, 20000104, 20020301	34	0	0
OMC-2 & OMC-3	SFR	omc3-mms6, omc3-mms1, omc3-mms7, omc3-mms8, omc2_-_p1, omc2_-_p2, omc2_-_p3, omc2_-_p4, omc2_-_p5, omc2_-_p6, omc2_-_p7	05 35 26.9	−05 09 58	19980905, 19980906, 19980907, (20030924), (20030925), (20030926), (20030927), (20030928), (20030929), (20030930), (20031001), 20040914, 20040917, 20040918, 20040919, 20040920, 20040921, 20041021, 20050116	161	152[c]	0
VLA1 IRS2	YSO	hh1_2vla1	05 36 23.19	−06 46 08.9	20000220	5	1	0
NGC 2024	SFR	n2024n, n2024s	05 41 44.08	−01 55 49.6	19980908	12	0	0
LBS 23	SFR	lbs23n, lbs23s	05 46 08.22	−00 10 43.7	19980907, 19980908, 20020912, 20020918	47	0	0
NGC 2068	SFR	obfil	05 46 37.64	+00 00 33.1	19991011*, 19991012, 19991013, 19991014, 19991015, 19991016, 20000218, 20000223	111	2	6
CB 34	BG	cb34	05 47 02.13	+21 00 10.2	19980810	1	0	0
NGC 2071 IR	SFR	ngc2071ir	05 47 04.85	+00 21 47.1	19980907	6	0	0
HH 111	YSO	hh111	05 51 46.23	+02 48 26.7	20000220	4	0	0
IRAS 05490+2658	SFR	iras_05490+2	05 52 13.24	+26 59 33.3	20031223	9	0	0
Mon R2 IRS	SFR	monr2	06 07 46.16	−06 23 22.5	19990620, 20000104	6	1	0
IRAS 06381+1039	SFR	monir27	06 40 58.10	+10 36 37.8	19991016, (20020305)	2	16	0
MON IRAS 12	SFR	iras12, monir12	06 41 05.81	+09 34 09.0	19991011*, 19991012, 20020301, 20020305	19	0	2

Table 1
(Continued)

Source/ Region	Object[a] Type	SCUBA Archive Name(s)	Coordinates of (0,0) pixel R.A. (J2000)	Decl. (J2000)	Date(s) Observed[b] (YYYYMMDD)	Used Obs.	Bad/N-S Obs.	Unstable tau
CB 54	BG	cb_54	07 04 21.07	−16 23 20.09	19980810, 20000306	16	1	0
IRAS 08076-3556	SFR	dc_253.3-1.6	08 09 34.12	−36 05 13.4	20000301, 20000305	24	0	0
IRC +10216	AGB	irc+10216	09 47 57.38	+13 16 43.7	20001210, 20010930, 20050116	18	0	0
M82	GAL	M82	09 55 52.23	+69 40 47.1	(19980214), 19981229, 19990419, 19990420	36	28	0
M87	GAL	m87	12 30 49.45	+12 23 28.2	(19971028), 19981123	7	4	0
L183	SC/PC	l183	15 54 08.96	−02 52 43.9	19990314, 19990315, 20020214, 20020215, 20020216, 20020217	128	1	0
ρ Oph A	SFR rhoopha2, rhoopha3, vla1623	lfam1, rhoopha1,	16 26 26.45	−24 24 10.9	19980514, 19990329, 19990330, 19990331, 19990827*, 19990831*, 20010731, 20010901	55	0	15
ρ Oph C	SFR	rhoophc	16 27 00.10	−24 34 26.7	19990331, 19990401, 19990828*, 19990829*, 19990831*	7	1	24
ρ Oph B2	SFR	rhoophb, b2mms8a, b2mms8b, b2mms8c	16 27 27.97	−24 27 06.8	19990329, 19990330, 19990414	38	0	0
IRAS 16293-2422	YSO	16293-2422	16 32 22.91	−24 28 35.5	19980514, 19990314, 19990315, 19990827*, 19990829*	4	2	12
L43	SC/PC	l43	16 34 35.57	−15 47 00.6	19990314, 19990315	29	0	0
CB 68	BG	bok068p	16 57 19.60	−16 09 22.7	20000602	9	0	0
NGC 6302	PN	ngc_6302	17 13 44.40	−37 06 11.1	20050510	5	0	0
NGC 6334A	SFR	ngc6334a	17 20 19.55	−35 54 42.3	19990620, 19990705, 19990706	7	1	0
Galactic Center	GC	gc, gc-beampos2, gc-beampos3, gc-beampos4, gc-beampos5, gc-beampos6, gc-beampos7, gcpol1, gcpol2, gcpol3, gcpol4, gcpol5, gcpol6, gcpol7, gcpol8, skypos	17 45 39.8	−29 00 26	19990325, 19990326, 19990330, 19990331, 19990827, 19990828*, 19990829*, 20010805, 20030907[d], 20030908*[d]	69	0	36
G011.11-0.12	SFR	gg11.11-0.12p, 11.11p6p7, g11.11p1	18 10 33.99	−19 21 36.9	19990913[e], 20030415, 20030420, 20030816, 20030817, 20030906, 20030928, 20030929	89	9	0
GGD 27	SFR	ggd27	18 19 12.00	−20 47 30.9	19980516	8	0	0
CRL 2136 IRS 1	YSO	gl2136	18 22 26.48	−13 30 15.1	19990706	6	0	0
Serpens Main Core	SFR	smm1_9,smm234	18 29 49.34	+01 15 54.6	19990420	24	1	0
CL 04/CL 21	SFR	cl04/cl21	18 37 19.39	−07 11 31.8	20030417, 20030420	20	0	0
G28.34+0.06[e]	SFR	g28.34p2,g28.34p1p6, g28.34p2fil	18 42 52.40	−03 59 53.9	19990912, 19990913, 19990915, 19990916	30	7	0
IRAS 18437-0216	SFR	iras_18437-0	18 46 23.23	−02 13 45.4	20030831*, 20050604	9	0	9
W48	SFR	w48	19 01 45.45	+01 13 04.5	19990620	8	0	0
R Cr A	SFR	rcra	19 01 53.65	−36 57 07.5	19990705	5	0	0
W49	SFR	w49n,w49se	19 10 13.60	+09 06 17.4	19980516	12	0	0
W51	SFR	w51	19 23 42.00	+14 30 33.0	20001006	6	0	0
B335	BG	b_335	19 37 01.13	+07 34 10.9	19990827*, 19990828*, 20010911, 20010912	27	0	11
IRAS 20081+2720	SFR	iras_20081+2	20 10 13.99	+27 28 36.9	20030830*, 20040604	5	0	9
IRAS 20126+4104	SFR	20126+4104	20 14 26.04	+41 13 32.5	19990706	8	0	0
AFGL 2591 IRS	YSO	gl2591	20 29 24.72	+40 11 18.9	19990706, 20001010	12	0	0
IRAS 20188+3928	SFR	20188+3928	20 20 38.75	+39 38 03.9	19990620, 19990705	9	1	0
S106	SFR	s106-z-1	20 27 17.32	+37 22 41.3	20021002, 20021003, 20021006	28	1	0
G079.3+0.3[e]	SFR	g79.3p2	20 32 23.62	+40 19 44.0	19990912, 19990913, 19990916	14	1	0
DR 21	SFR	dr21,w75,dr21-oh1-z	20 39 01.50	+42 19 38.0	19971028, 19980514, 20000602, 20001010, 20010802*, 20010805, 20021002, 20021006	29	5	5
G81.56+0.10[e]	SFR	g81.50pol	20 40 33.5	+41 59 00.0	19990912, 1990913, 19990915, 19990916	23	0	0
CRL 2688	AGB	crl2688	21 02 18.80	+36 41 38.0	20001007, 20050510	15	0	0
NGC 7027	PN	ngc_7027	21 07 01.59	+42 14 10.2	20001007, 20001010, 20050510	26	0	0

Table 1
(Continued)

Source/ Region	Object[a] Type	SCUBA Archive Name(s)	Coordinates of (0,0) pixel R.A. (J2000)	Coordinates of (0,0) pixel Decl. (J2000)	Date(s) Observed[b] (YYYYMMDD)	Used Obs.	Bad/N-S Obs.	Unstable tau
CB 230	BG	cb_230	21 17 39.39	+68 17 31.9	19980810, 20010910	22	1	0
S140	SFR	s140	22 19 18.00	+63 18 49.0	20001006	6	0	0
S146	SFR	s146	22 49 28.56	+59 55 08.6	19990620, 19990705	14	0	0
Cepheus A	YSO	cepa	22 56 17.80	+62 01 49.0	19980516	8	0	0
Cepheus E	YSO	cepa	23 03 12.80	+61 42 25.0	20001006	4	0	0
S152	SFR	s152	22 58 50.14	+58 45 01.0	20001006	9	0	0
NGC 7538	SFR	ngc7538	23 13 45.54	+61 27 35.7	19980514, 19980718	11	1	0
S157	SFR	s157	23 16 04.00	+60 02 06.0	20001010	5	0	0
Cas A	SNR	casa1, casa3	23 23 10.70	+58 48 44.0	20041017, 20041018	8	2	0
CB 244	BG	cb_244	23 25 46.26	+74 17 38.2	19980810, 20010913, 20010914	34	0	0
Nondetections								
Perseus 5	SFR	per5	03 29 48.23	+31 39 26.1	20000224	2	0	0
Perseus 7	SFR	per7	03 32 16.79	+30 56 28.5	20000224	1	0	0
DG Tau	YSO	dgtau	04 27 04.68	+26 06 16.2	19980719	1	0	0
Elias 16	YSO	elias16, e16_ridge,elias16_ridg	04 39 36.67	+26 11 50.6	19990909, 20000118	35	0	0
CRL 618	AGB	crl618	04 42 53.60	+36 06 53.7	(19980811), 19990706, 20000104, 20000118, 20031223	5	2	0
Elias 24	YSO	el24	16 26 22.42	−24 16 13.2	20010731*, 20010901	4	0	3
NGC 6334	SFR	ngc6334	17 17 13.00	−35 48 23.9	20030816, 20030909*	5	0	10
NGC 6537	PN	ngc_6537	18 05 13.20	−19 50 34.1	20050510	5	0	0
GF9	SFR	gf9	20 49 28.60	+60 13 20.3	19980720	2	0	0
CB 243	BG	cb243	23 25 05.73	+63 36 33.6	19980810	1	0	0
No Good Data								
CB 4	BG	cb4	00 39 04.13	+52 51 58.5	(19980810)	0	1	0
CB 16	BG	cb16	04 03 16.37	+56 50 56.2	(19981810)	0	1	0
GM Aur	YSO	gm_aur	04 55 11.00	+30 22 01.3	(19980831)	0	1	0
CB 24	BG	cb24	04 58 29.67	+52 15 54.0	(19980811)	0	1	0
CB 25	BG	cb25	04 59 03.13	+52 03 51.6	(19980811)	0	1	0
AS205	YSO	as205	16 11 31.40	−18 38 25.0	20010731*	0	0	5
L1709B	YSO	l1709b	16 31 35.83	−24 01 28.1	20010731*	0	0	4
L483	YSO	l483	18 17 31.49	−04 39 13.1	19990827*	0	0	8
L723	YSO	l723	19 17 53.86	+19 12 18.6	19990829*	0	0	5
L1157	YSO	l1157	20 39 06.54	+68 02 13.4	19990828*, 19990829*	0	0	14
IRAS 22551+6221	SFR	iras_22551+6	22 57 08.57	+62 37 41.4	20030830*	0	0	5

Notes.

[a] Objects have been categorized as BGs, SC/PCs, SFRs, YSOs, SNRs, GALs, PNe, post-AGB stars, or the GC.

[b] Dates marked with an asterisk had no CSOFIT solution and are deemed to have unstable tau. Dates in parentheses indicate no useable data for that date for reasons other than the tau solutions.

[c] All observations between 20030924 and 20031001 (150) were bad due to the attempt to use a depolarizer which causes vignetting of the beam.

[d] These observations of the GC were taken in a nonstandard mode during testing of a new large-scale mapping technique. The observations were never completed. Due to the deliberate chopping onto emission during these observations, we have opted not to include these data in the final map.

[e] Observations are part of the project M99BC20. The data for this project were taken during a period of dish adjustment at the JCMT. As a consequence, the dish shape was changing each day, and it is possible that the shape of the sidelobes was also changing. The effect on the main beam of the antenna is not established, so these data should be treated with caution. This is the first appearance of these data in the literature, but they are included for completeness, and perhaps may be useable to inform future work in the region.

Table 2
Noisy Bolometers

Date[a]	Noisy bolometers[b]
1997 Oct 28	6,9,13,23,29,35
1998 Feb 14	9,14,22,23
1998 Mar 3	10,35
1998 May 14	10,14,30
1998 May 16	10,14,30,37
1998 Jul 18	9,14,30,(31),36,37
1998 Jul 19	9,10,14,22,30,31,37
1998 Jul 20	9,10,14,22,23,30,37
1998 Aug 10	9,14,17,28,30,35,37
1998 Aug 11	9,10,14,28,30,37

Notes.
[a] An asterisk indicates data from this date does not yield a fit to the CSO tau data; these have not been reduced or compiled with the rest of the data.
[b] Parentheses indicate bolometers removed for only parts of a night.
(This table is available in its entirety in a machine-readable form in the online journal. A portion is shown here for guidance regarding its form and content.)

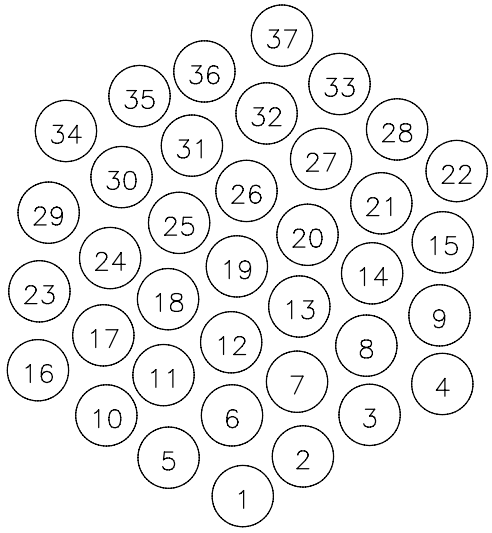

Figure 1. Arrangement of bolometers across the 850 μm SCUBA detector array.

performance to be noted and those bolometers removed. Table 2 is a summary of the bad bolometers chosen for each date. This information can inform comparisons of our data reduction with pre-existing or subsequent analysis. Figure 1 shows the arrangement of bolometers across the long-wavelength array. The increasing number of flagged bolometers over time reflects the aging of the SCUBA instrument which resulted in significantly noisier performance in the final two years of its lifetime.

The high number of individual observations, in many cases observed on multiple nights, toward many regions produced by combining all the data means that even after flagging, few or no holes remain in the final maps. Since SCUBA sat at the Nasmyth platform at the JCMT, sky rotation ensures that different bolometers observe each sky position as observations progress, mitigating the effects of individual bad bolometers. Minimizing noise was favored over avoiding holes in the final, gridded, polarization vectors.

At submillimeter wavelengths, the sky is highly variable on timescales of less than a second. This variability must be measured and removed from the data. Chopping removes the effects of slow sky variability; however, fast variations remain in the data. Subtraction of sky variations on timescales shorter than the chop duration was done using data from off-source bolometers within individual observations, which we call "sky" bolometers. The methods are discussed in detail by Jenness et al. (1998). The sky bolometers are selected to have negligible, preferentially positive emission, requiring active inspection of each individual observation. In order to subtract the sky variations, the average of all designated sky bolometers is taken for each 1 s time interval and subtracted from each bolometer in the map. The mean of the sky bolometers (averaged over all 1 s time intervals) was added back into the map in order to conserve the flux level in case bolometers contained some emission (positive or negative). Typically one to four sky bolometers was used (although the entire outer ring can be used in the case of compact sources). In areas of extended emission such as the Orion A filament and the GC it is extremely difficult to chop onto areas empty of emission, even with the largest allowable chop throw of 3 arcmin, and somewhat negative bolometers sometimes were used.

Matthews et al. (2001a) show that the removal of sky noise is a critical step in deriving accurate results for polarimetry data. Even use of a single reasonably empty bolometer produces better results for individual observations than using a high number of bolometers which are not optimal. In the latter case, sky removal is imperfect and will result in individual observations which have a high degree in variation in polarization signal. When these maps are combined, the result will be diminished or negligible polarization because the vector sum will go to zero. The instrumental polarization was removed using the measured values from 1997, as described in Greaves et al. (2003).

Finally, the individual observations toward targets or regions were combined to create composite Stokes I, Q, and U maps. This is done by fitting a sinusoid to the intensity measurements from each set of pixel measurements at each wave plate position in order to fit for I, Q, and U from which the polarization percentage, p, and the position angle can be deduced. The data were sampled on a $10''$ pixel^{-1} grid in J2000 coordinates. We used a Gaussian kernel to generate grid maps of the polarization data. This is a good compromise when the mapped area is not densely sampled, but it does require smoothing of the data to effectively sample the grid. After smoothing with a $14''$ gaussian, the effective beamwidth in the maps is $20''$, larger than the $14''$ diffraction limit of the JCMT at 850 μm. The resultant maps therefore represent Nyquist sampling of the smoothed data. For some data sets, better resolution can be obtained with a different regridding kernel. We binned data by a factor of 2 (i.e., to a $20''$ grid) only when this significantly improved the representation of the data quality in the final map. Only maps in which significant vectors were detected in the raw $10''$ pixel^{-1} map were subject to binning (i.e., we do not present binned maps if the binning was required to produce a significant vector).

The fitting of a sinusoid to the intensity measurements as a function of waveplate angle also permits an internal estimation of errors by comparison of equivalent waveplate positions (i.e., 0, 90, 180, and 270° waveplate positions all measure a position angle of 0° on the sky). Once I, Q, and U are known, the polarization percentage, p, and the position angle θ can be deduced. A θ value of 0° indicates north and angles increase east of north.

Table 3
Planetary Observations Summary

Planet	Dates Observed (YYYYMMDD)	Number of Used Observations	Number of Bad/N-S Observations
Mars	(19980515), 19981123, (19990326), 19990419, 19990513, (19990912), (19990913), 20000224, 20010913, 20010914, 20020301	8	7
Jupiter	(19971027), 19981121*, (19990329), 19991011*, 19991012, 20000103*, 20000719, 20000823, 20000825	7	6
Saturn	19980831, (19990829), 19990909, 19990914, 19991013, 19991014, 19991016, (19991224), 20000218, 20000220, 20000223, 20000224, (20001116*), 20011224	15	4
Uranus	(19980302), (19980516), 19980719, (19980810), (19980811), 19990314, 19990315, (19990329), 19990330, 19990420, (19990620), 19990827*, 19990828*, (19990912), (19990913), (19990915), (19990916), 20000823, 20011229, (20011228), 20020217, (20020811), (20020816), 20030417, 20041017	19	13

Notes. Dates marked with an asterisk have no tau fits; these data may be alright, but we have not included them in our reduction. Dates in parentheses contain irreducible (i.e., bad or nonstandard) data.

The raw polarization percentage and the uncertainty in polarization percentage are calculated from the expressions

$$p' = \frac{\sqrt{Q^2 + U^2}}{I} \times 100\% \quad (1)$$

$$dp = p'^{-1} \sqrt{(dQ^2\, Q^2 + dU^2\, U^2)} \quad (2)$$

since the dI term ($\propto I^{-6}$) is negligible.

A bias exists that tends to increase the polarization percentage value, even when Q and U are consistent with a value of zero because polarization percentage is forced to be positive (Vaillancourt 2006). Therefore, its value is typically "debiased" in the following manner to produce the final polarization percentage, p:

$$p = \sqrt{p'^2 - dp^2}. \quad (3)$$

The position angles can then be calculated by the following relations:

$$\theta = \frac{1}{2}\, tan^{-1} \frac{U}{Q} \quad (4)$$

$$d\theta = \frac{180^\circ}{\pi \times \sigma_p}, \quad (5)$$

where σ_p is the ratio of p to dp. Note that the position angles can take on any value, but in measurements of linear polarization, values different by 180° are identical to each other.

2.3. Calibration with Planetary Polarization Data

Although absolute flux calibration is not essential to measurements of polarization in astronomical sources, planetary observations serve two purposes in the analysis of polarization data. The first purpose is to provide a check that the instrumental polarizations are effectively being removed, since planets should not be inherently polarized in thermal emission at 850 μm (an exception is Saturn due to the presence of its rings). The second purpose is to enable a measure of the relative beam response from the peak to anywhere else on the array as well as the relative polarization in the sidelobe relative to the peak after instrumental polarization removal. These quantities are needed to assess the minimum believable polarization in science observations. If strong sources exist off the array center (for example, at the location of a strong sidelobe), then these can produce a polarization signal at the array center (in the main beam). The method for assessing the scale of this error is described in Greaves et al. (2003).

In Tables 3 and 4, we show a compiled list of all the planetary polarization data taken with SCUBA in the jiggle-mapping mode. Calibration data do not exist for all dates when SCUPOL science data were taken. For such dates, the closest available observation in time could be used. The specific ratios of flux and polarization response should be taken from the planetary maps at the radius from beam center where the brightest off-center source is located, since this will provide the maximum artifact signal which can be present in each science map.

3. RESULTS

Table 1 summarizes the SCUPOL observations of science targets in the jiggle-map mode. Sources with detections, nondetections and for which all data are of bad or nonstandard quality are included in the table, for completeness. The right ascension and declination of the (0,0) pixel correspond to the reference coordinates used during reduction of the data and are generally the pointing center of at least one observation, or a bright source in the region. We include all maps for regions with detections (Figures 2–84) as a resource for future users of the archival data.

Table 5 is a compilation of information about regions toward which we have detected polarization. The table lists the figure number, the distance to the object/region, whether it is a first publication of any part of the SCUPOL data set, previous SCUPOL publication(s) and publications of thermal emission polarization data from other facilities or instruments, where applicable.

Table 4
Planetary Observations with SCUPOL by Date

Year	Date	Planet	No. of Observations[a]	Reference Position	
				R.A. (J2000)	Decl. (J2000)
1997	28 Oct	Jupiter	(4)	No map created.	
1998	2 Mar	Uranus	(1)	No map created.	
	15 May	Mars	(1)	No map created.	
	16 May	Uranus	(1)	No map created.	
	19 Jul	Uranus	2	20 56 03.58	−18 01 24.6
	10 Aug	Uranus	(1)	No map created.	
	11 Aug	Uranus	(1)	No map created.	
	31 Aug	Saturn	1	02 08 26.81	+10 09 42.6
	21 Nov[b]	Jupiter	1	No map created.	
	23 Nov	Mars	1	11 15 17.08	+02 18 34.1
1999	14 Mar	Uranus	1	21 10 43.36	−16 56 28.1
	15 Mar	Uranus	1	21 10 54.90	−16 55 38.6
	26 Mar	Mars	(1)	No map created.	
	29 Mar	Uranus	(3)	No map created.	
		Jupiter	(2)	No map created.	
	30 Mar	Uranus	5,(1)	21 13 33.23	−16 44 20.1
	19 Apr	Mars	2	14 16 56.3	−12 05 07.8
	20 Apr	Uranus	1	21 16 17.46	−16 32 44.7
	13 May[d]	Mars	1	13 43 34.0	−10 07 53.0
	20 June	Uranus	(1)	No map created.	
	27 Aug[b]	Uranus	2	No map created.	
	28 Aug[b]	Uranus	2	No map created.	
	29 Aug	Saturn	(2)	No map created.	
	9 Sep	Saturn	1	03 01 25.1	+14 31 40.9
	12 Sep	Mars	(2)	No map created.	
		Uranus	(2)	No map created.	
	13 Sep	Mars	(3)	No map created.	
		Uranus	(1)	No map created.	
	14 Sep	Saturn	1	03 00 59.08	+14 28 45.4
	15 Sep	Uranus	(2)	No map created.	
	16 Sep	Uranus	(3)	No map created.	
	11 Oct[b]	Jupiter	1	No map created.	
	12 Oct	Jupiter	1	01 59 18.34	+10 31 31.8
	13 Oct	Saturn	2	02 55 24.81	+14 00 00.2
	14 Oct	Saturn	1	02 55 08.96	+13 58 45.2
	16 Oct	Saturn	1	02 54 35.66	+13 56 08.5
	24 Dec	Saturn	(1)	No map created.	
2000	3 Jan[b,e]	Jupiter	4	No map created.	
	18 Feb	Saturn	1	02 39 14.35	+13 11 15.2
	20 Feb	Saturn	1	02 39 45.05	+13 14 11.9
	23 Feb	Saturn	1	02 40 32.65	+13 18 41.6
	24 Feb	Mars	1	00 34 27.37	+03 18 37.5
		Saturn	1	02 40 49.78	+13 20 17.6
	19 Jul[c]	Jupiter	2	04 07 54.98	+20 04 36.4
	23 Aug	Uranus	1	21 24 06.46	−16 01 39.0
		Jupiter	2	04 30 02.44	+20 56 19.0
	25 Aug	Jupiter	2	04 30 56.87	+20 58 07.2
	16 Nov[b]	Saturn	(1)	No map created.	
2001	13 Sep	Mars	1	18 10 32.91	−26 44 37.7
	14 Sep	Mars	1	18 13 01.80	−26 42 25.5
	24 Dec	Saturn	4	04 33 51.83	+20 06 44.9
	28 Dec	Uranus	(1)	No map created.	
	29 Dec	Uranus	2	21 39 36.63	−14 44 29.9
2002	17 Feb	Uranus	2	21 50 13.12	−13 49 58.9
	1 Mar	Mars	1	01 50 05.21	+11 36 02.5
	11 Aug	Uranus	(1)	No map created.	
	16 Aug	Uranus	(1)	No map created.	
2003	17 Apr	Uranus	2	22 16 09.55	−11 31 33.2
2004	17 Oct	Uranus	2	22 21 11.18	−11 07 00.0

Notes.
[a] Parentheses indicate bad/nonstandard data, not reduced. [b] No tau fit solutions for this date. [c] Off-source pointing. [d] Nonstandard Observation. [e] Several chop throws.

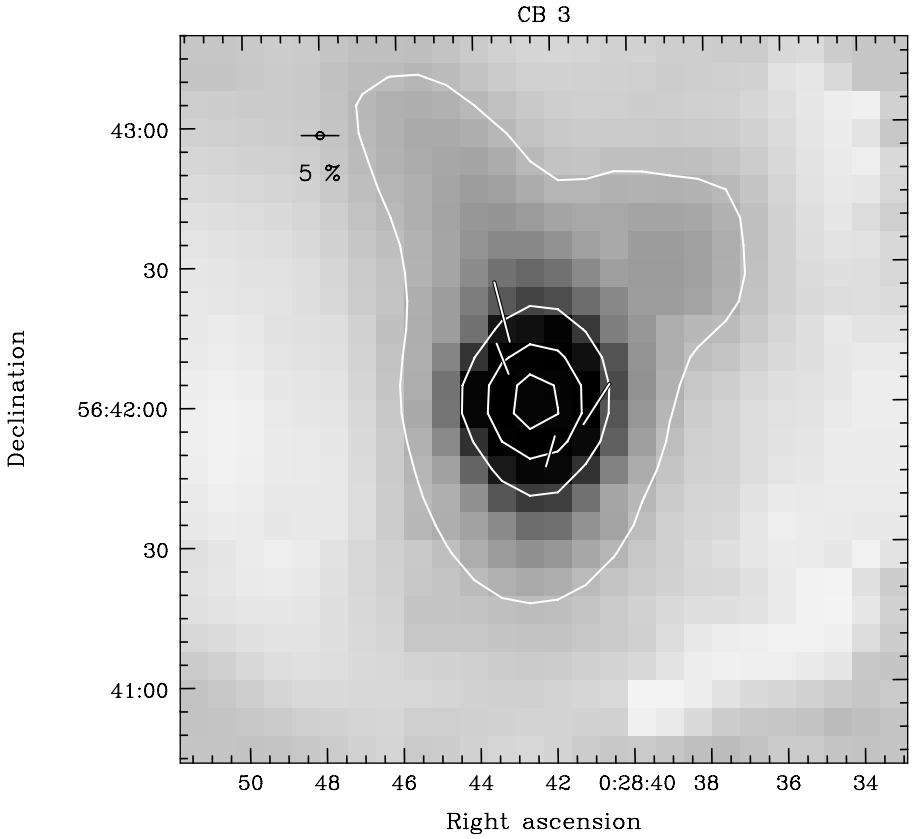

Figure 2. Compiled data toward the source CB 3. Contours range from 0.03 Jy beam^{-1} in steps of 0.3 Jy beam^{-1}. 850 μm polarization vectors are sampled on a 10″ grid. Vectors are plotted where $I > 0$, $p/dp > 2$, and $dp < 4\%$.

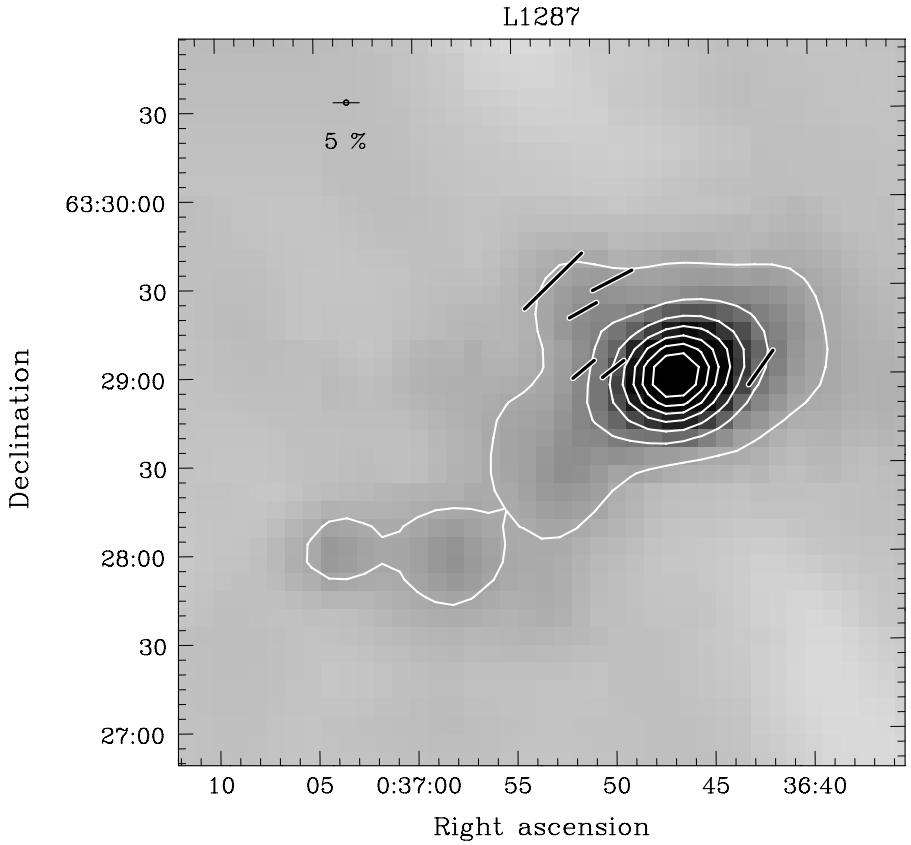

Figure 3. Compiled data toward the region L1287. Contours range from 0.2 Jy beam^{-1} in steps of 0.4 Jy beam^{-1}. 850 μm polarization vectors are sampled on a 10″ grid. Vectors are plotted where $I > 0$, $p/dp > 2$, and $dp < 4\%$.

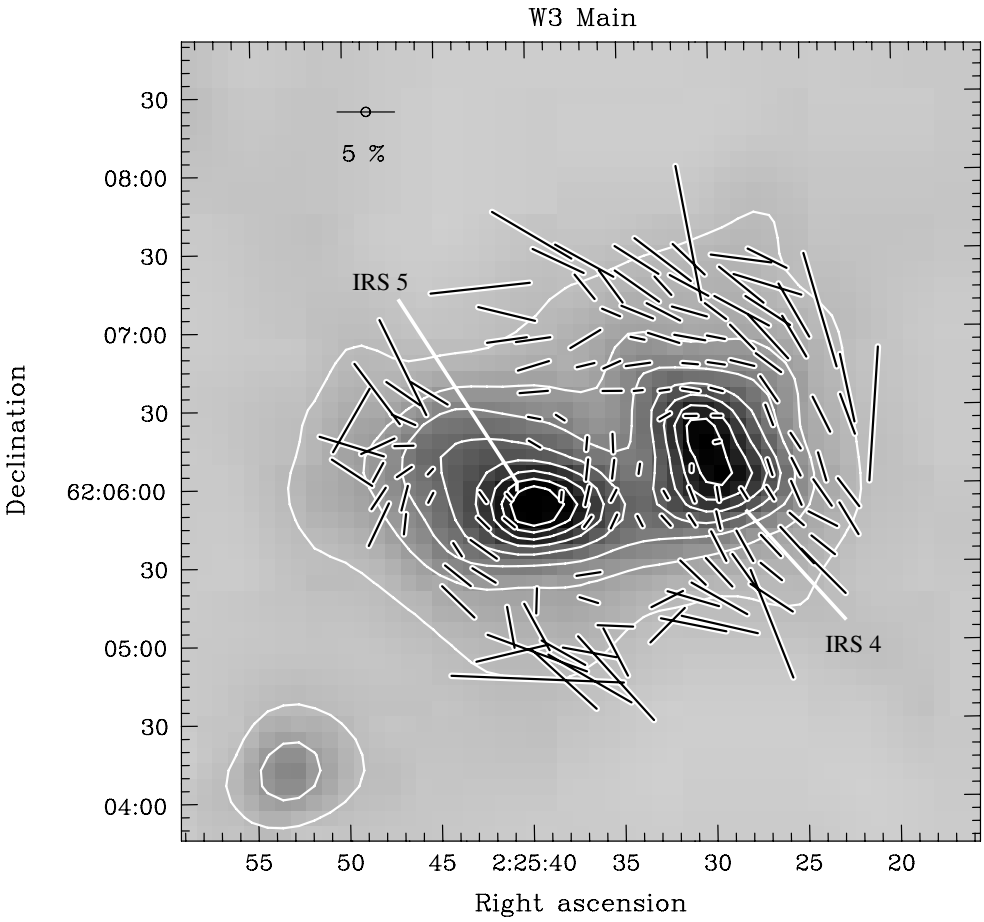

Figure 4. Compiled data toward the W3 (Main) molecular cloud. The two peaks are IRS 4 (right) and IRS 5 (left). Contours range from 0.5 Jy beam^{-1} in steps of 1 Jy beam^{-1}. 850 μm polarization vectors are sampled on a 10″ grid. Vectors are plotted where $I > 0$, $p/dp > 2$, and $dp < 4\%$.

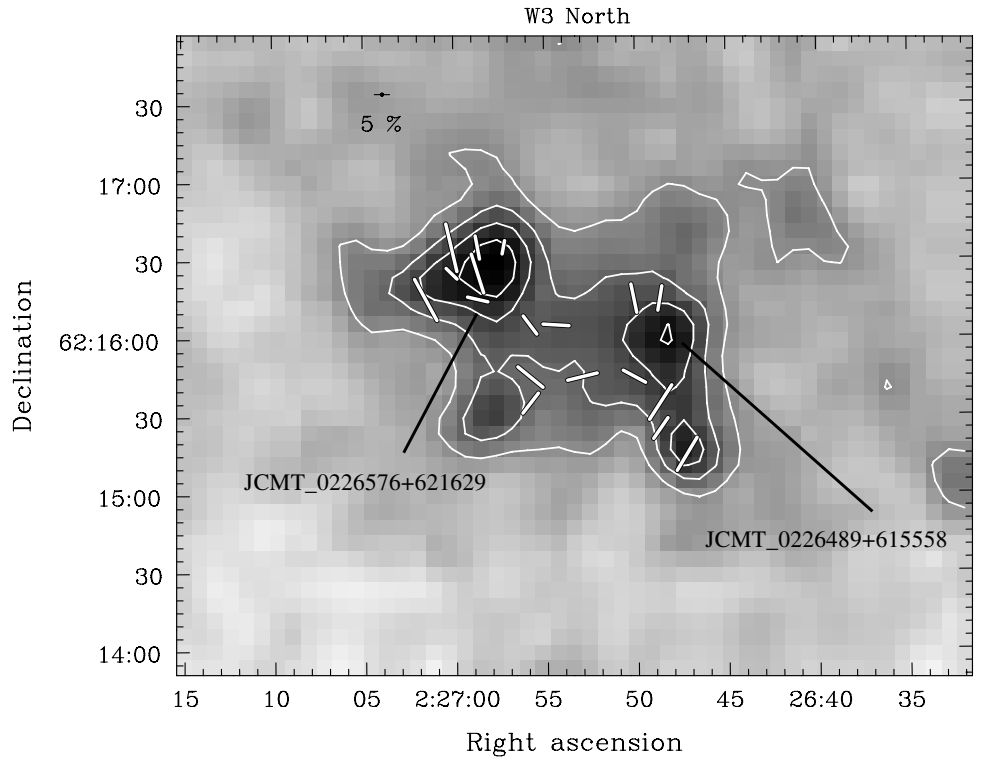

Figure 5. Compiled data toward the W3N molecular cloud. Contours range from 0.05 Jy beam^{-1} in steps of 0.05 Jy beam^{-1}. 850 μm polarization vectors are sampled on a 10″ grid. Vectors are plotted where $I > 0$, $p/dp > 2$, and $dp < 4\%$.

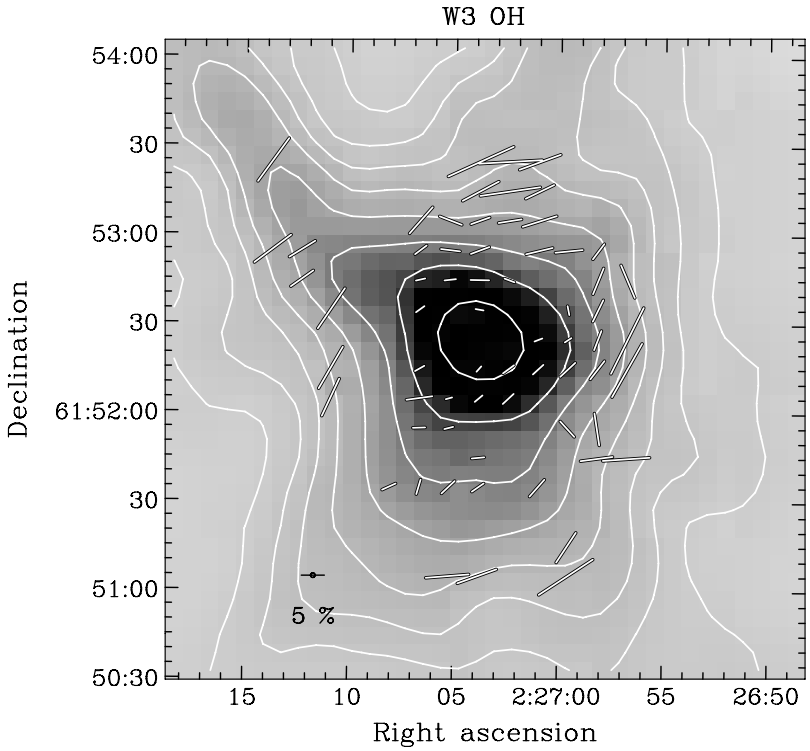

Figure 6. Compiled data toward the W3 OH molecular cloud. Contours are plotted at levels of 0.11, 0.20, 0.29, 0.42, 0.69, 1.2, 2.1 and 6.3 Jy beam^{-1}. 850 μm polarization vectors are sampled on a 10″ grid. Vectors are plotted where $I > 0$, $p/dp > 2$, and $dp < 4\%$.

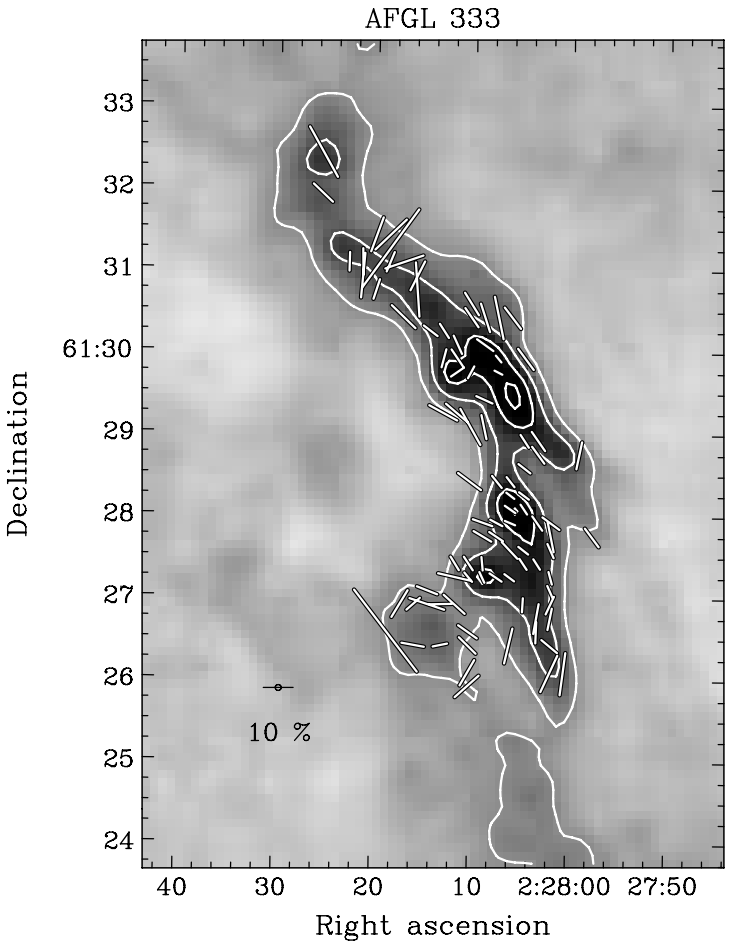

Figure 7. Compiled data toward source AFGL 333 within the W3 molecular cloud. Contours range from 0.1 Jy beam^{-1} in steps of 0.2 Jy beam^{-1}. 850 μm polarization vectors are sampled on a 10″ grid. Vectors are plotted where $I > 0$, $p/dp > 3$, and $dp < 3\%$.

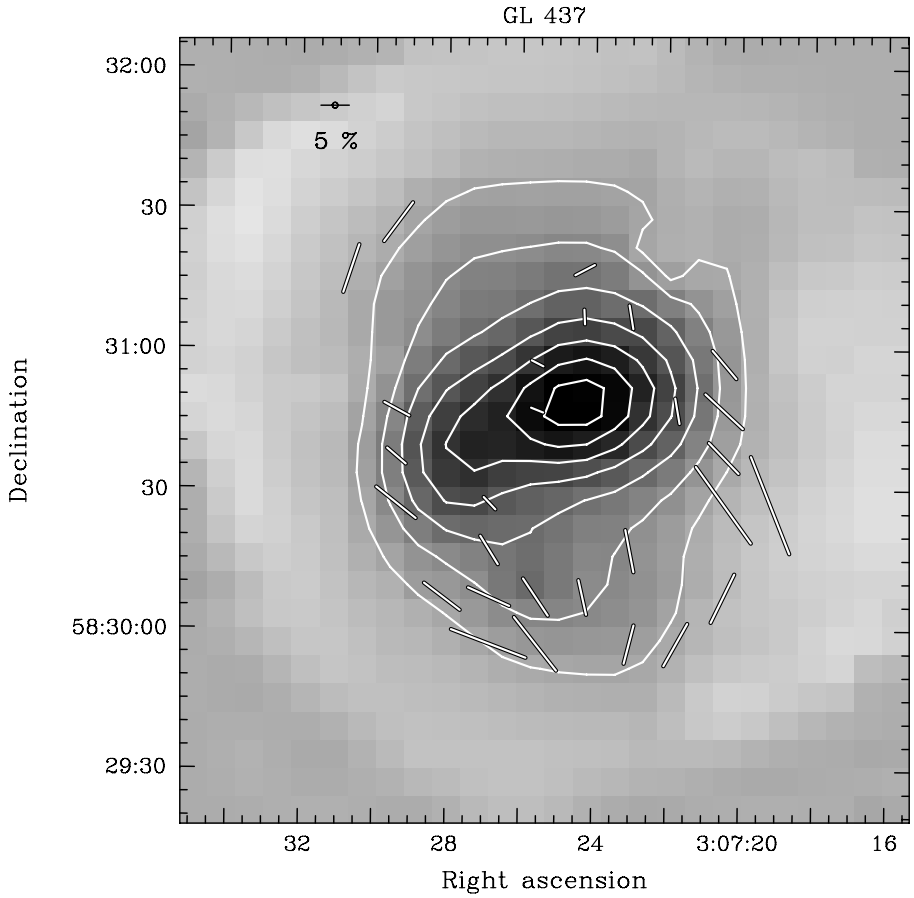

Figure 8. Compiled data toward the molecular cloud GL 437. Contours range from 0.05 Jy beam^{-1} in steps of 0.2 Jy beam^{-1}. 850 μm polarization vectors are sampled on a 10″ grid. Vectors are plotted where $I > 0$, $p/dp > 2$, and $dp < 4\%$.

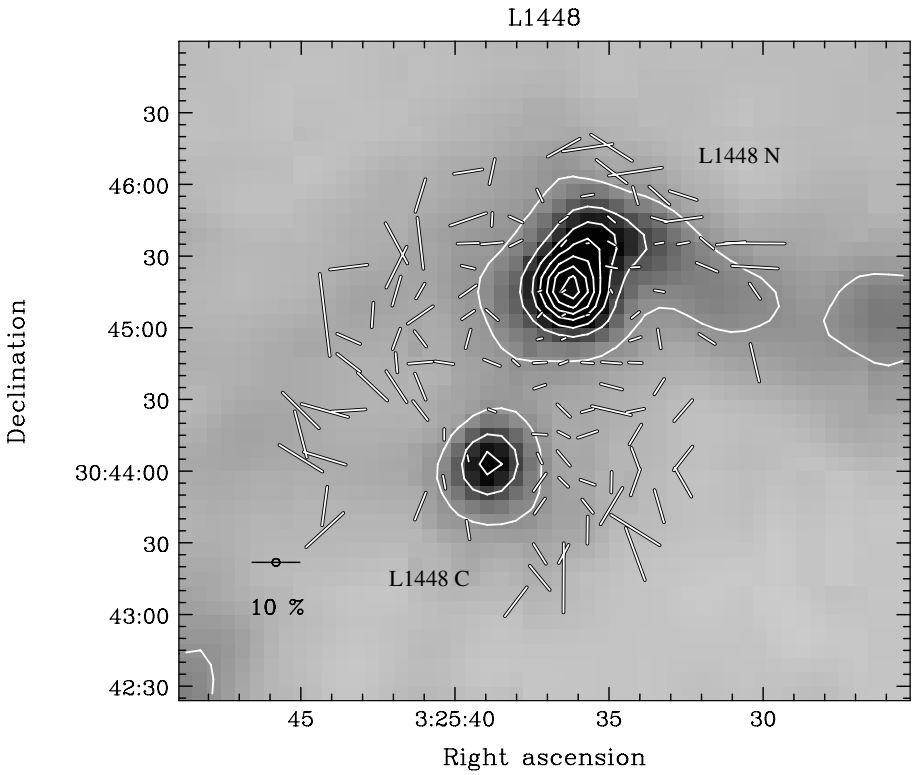

Figure 9. Compiled data toward the molecular cloud L1448. Contours range from 0.2 Jy beam^{-1} in steps of 0.4 Jy beam^{-1}. 850 μm polarization vectors are sampled on a 10″ grid. Vectors are plotted where $I > 0$, $p/dp > 2$, and $dp < 4\%$.

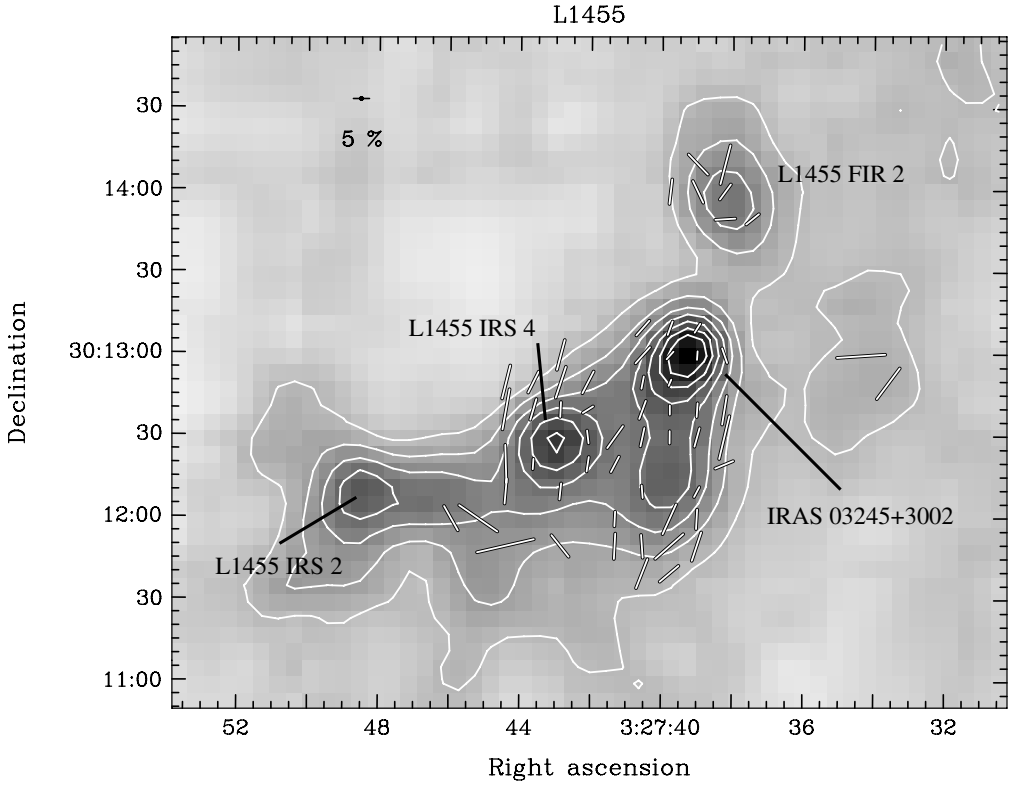

Figure 10. Compiled data toward the molecular cloud L1455. Contours range from 0.05 Jy beam^{-1} in steps of 0.05 Jy beam^{-1}. 850 μm polarization vectors are sampled on a 10″ grid. Vectors are plotted where $I > 0$, $p/dp > 2$, and $dp < 4\%$.

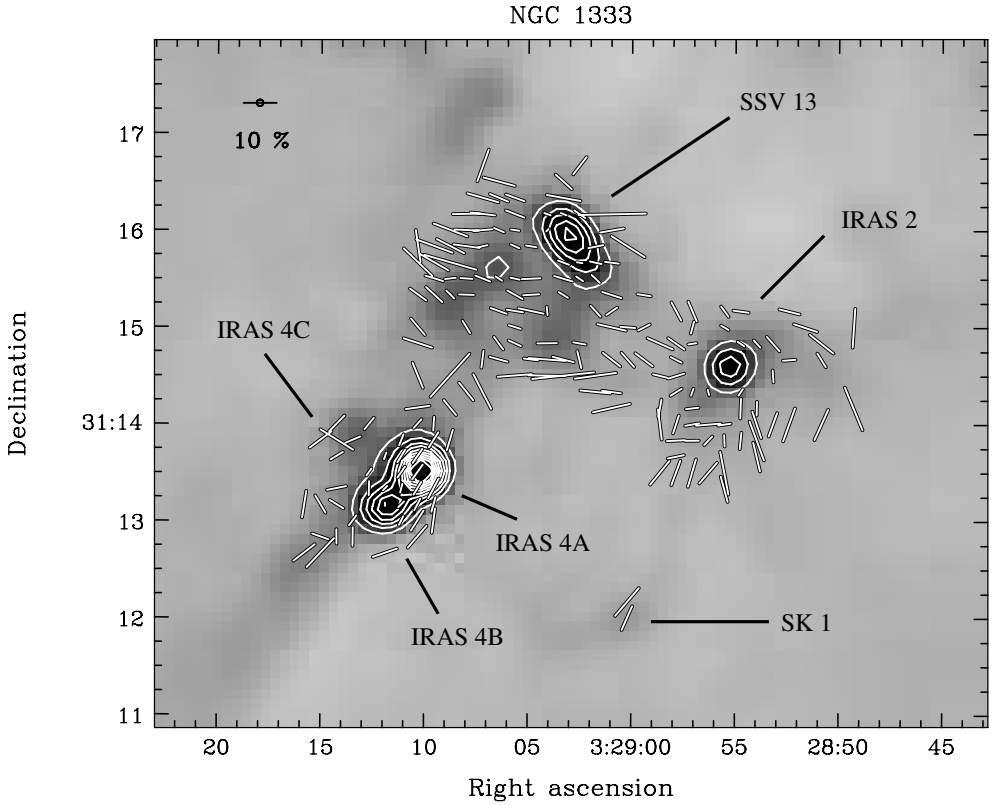

Figure 11. Compiled data toward the well-studied NGC 1333 cluster in Perseus. Contours range from 0.6 Jy beam^{-1} in steps of 0.4 Jy beam^{-1}. 850 μm polarization vectors are sampled on a 10″ grid. Vectors are plotted where $I > 0$, $p/dp > 2$, and $dp < 4\%$.

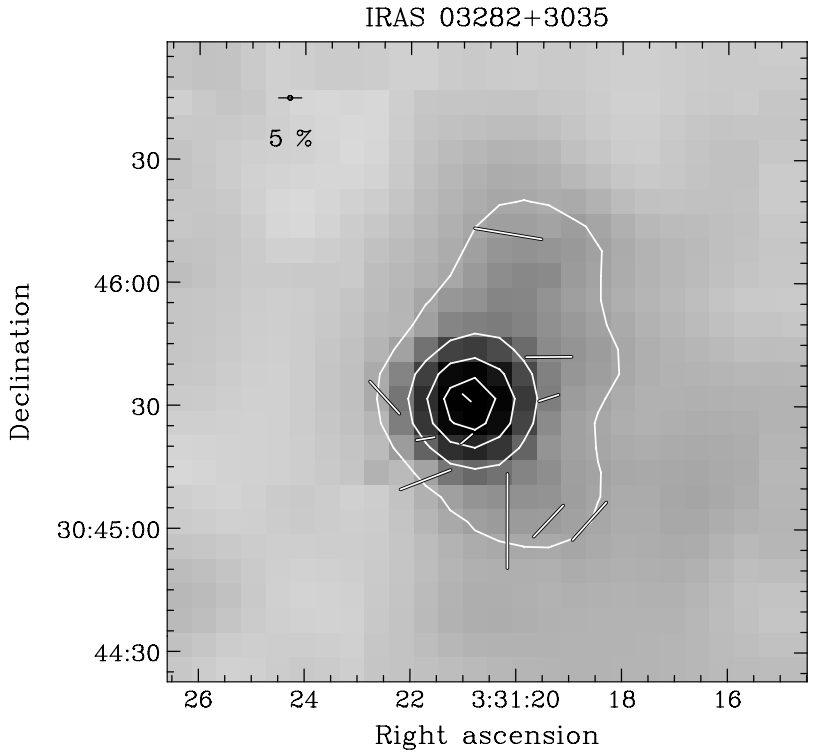

Figure 12. Compiled data toward the source IRAS 03282+3035. Contours range from 0.05 Jy beam^{-1} in steps of 0.15 Jy beam^{-1}. 850 μm polarization vectors are sampled on a 10″ grid. Vectors are plotted where $I > 0$, $p/dp > 2$, and $dp < 4\%$.

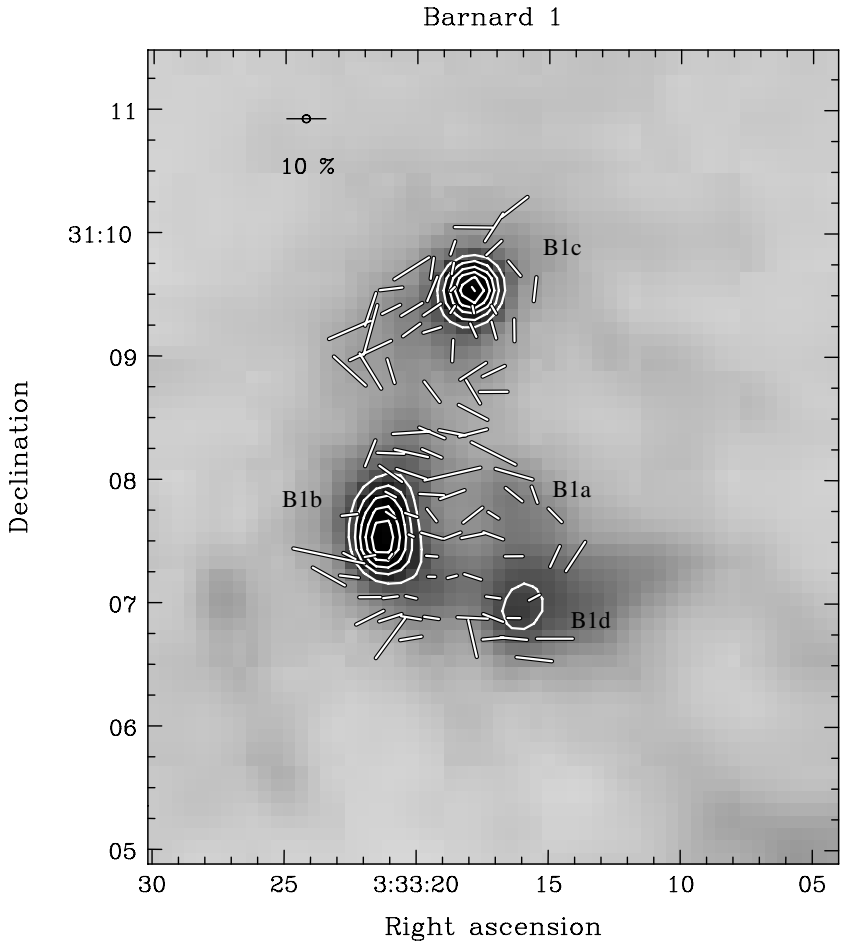

Figure 13. Compiled data toward the Barnard 1 region in the Perseus molecular cloud. Contours range from 0.5 Jy beam^{-1} in steps of 0.15 Jy beam^{-1}. 850 μm polarization vectors are sampled on a 10″ grid. Vectors are plotted where $I > 0$, $p/dp > 2$, and $dp < 4\%$.

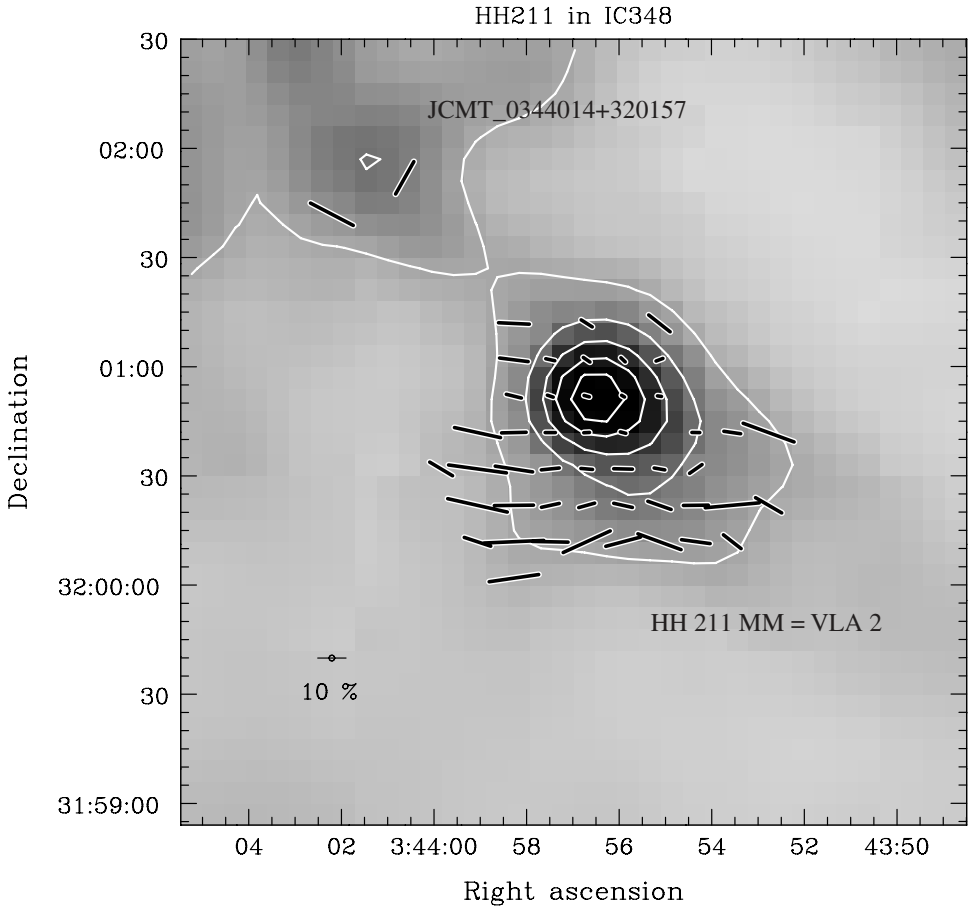

Figure 14. Compiled data toward the HH211 object in IC348, a region within the Perseus molecular cloud. Contours range from 0.1 Jy beam^{-1} in steps of 0.2 Jy beam^{-1}. 850 μm polarization vectors are sampled on a 10″ grid. Vectors are plotted where $I > 0$, $p/dp > 2$, and $dp < 4\%$.

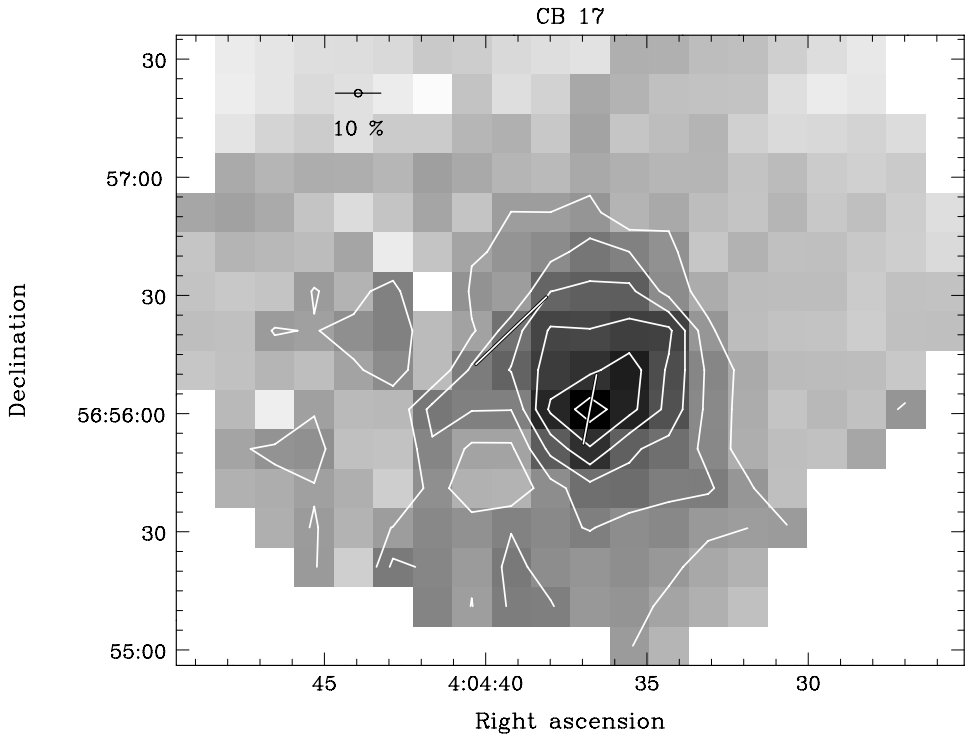

Figure 15. Compiled data toward the source CB 17. The intensity data are taken from SCUPOL data, rather than the SCUBA Legacy Catalog. Contours range from 0.22 Jy beam^{-1} in steps of 0.11 Jy beam^{-1}, where we have used a flux conversion factor of 557 Jy beam^{-1} V^{-1}. 850 μm polarization vectors are sampled on a 10″ grid. Vectors are plotted where $I > 0$, $p/dp > 2$, and $dp < 4\%$.

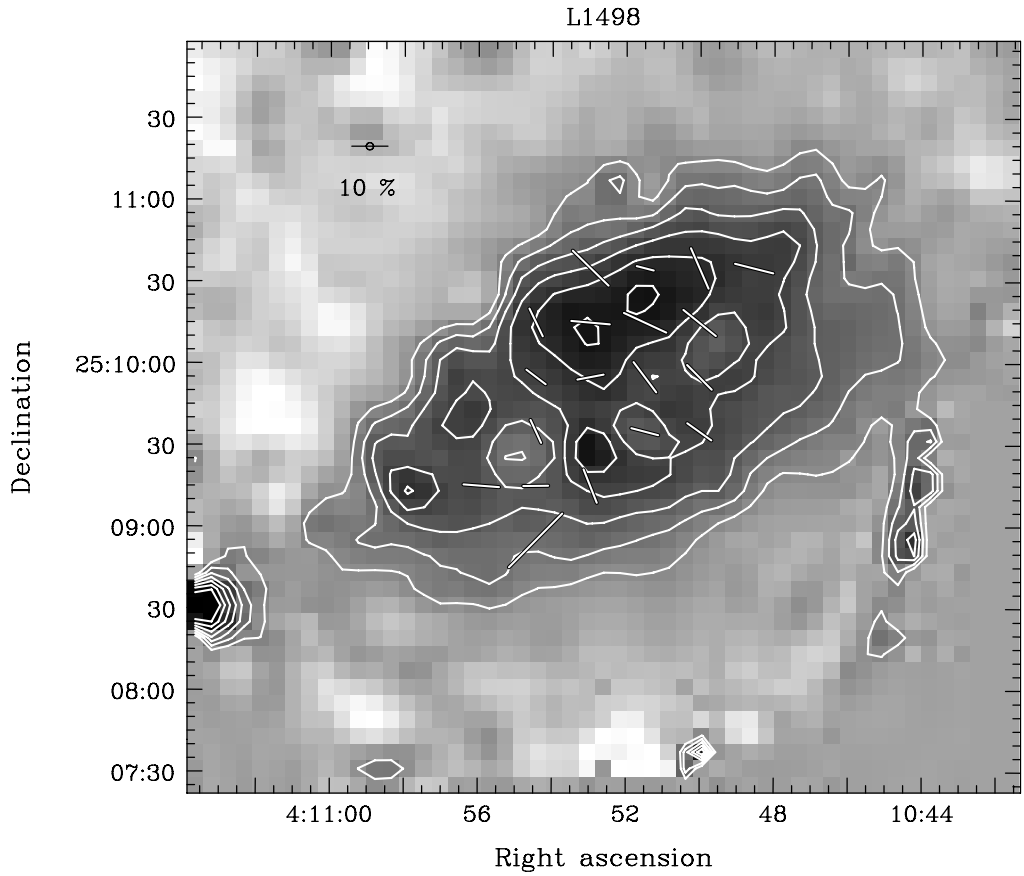

Figure 16. Compiled data toward the L1498 region in Taurus. Contours range from 0.01 Jy beam^{-1} in steps of 0.01 Jy beam^{-1}. 850 μm polarization vectors are sampled on a 20″ grid (binned from a 10″ grid). Vectors are plotted where $I > 0$, $p/dp > 2$, and $dp < 4\%$.

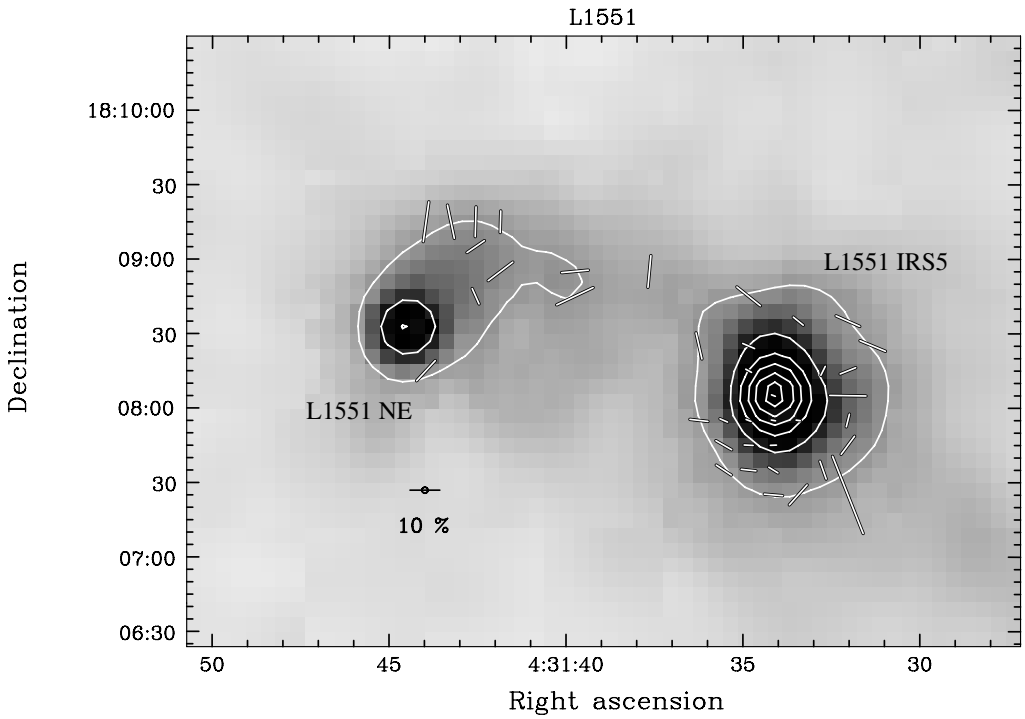

Figure 17. Compiled data toward the L1551 region in Taurus. Contours range from 0.2 Jy beam^{-1} in steps of 0.4 Jy beam^{-1}. 850 μm polarization vectors are sampled on a 10″ grid. Vectors are plotted where $I > 0$, $p/dp > 2$, and $dp < 4\%$.

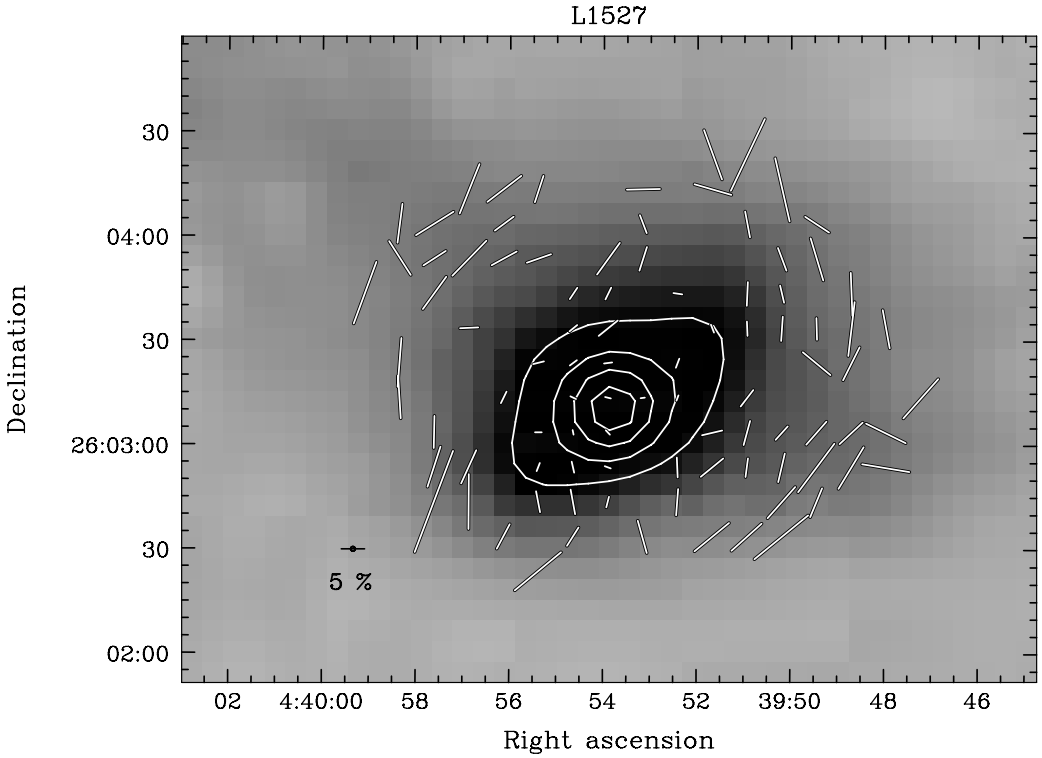

Figure 18. Compiled data toward the L1527 region in Taurus. Contours range from 0.3 Jy beam^{-1} in steps of 0.15 Jy beam^{-1}. 850 μm polarization vectors are sampled on a 10″ grid. Vectors are plotted where $I > 0$, $p/dp > 2$, and $dp < 4\%$.

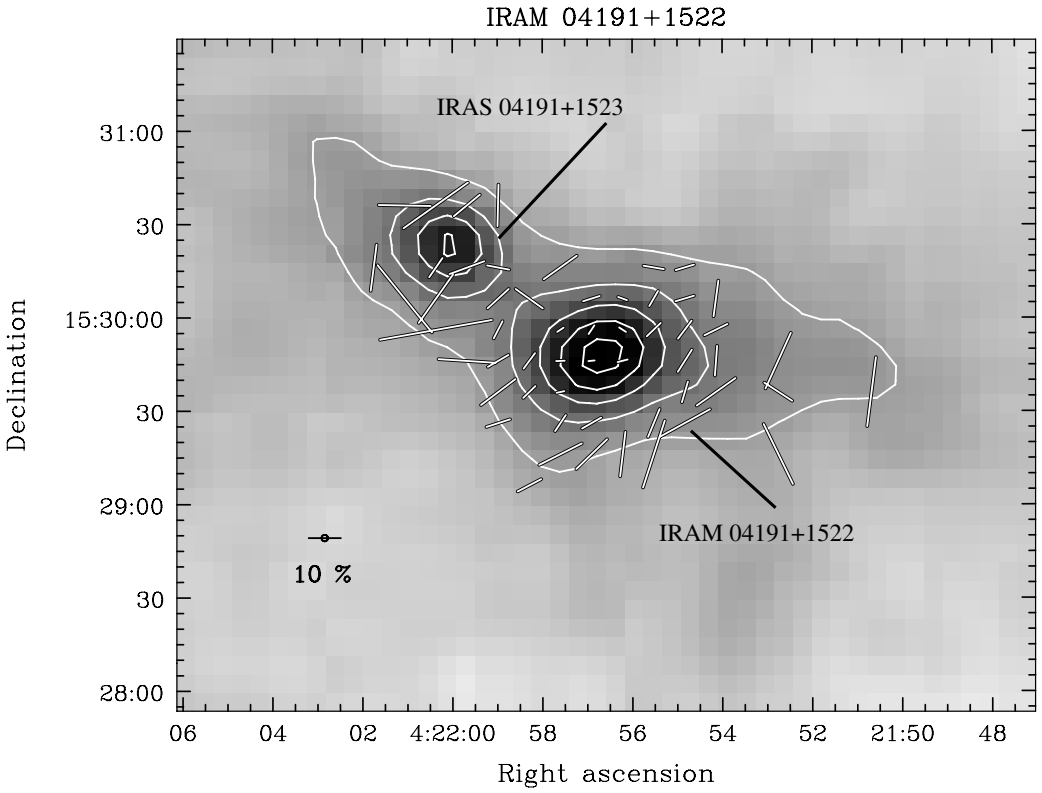

Figure 19. Compiled data toward the VeLLO IRAM 04191+1522. Contours range from 0.05 Jy beam^{-1} in steps of 0.05 Jy beam^{-1}. 850 μm polarization vectors are sampled on a 10″ grid. Vectors are plotted where $I > 0$, $p/dp > 2$, and $dp < 4\%$.

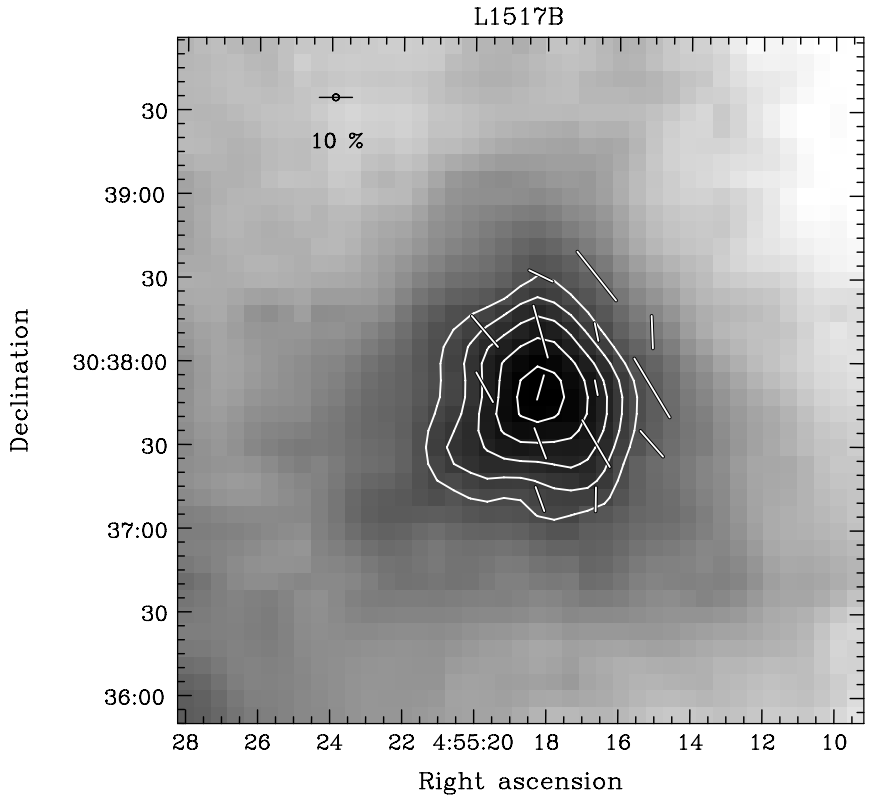

Figure 20. Compiled data toward the L1517B region in Taurus. Contours range from 0.01 Jy beam^{-1} in steps of 0.01 Jy beam^{-1}. 850 μm polarization vectors are sampled on a 20″ grid (binned from a 10″ grid). Vectors are plotted where $I > 0$, $p/dp > 2$, and $dp < 4\%$.

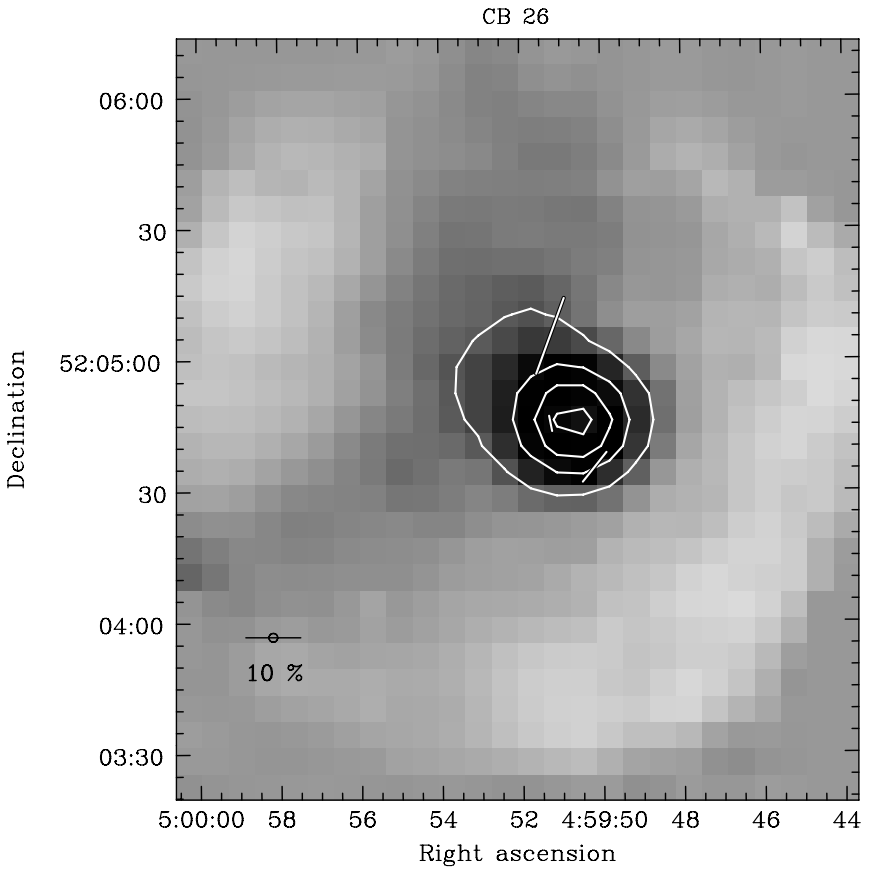

Figure 21. Compiled data toward the source CB 26. Contours range from 0.04 Jy beam^{-1} in steps of 0.06 Jy beam^{-1}. 850 μm polarization vectors are sampled on a 10″ grid. Vectors are plotted where $I > 0$, $p/dp > 2$, and $dp < 4\%$.

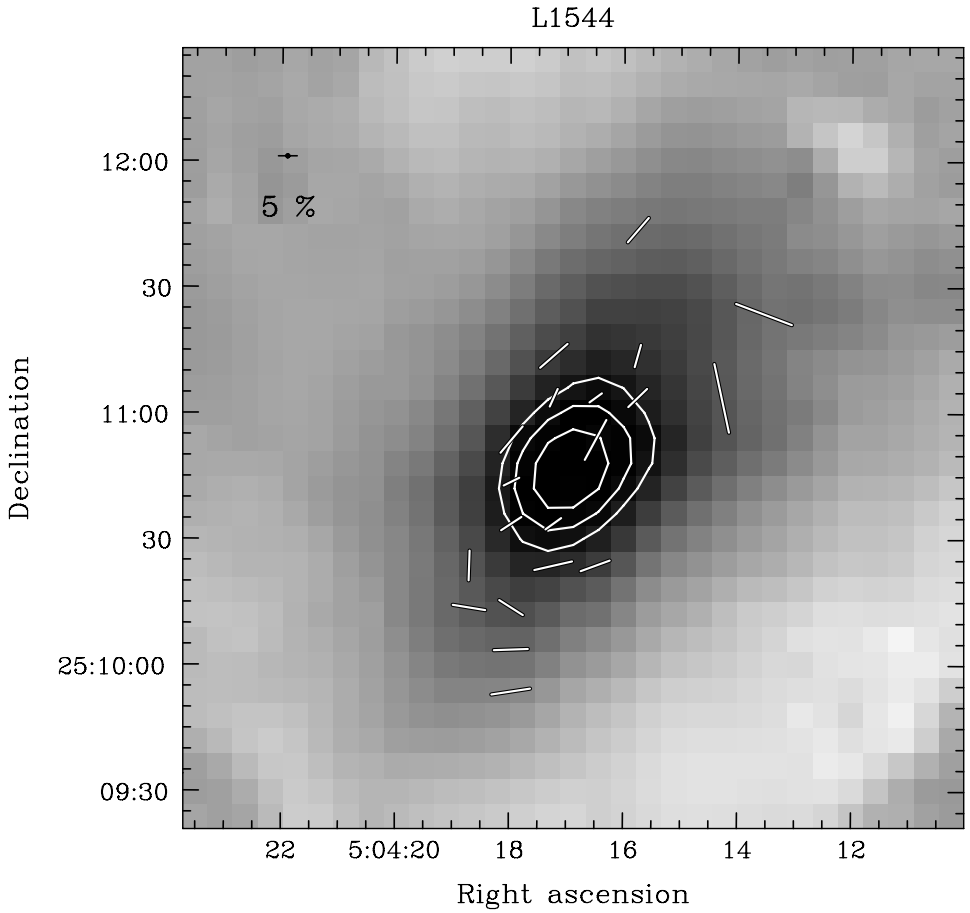

Figure 22. Compiled data toward the source L1544. Contours range from 0.15 Jy beam^{-1} in steps of 0.025 Jy beam^{-1}. 850 μm polarization vectors are sampled on a 10″ grid. Vectors are plotted where $I > 0$, $p/dp > 2$, and $dp < 4\%$.

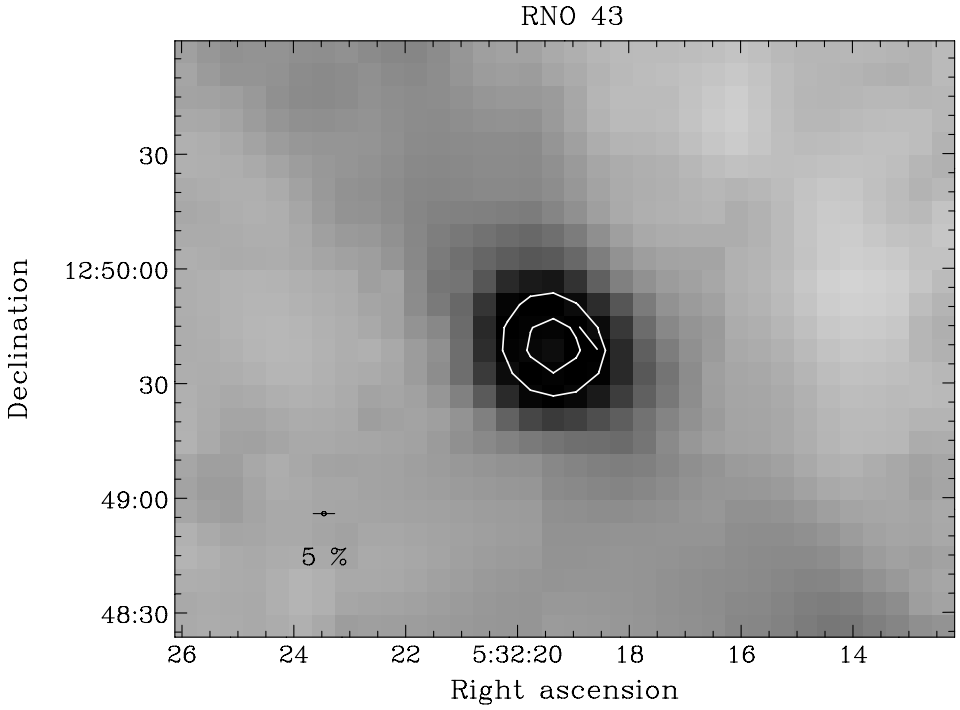

Figure 23. Compiled data toward the RNO 43 object in Monoceros. Contours range from 0.2 Jy beam^{-1} in steps of 0.15 Jy beam^{-1}. 850 μm polarization vectors are sampled on a 10″ grid. Vectors are plotted where $I > 0$, $p/dp > 2$, and $dp < 4\%$.

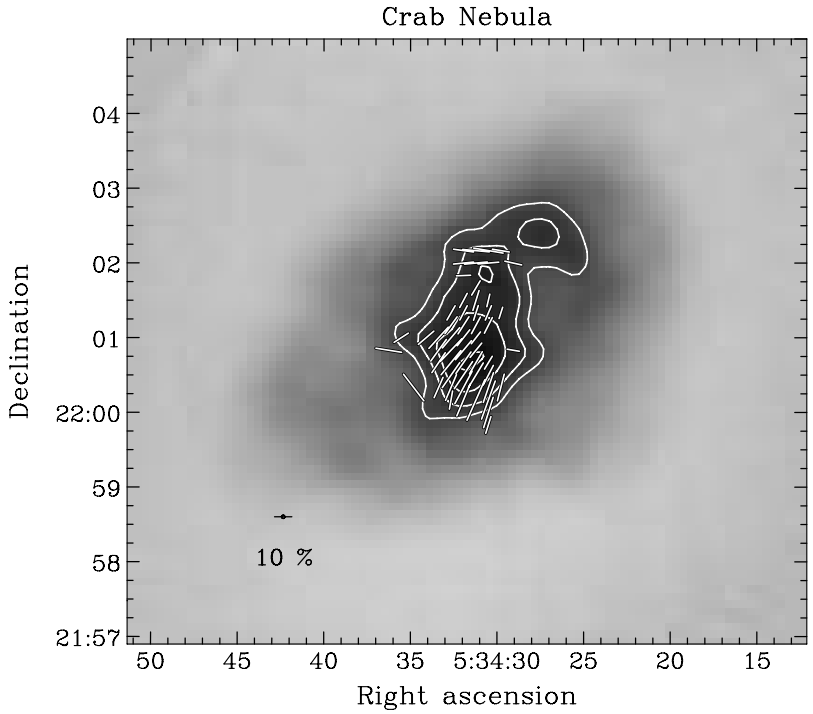

Figure 24. Compiled data toward the Crab Nebula. Contours start at 0.6 Jy beam^{-1} in steps of 0.1 Jy beam^{-1}. 850 μm polarization vectors are sampled on a 10″ grid. Vectors are plotted where $I > 0$, $p/dp > 2$, and $dp < 4\%$.

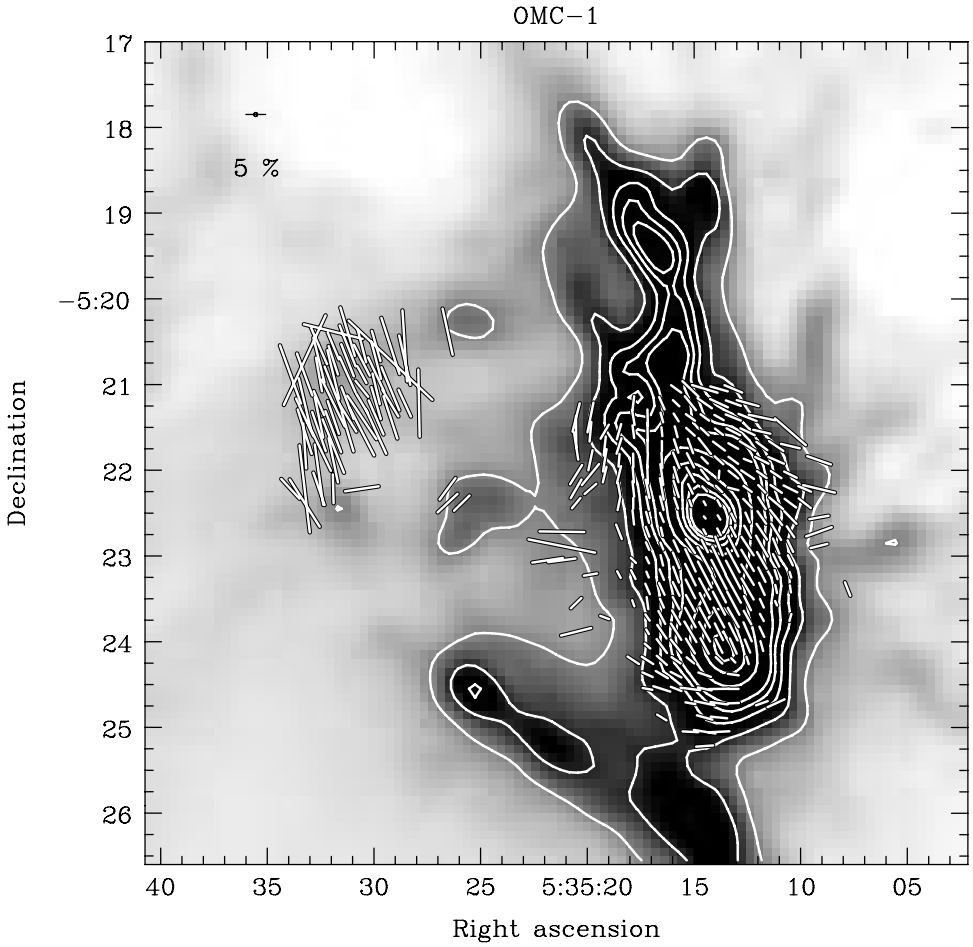

Figure 25. Compiled data toward the OMC-1 core within the Orion A "Integral-shaped Filament." Contours range from 1 Jy beam^{-1} in steps of 1 Jy beam^{-1}, and then from 10 Jy beam^{-1} in steps of 10 Jy beam^{-1}. 850 μm polarization vectors are sampled on a 10″ grid. Vectors are plotted where $I > 0$, $p/dp > 2$, and $dp < 4\%$.

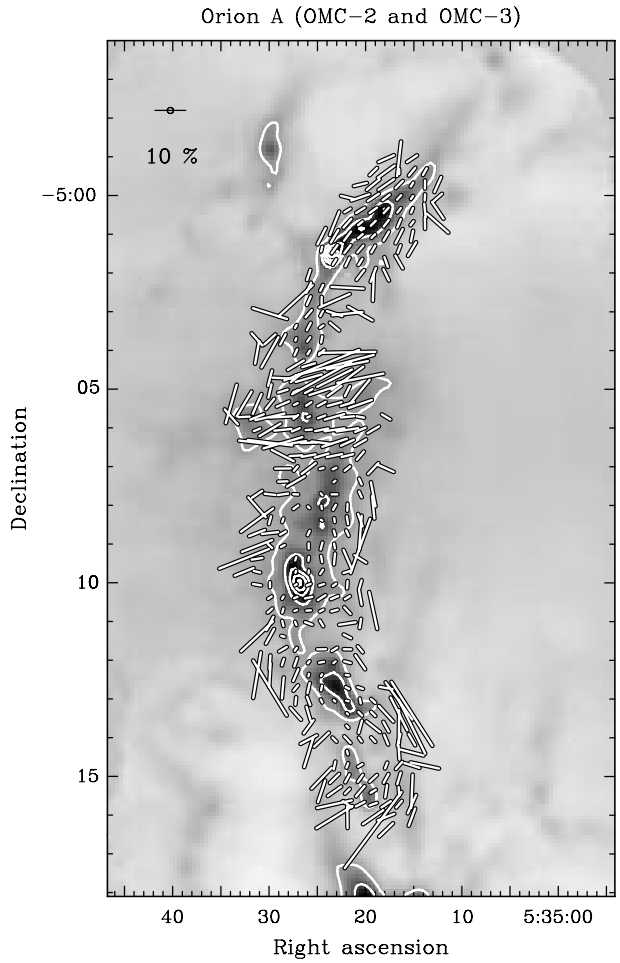

Figure 26. Compiled data toward the OMC-2 and OMC-3 regions of the Orion A "Integral-shaped Filament." Contours range from 0.4 Jy beam^{-1} in steps of 0.8 Jy beam^{-1}. 850 μm polarization vectors are sampled on a 20″ grid (binned from a 10″ grid to better see the vectors). Vectors are plotted where $I > 0$, $p/dp > 2$, and $dp < 4\%$.

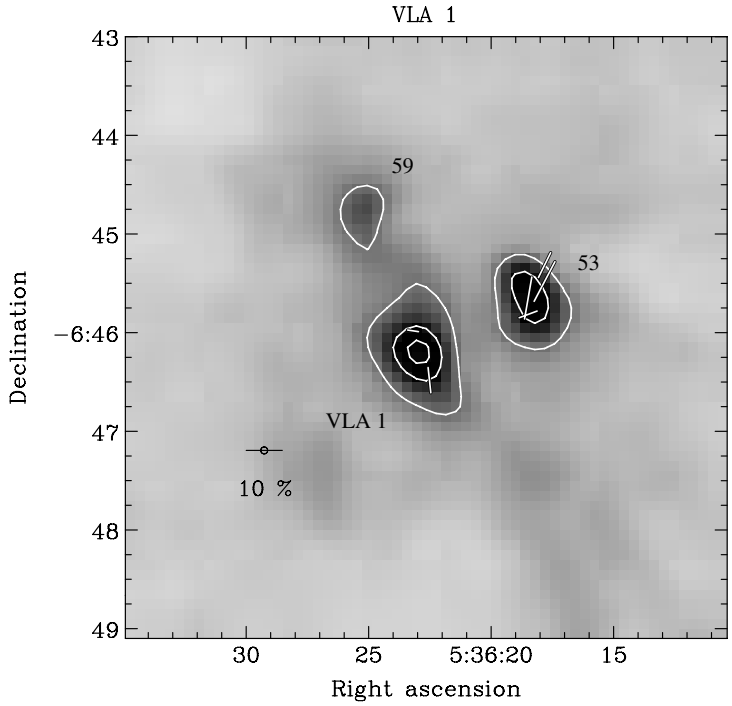

Figure 27. Compiled data toward the source VLA 1. Core designations are from Pravdo et al. (1985). Contours range from 0.3 Jy beam^{-1} in steps of 0.4 Jy beam^{-1}. 850 μm polarization vectors are sampled on a 10″ grid. Vectors are plotted where $I > 0$, $p/dp > 2$, and $dp < 4\%$.

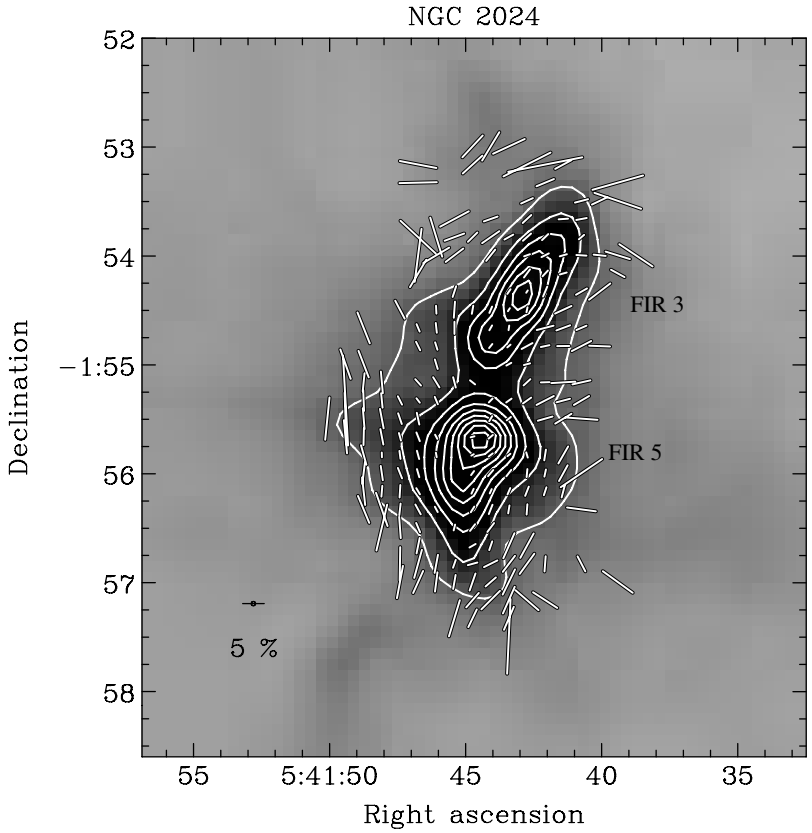

Figure 28. Compiled data toward the NGC 2024 ridge in the Orion B molecular cloud. Contours range from 1 Jy beam^{-1} in steps of 1 Jy beam^{-1}. 850 μm polarization vectors are sampled on a 10″ grid. Vectors are plotted where $I > 0$, $p/dp > 2$, and $dp < 4\%$.

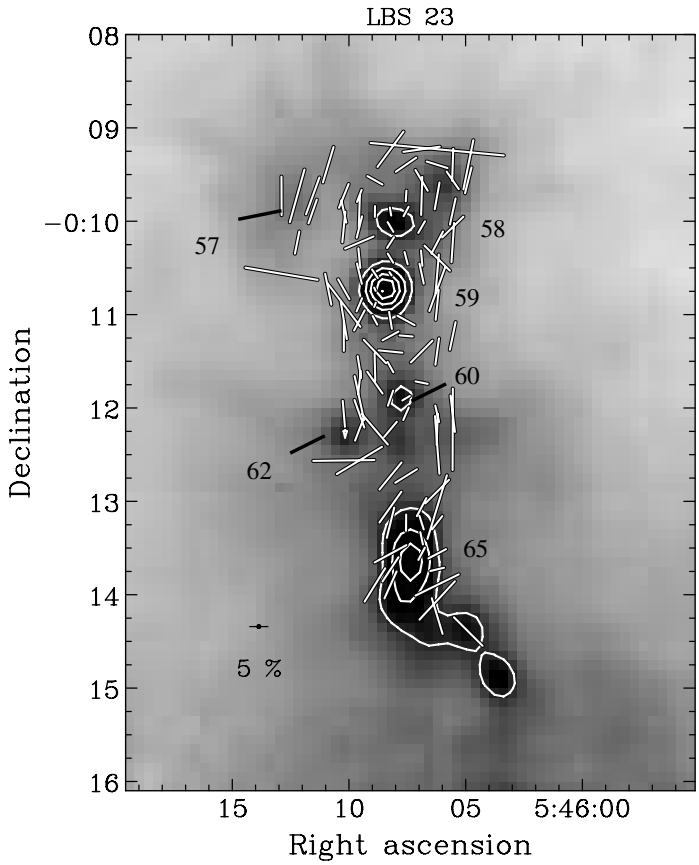

Figure 29. Compiled data toward the LBS 23 ridge in the Orion B molecular cloud. Core designations are from Mitchell et al. (2001). Contours range from 0.5 Jy beam^{-1} in steps of 0.25 Jy beam^{-1}. 850 μm polarization vectors are sampled on a 10″ grid. Vectors are plotted where $I > 0$, $p/dp > 2$, and $dp < 4\%$.

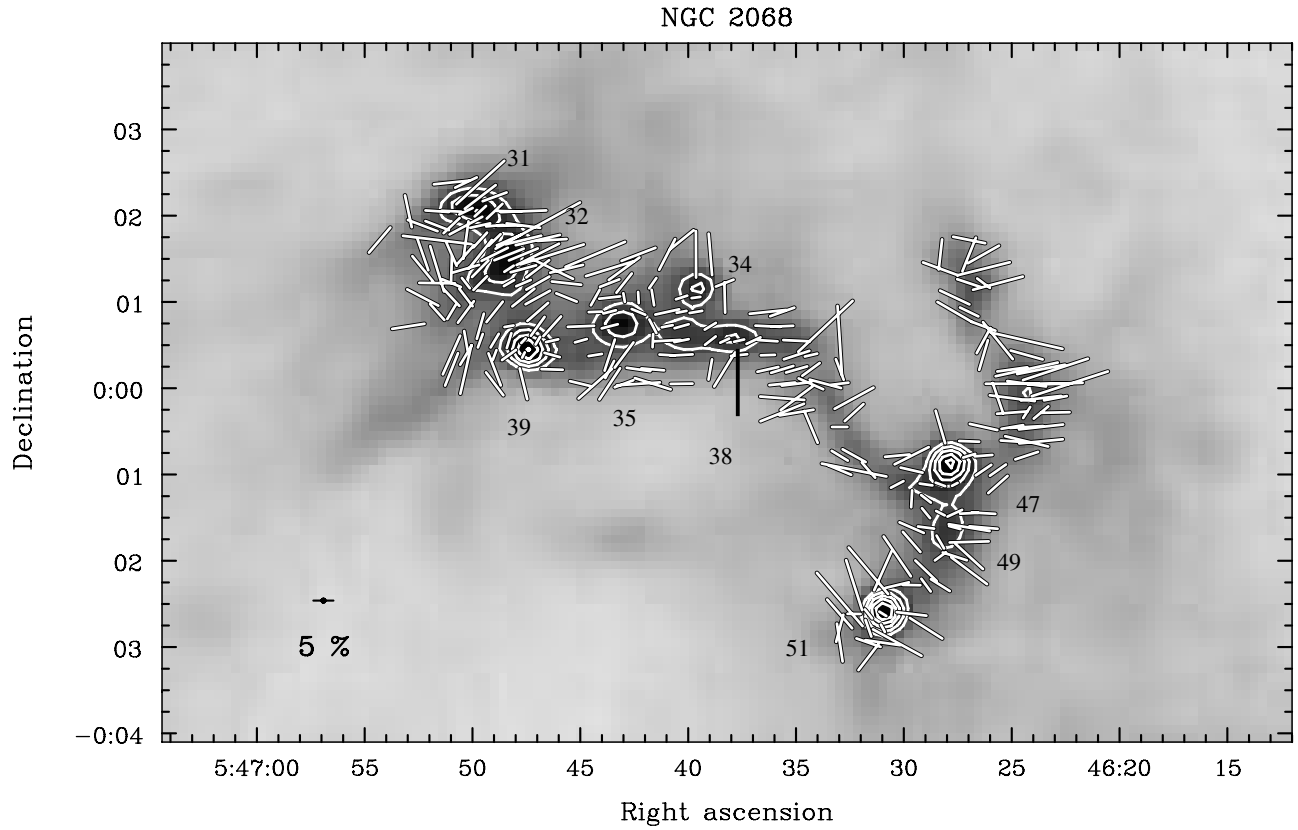

Figure 30. Compiled data toward the NGC 2068 filament in the Orion B molecular cloud. Core designations are from Mitchell et al. (2001). Contours range from 0.4 Jy beam^{-1} in steps of 1 Jy beam^{-1}. 850 μm polarization vectors are sampled on a 10″ grid. Vectors are plotted where $I > 0$, $p/dp > 2$, and $dp < 4\%$.

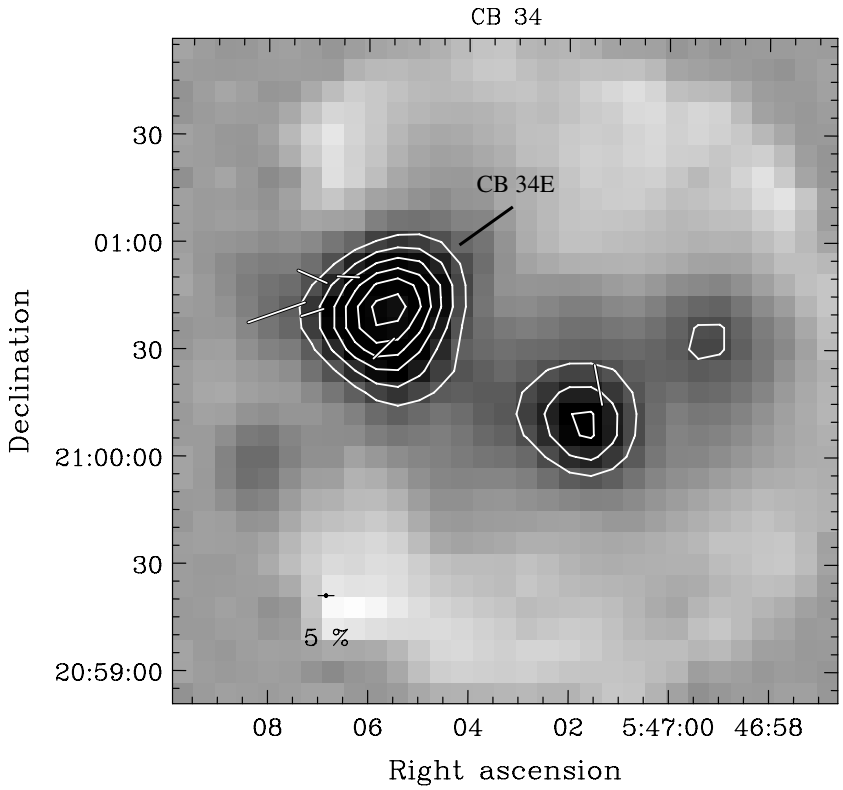

Figure 31. Compiled data toward the source CB 34. The eastern core designation is from Vallée et al. (2000). Contours range from 0.1 Jy beam^{-1} in steps of 0.05 Jy beam^{-1}. 850 μm polarization vectors are sampled on a 10″ grid. Vectors are plotted where $I > 0$, $p/dp > 2$, and $dp < 4\%$.

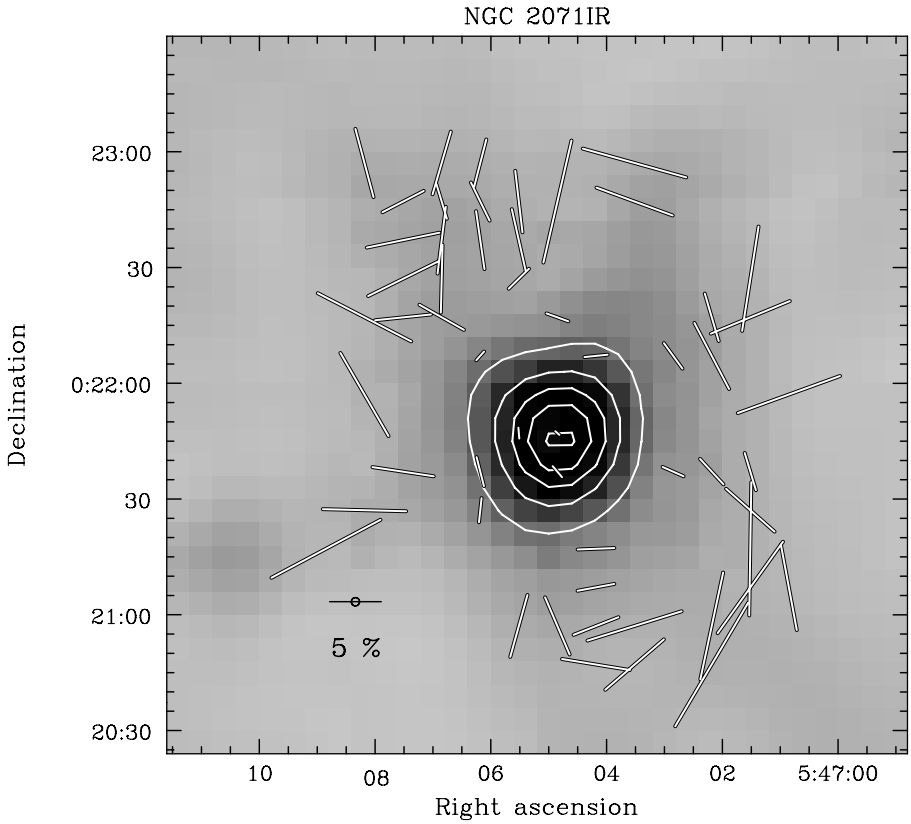

Figure 32. Compiled data toward the NGC 2071 IR massive core in the Orion B molecular cloud. Contours range from 1 Jy beam^{-1} in steps of 1 Jy beam^{-1}. 850 μm polarization vectors are sampled on a 10″ grid. Vectors are plotted where $I > 0$, $p/dp > 2$, and $dp < 4\%$.

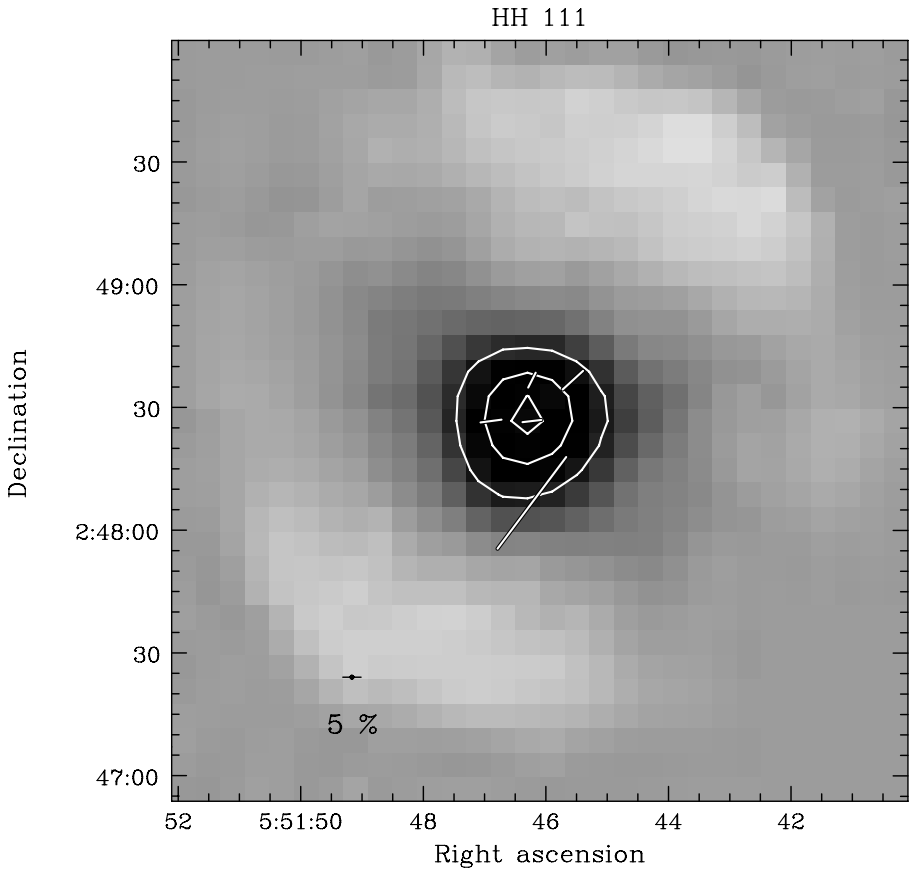

Figure 33. Compiled data toward the HH 111 object. Contours range from 0.25 Jy beam^{-1} in steps of 0.25 Jy beam^{-1}. 850 μm polarization vectors are sampled on a 10″ grid. Vectors are plotted where $I > 0$, $p/dp > 2$, and $dp < 4\%$.

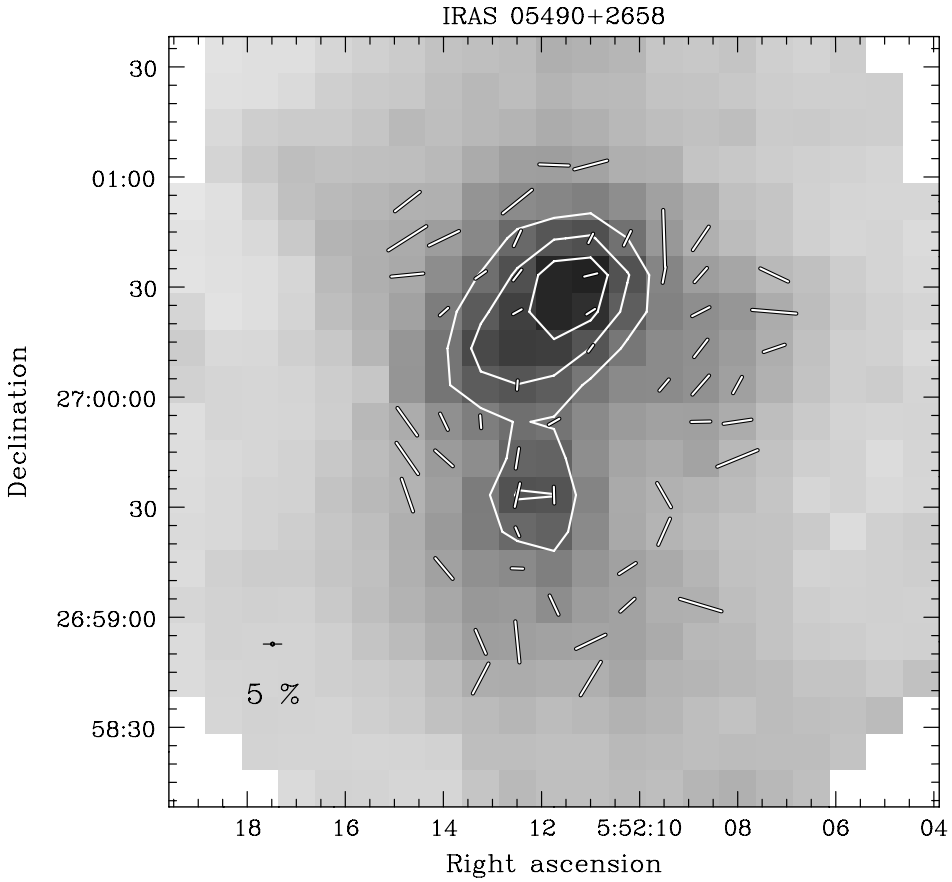

Figure 34. Compiled data toward IRAS 05490+2658. The intensity data are taken from SCUPOL data, rather than the SCUBA Legacy Catalog. Contours range from 1 Jy beam^{-1} in steps of 0.25 Jy beam^{-1} where we have used a conversion factor of 455 Jy beam^{-1} V^{-1}. 850 μm polarization vectors are sampled on a 10″ grid. Vectors are plotted where $I > 0$, $p/dp > 2$, and $dp < 4\%$.

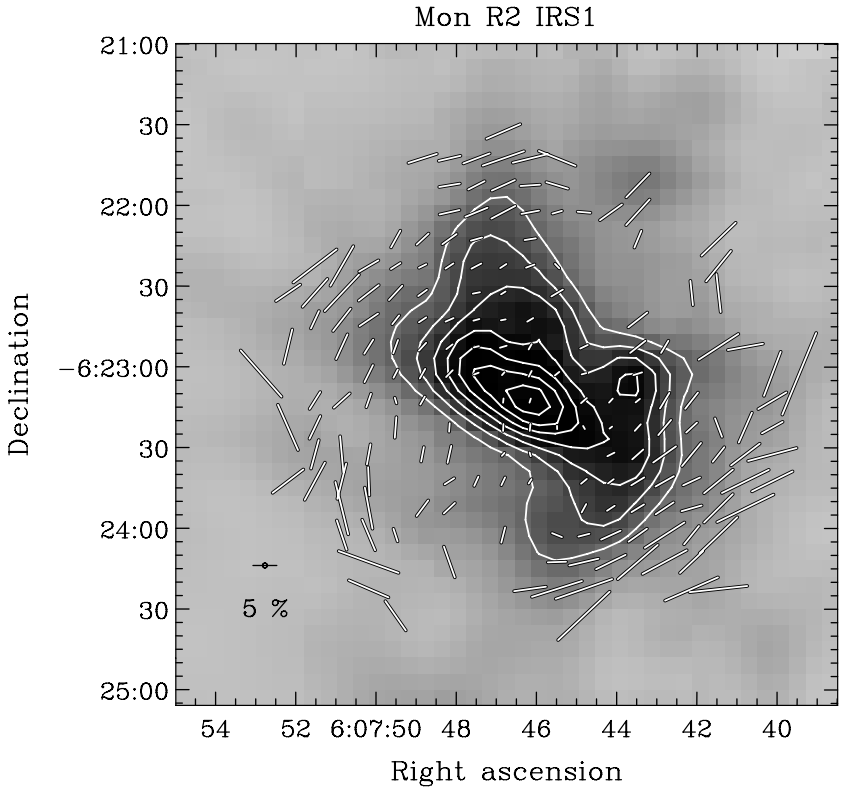

Figure 35. Compiled data toward Mon R2 IRS1. Contours range from 1.5 Jy beam^{-1} in steps of 0.5 Jy beam^{-1}. 850 μm polarization vectors are sampled on a 10″ grid. Vectors are plotted where $I > 0$, $p/dp > 2$, and $dp < 4\%$.

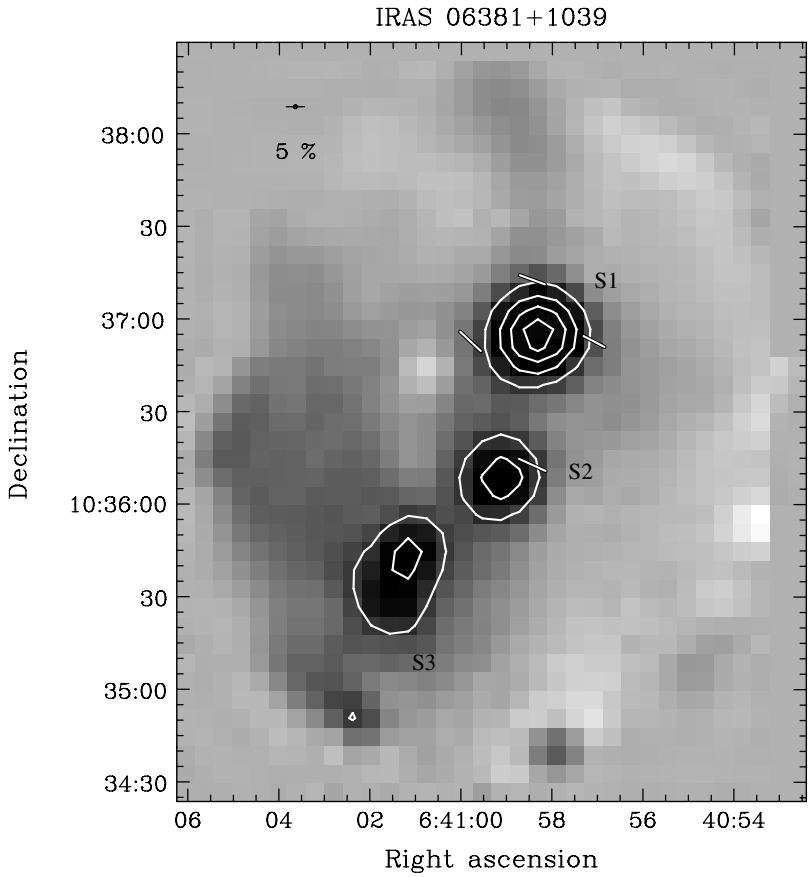

Figure 36. Compiled data toward Mon IRAS 27 (IRAS 06381+1039). Core designations are from Wolf-Chase et al. (2003). Contours range from 0.3 Jy beam^{-1} in steps of 0.2 Jy beam^{-1}. 850 μm polarization vectors are sampled on a 20″ grid (binned from a 10″ grid). Vectors are plotted where $I > 0$, $p/dp > 2$, and $dp < 4\%$.

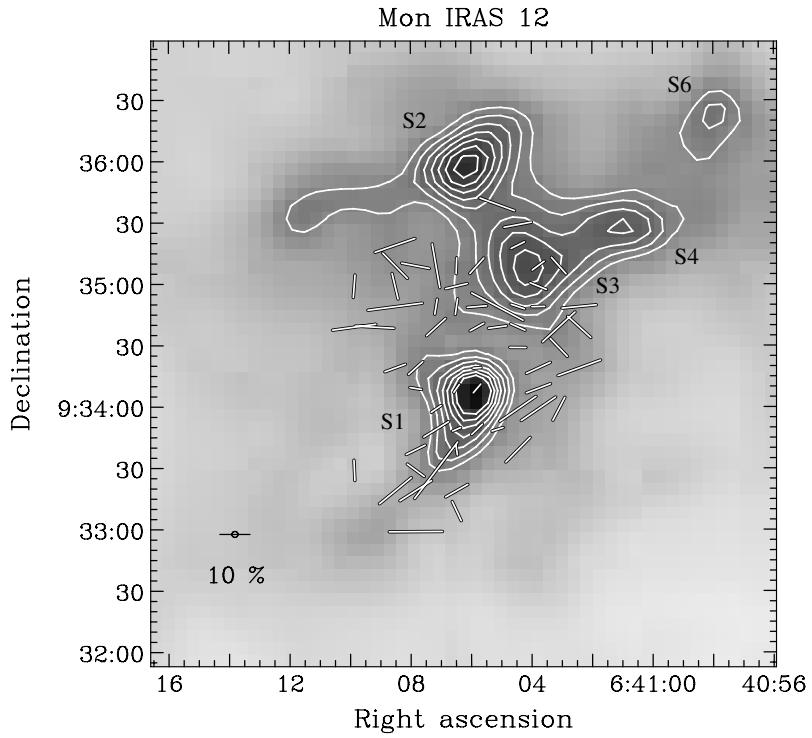

Figure 37. Compiled data toward Mon IRAS 12. Core designations are from Wolf-Chase et al. (2003). Contours range from 0.5 Jy beam^{-1} in steps of 0.1 Jy beam^{-1}. 850 μm polarization vectors are sampled on a 10″ grid. Vectors are plotted where $I > 0$, $p/dp > 4$, and $dp < 2\%$.

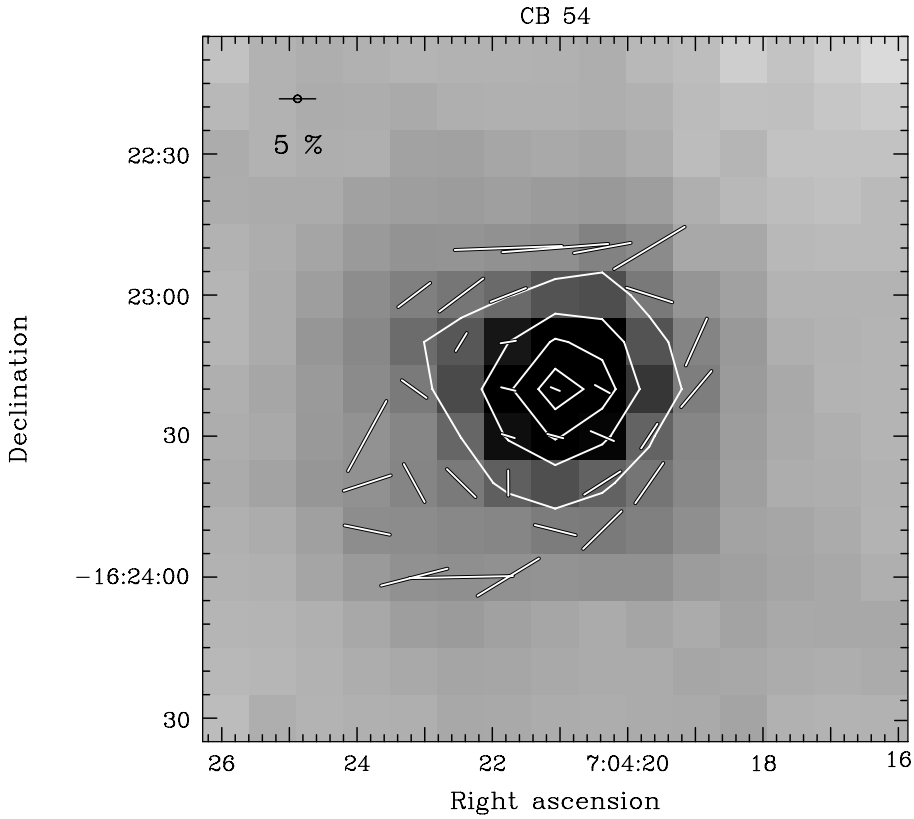

Figure 38. Compiled data toward the source CB 54. The intensity data are taken from SCUPOL data, rather than the SCUBA Legacy Catalog. Contours range from 0.45 Jy beam^{-1} in steps of 0.45 Jy beam^{-1} where we have applied a flux conversion factor of 455 Jy beam^{-1} Volt^{-1} for conversion to flux density. 850 μm polarization vectors are sampled on a 10″ grid. Vectors are plotted where $I > 0$, $p/dp > 2$, and $dp < 4\%$.

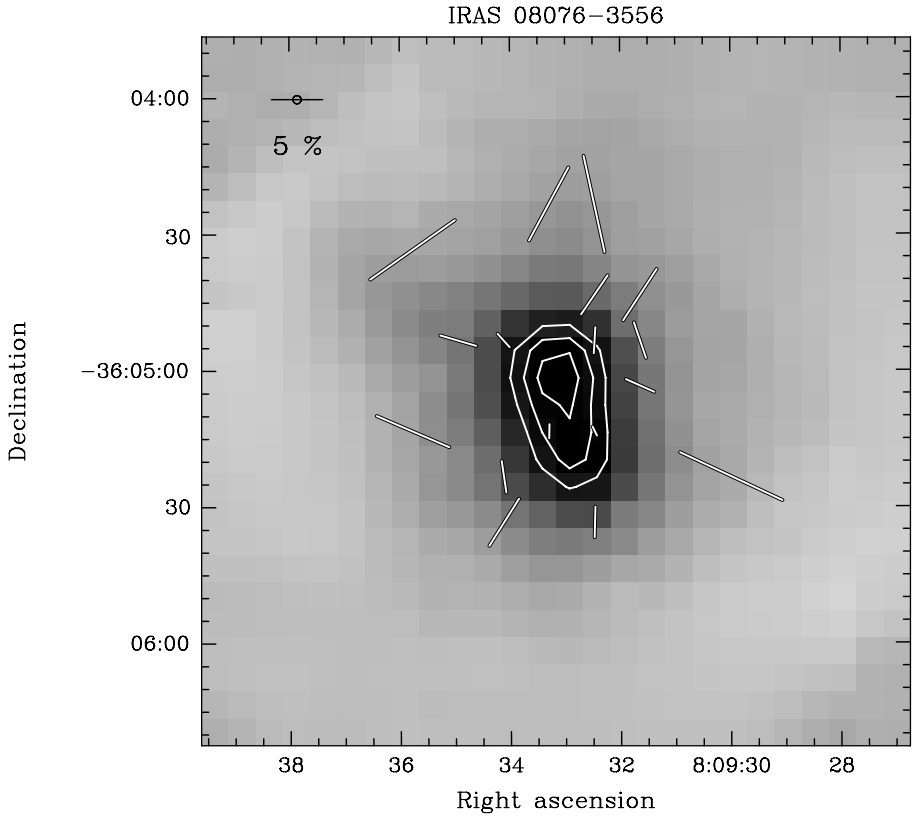

Figure 39. Compiled data toward the source IRAS 08076-3556. Contours range from 0.5 Jy beam^{-1} in steps of 0.1 Jy beam^{-1}. 850 μm polarization vectors are sampled on a 10″ grid. Vectors are plotted where $I > 0$, $p/dp > 2$, and $dp < 4\%$.

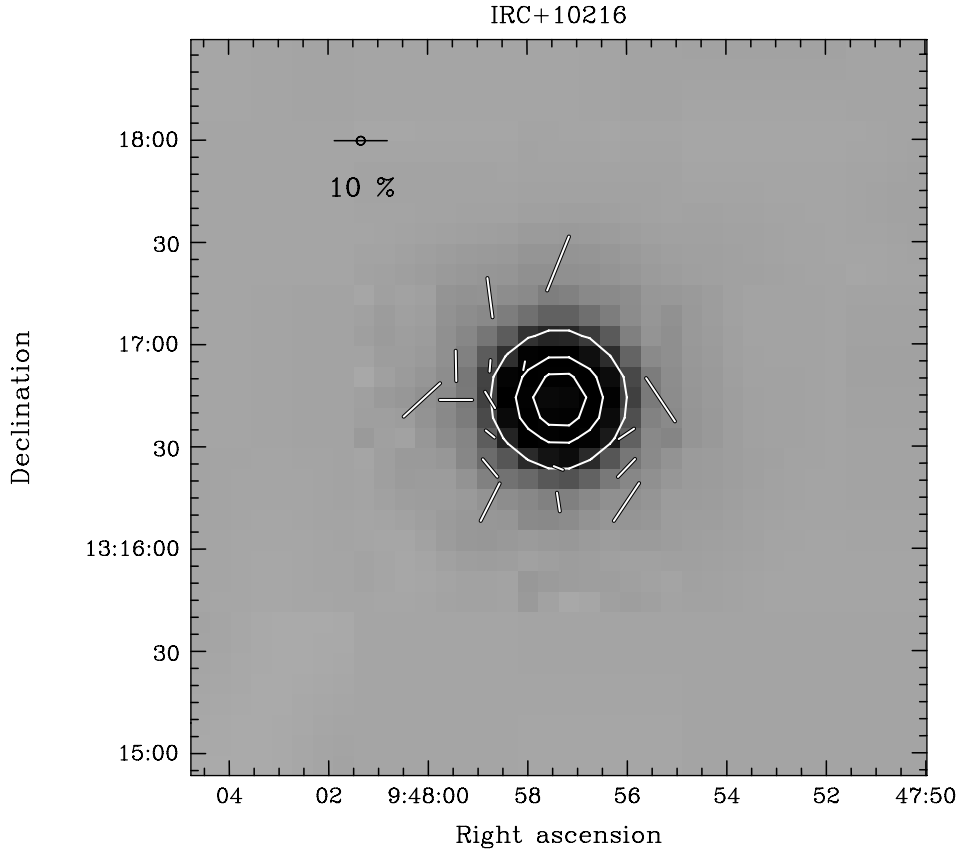

Figure 40. Compiled data toward the post-AGB star IRC +10216. Contours range from 0.6 Jy beam^{-1} in steps of 0.9 Jy beam^{-1}. 850 μm polarization vectors are sampled on a 10″ grid. Vectors are plotted where $I > 0$, $p/dp > 2$, and $dp < 4\%$.

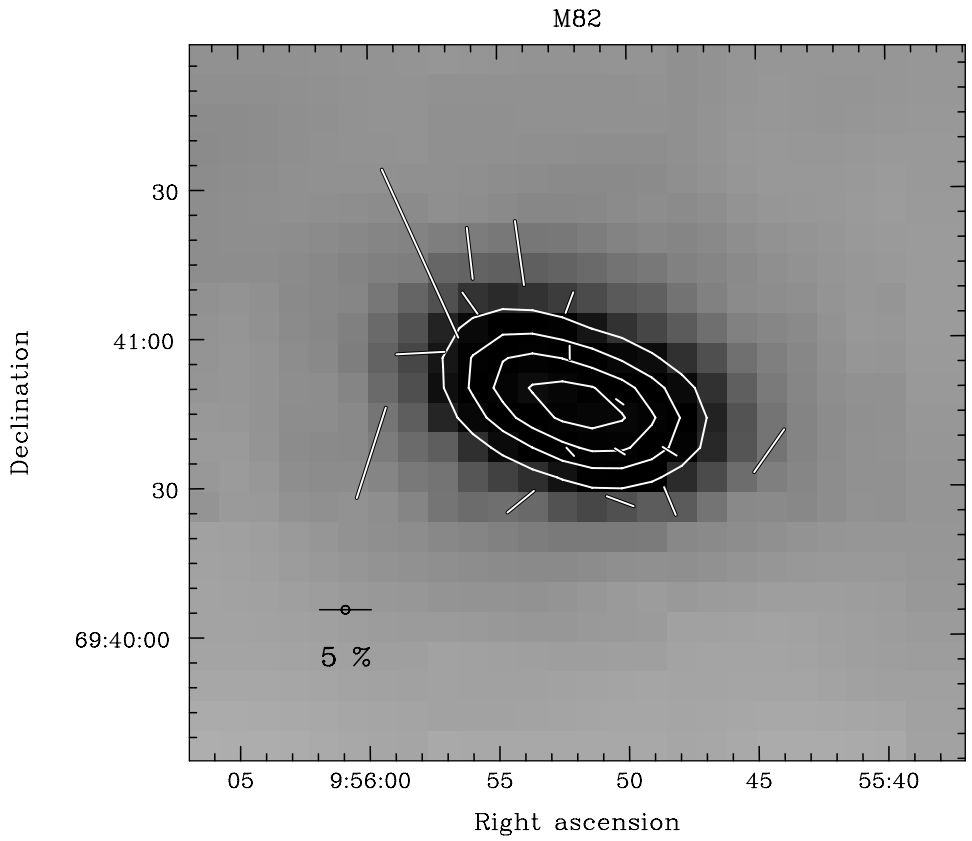

Figure 41. Compiled data toward the starburst galaxy M82. Contours range from 0.5 Jy beam^{-1} in steps of 0.25 Jy beam^{-1}. 850 μm polarization vectors are sampled on a 10″ grid. Vectors are plotted where $I > 0$, $p/dp > 2$, and $dp < 4\%$.

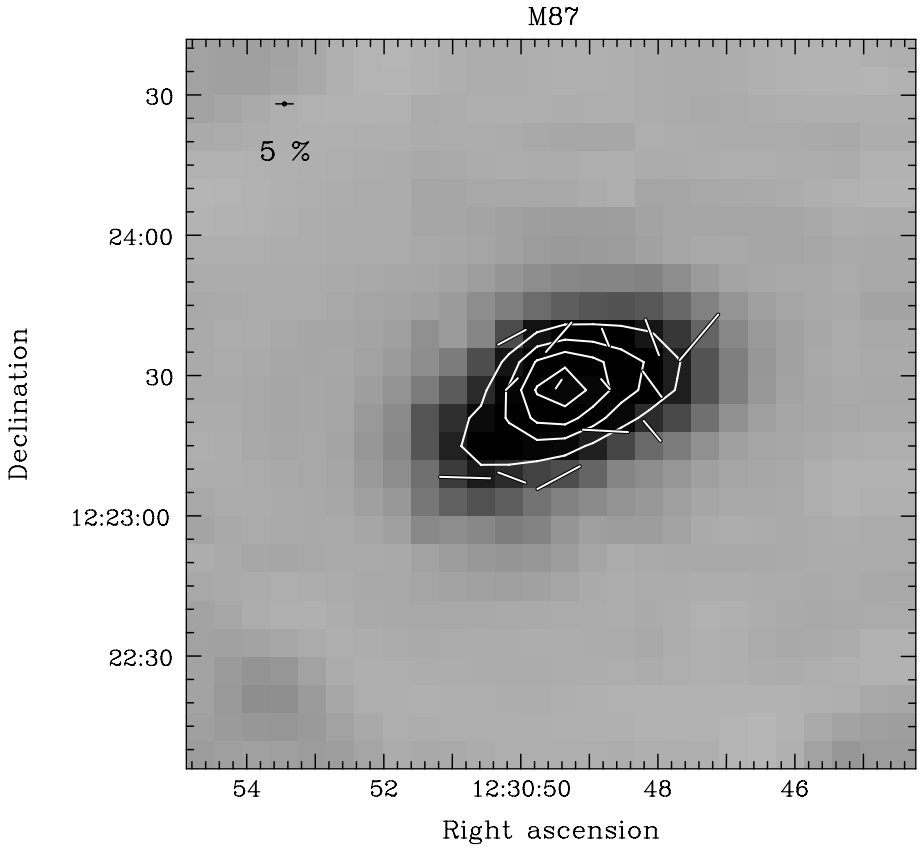

Figure 42. Compiled data toward the galaxy M87. Contours range from 0.2 Jy beam^{-1} in steps of 0.1 Jy beam^{-1}. 850 μm polarization vectors are sampled on a 10″ grid. Vectors are plotted where $I > 0$, $p/dp > 2$, and $dp < 4\%$.

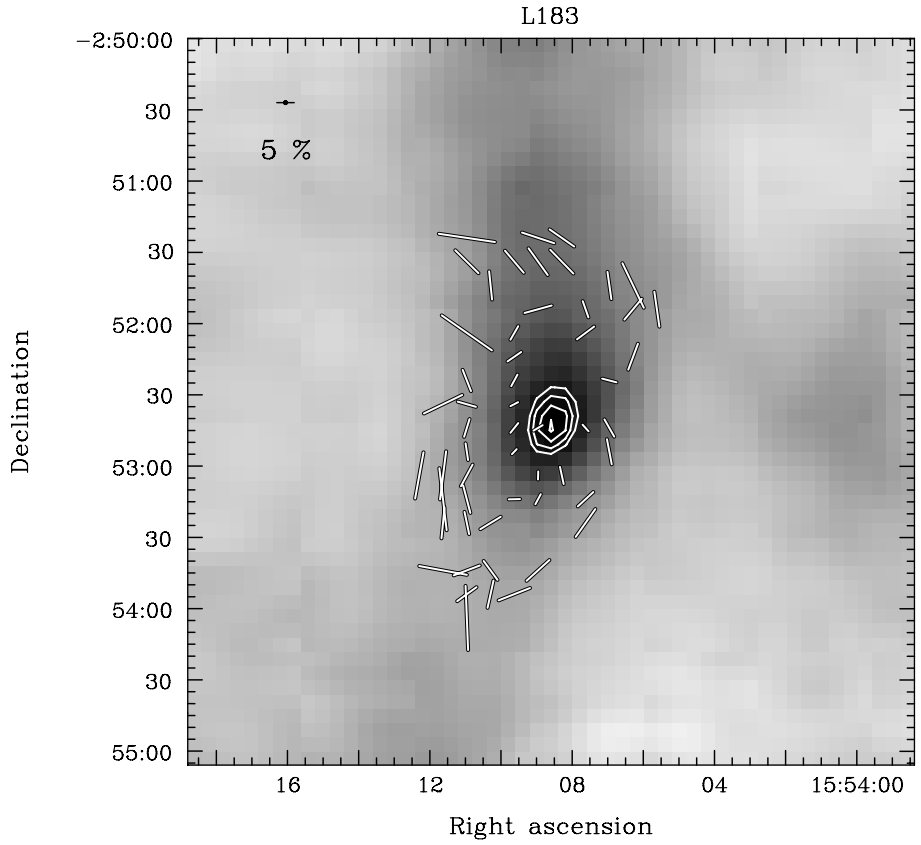

Figure 43. Compiled data toward the L183 core. Contours range from 0.2 Jy beam^{-1} in steps of 0.01 Jy beam^{-1}. 850 μm polarization vectors are sampled on a 10″ grid. Vectors are plotted where $I > 0$, $p/dp > 2$, and $dp < 4\%$.

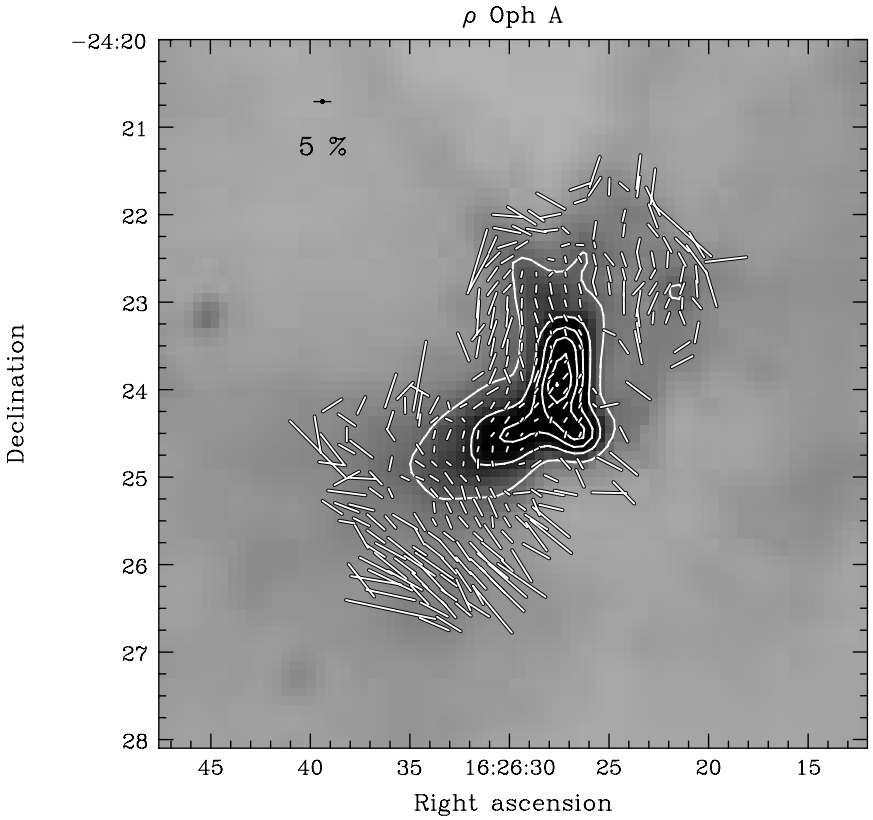

Figure 44. Compiled data toward the ρ Oph A core. Contours range from 0.5 Jy beam^{-1} in steps of 0.55 Jy beam^{-1}. 850 μm polarization vectors are sampled on a $10''$ grid. Vectors are plotted where $I > 0$, $p/dp > 2$, and $dp < 4\%$.

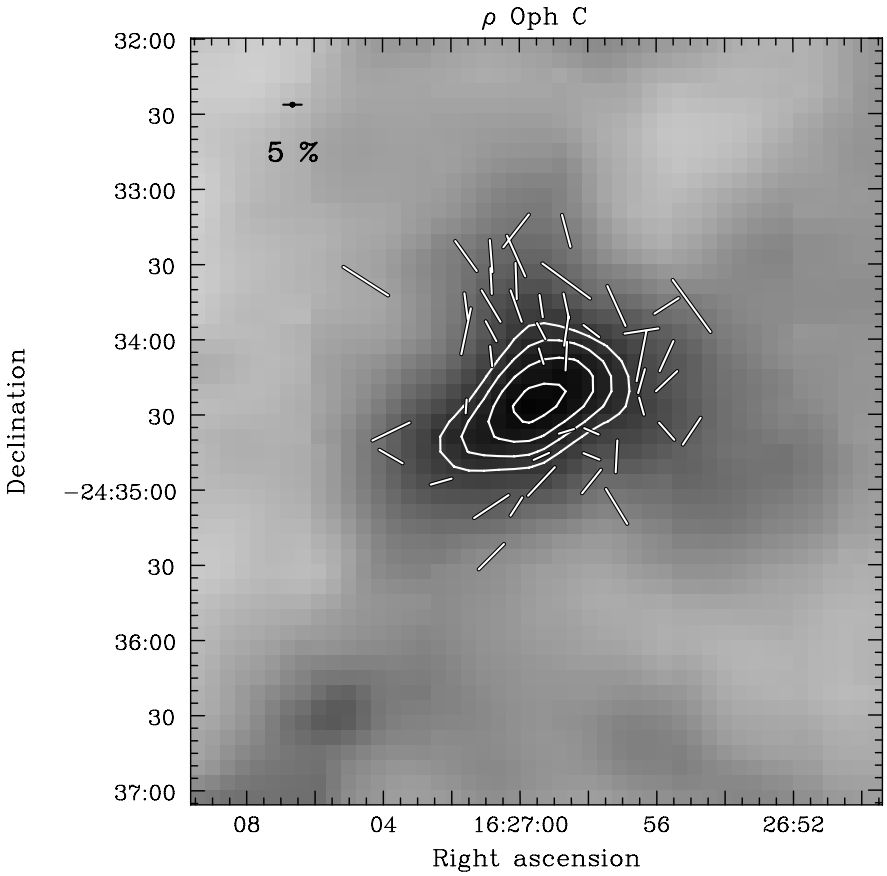

Figure 45. Compiled data toward the ρ Oph C core. Contours range from 0.3 Jy beam^{-1} in steps of 0.04 Jy beam^{-1}. 850 μm polarization vectors are sampled on a $10''$ grid. Vectors are plotted where $I > 0$, $p/dp > 2$, and $dp < 4\%$.

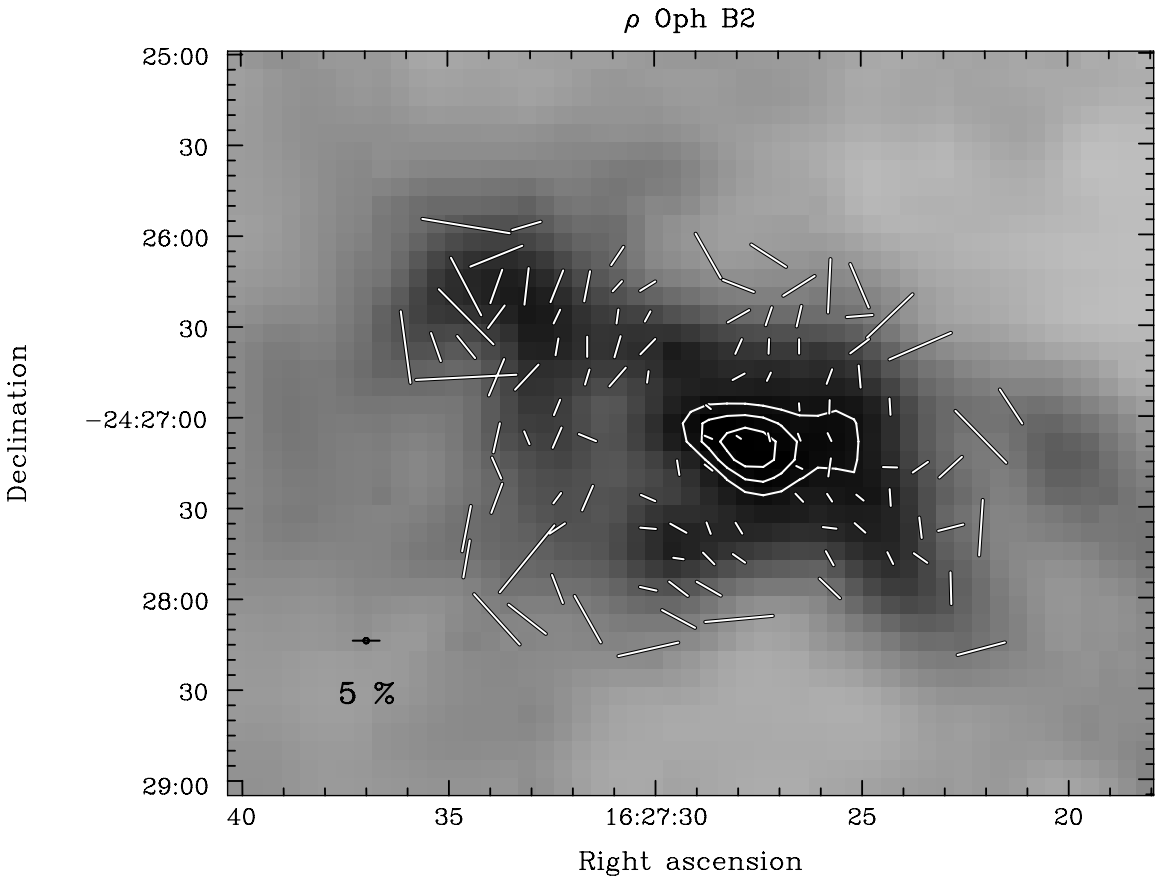

Figure 46. Compiled data toward the ρ Oph B2 core. Contours range from 0.6 Jy beam^{-1} in steps of 0.05 Jy beam^{-1}. 850 μm polarization vectors are sampled on a 10″ grid. Vectors are plotted where $I > 0$, $p/dp > 2$, and $dp < 4\%$.

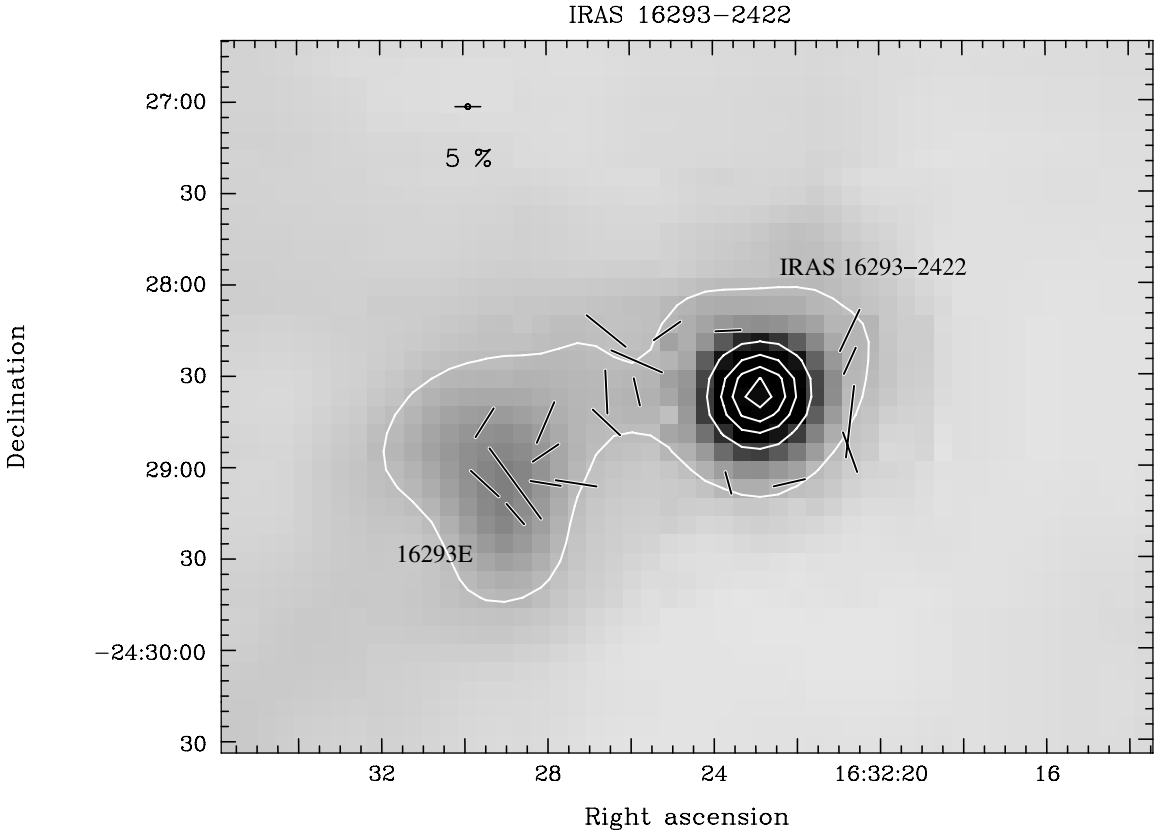

Figure 47. Compiled data toward the YSO IRAS 16293-2422. Contours range from 0.05 Jy beam^{-1} in steps of 2.0 Jy beam^{-1}. 850 μm polarization vectors are sampled on a 10″ grid. Vectors are plotted where $I > 0$, $p/dp > 2$, and $dp < 4\%$.

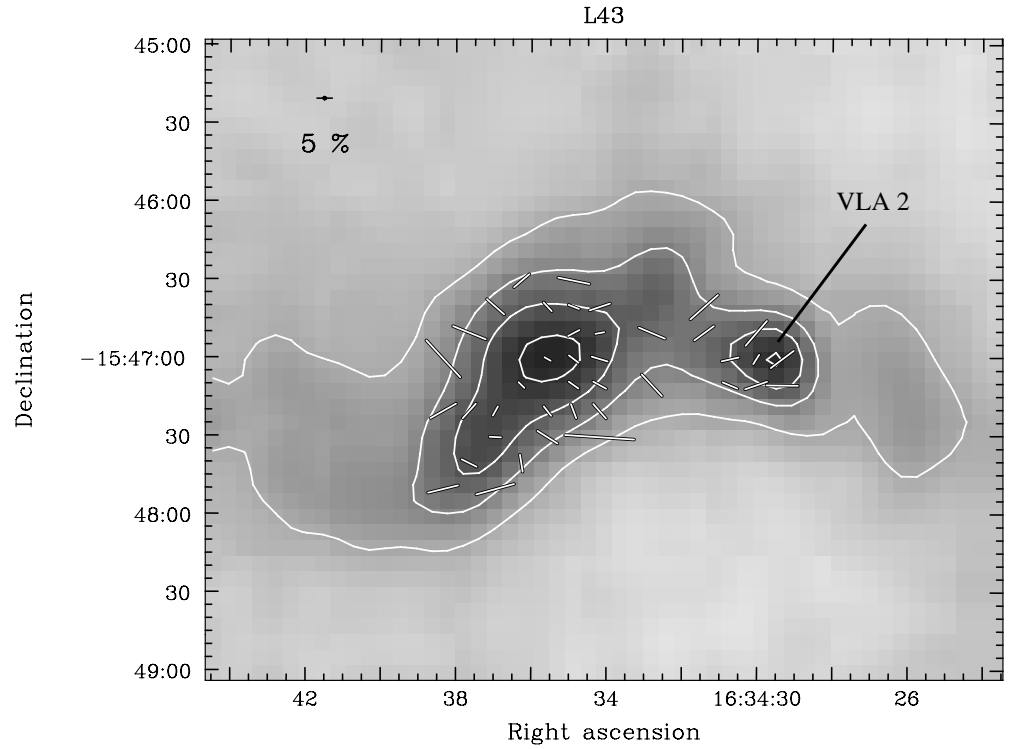

Figure 48. Compiled data toward the L43 core. Contours range from 0.1 Jy beam^{-1} in steps of 0.1 Jy beam^{-1}. 850 μm polarization vectors are sampled on a 10″ grid. Vectors are plotted where $I > 0$, $p/dp > 2$, and $dp < 4\%$.

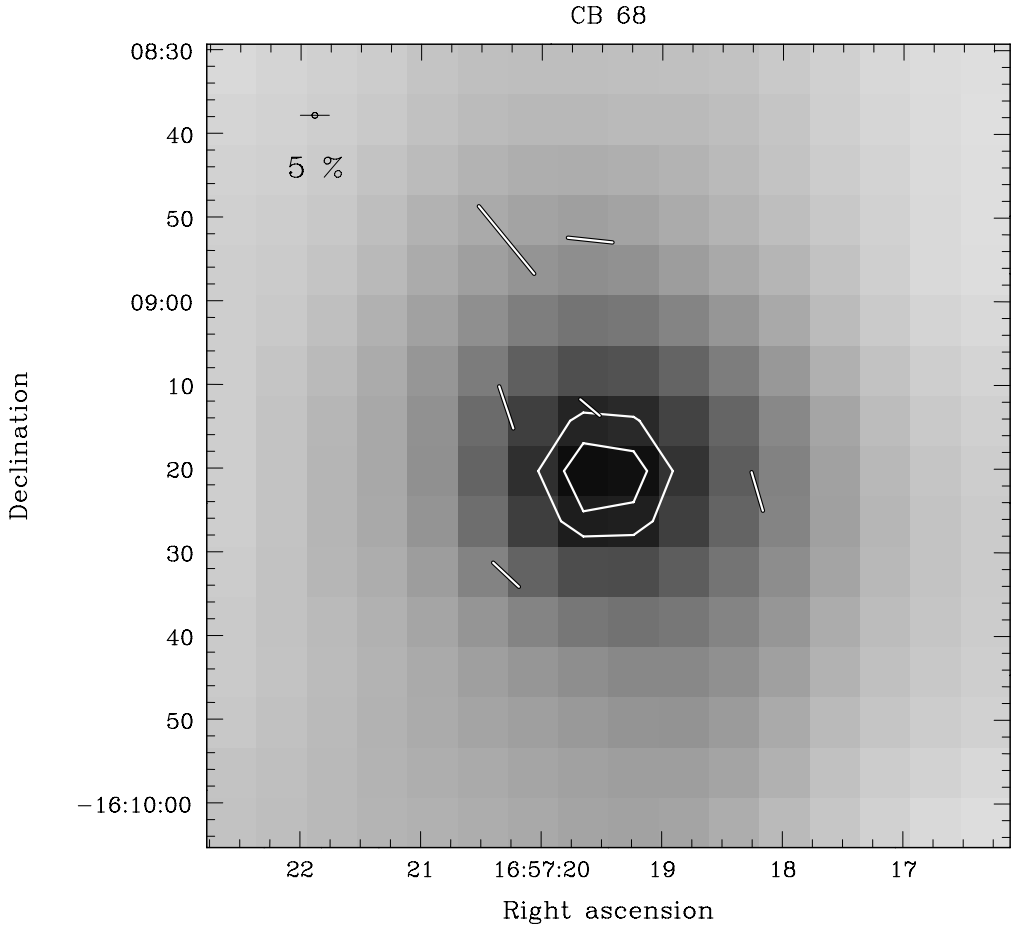

Figure 49. Compiled data toward the source CB 68. Contours range from 0.35 Jy beam^{-1} in steps of 0.035 Jy beam^{-1}. 850 μm polarization vectors are sampled on a 10″ grid. Vectors are plotted where $I > 0$, $p/dp > 2$, and $dp < 4\%$.

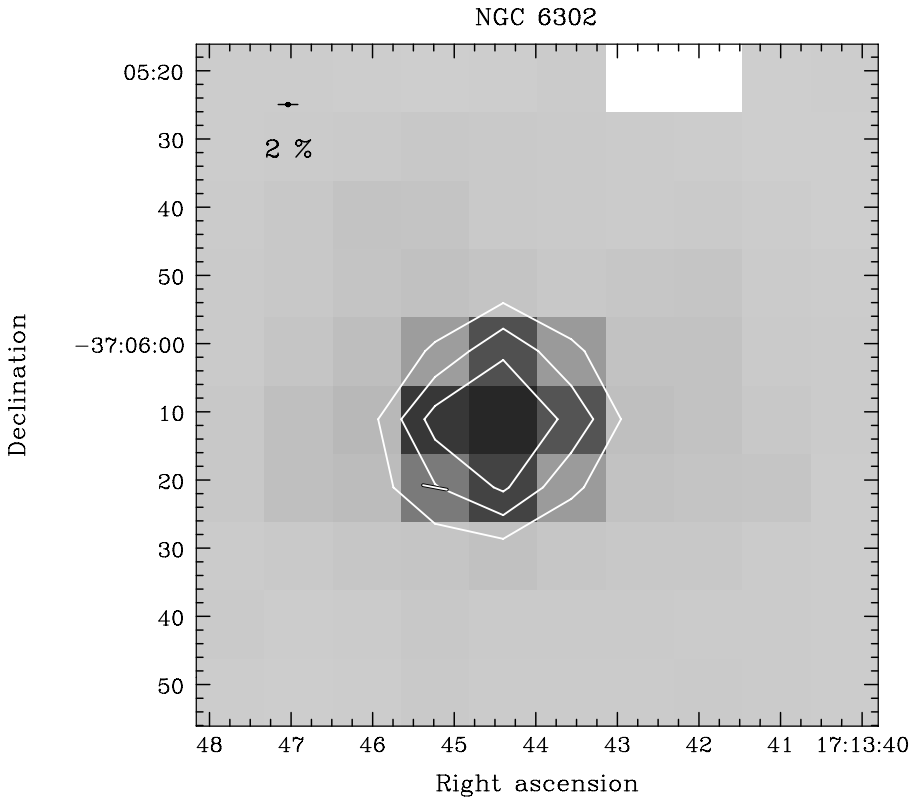

Figure 50. Compiled data toward the PN NGC 6302. The intensity data are taken from SCUPOL data, rather than the SCUBA Legacy Catalog. Contours range from 1.1 Jy beam^{-1} in steps of 1.1 Jy beam^{-1} where we have applied a flux conversion factor of 455 Jy beam^{-1} Volt^{-1} for conversion to flux density. 850 μm polarization vectors are sampled on a 10″ grid. Vectors are plotted where $I > 0$, $p/dp > 2$, and $dp < 4\%$.

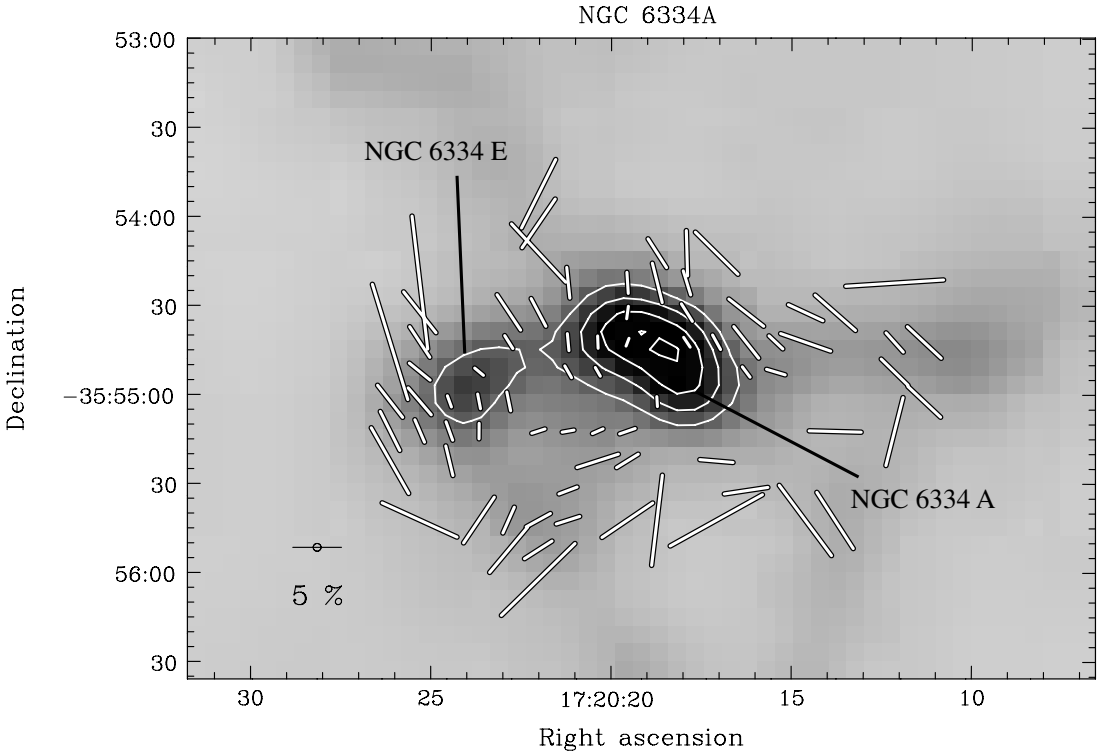

Figure 51. Compiled data toward the MSX (Midcourse Space Experiment[7]) dark cloud NGC 6334A (G351.161+00.697). Contours range from 5 Jy beam^{-1} in steps of 2.5 Jy beam^{-1}. 850 μm polarization vectors are sampled on a 10″ grid. Vectors are plotted where $I > 0$, $p/dp > 2$, and $dp < 4\%$.

[7] http://www.ipac.caltech.edu/ipac/msx/msx.html

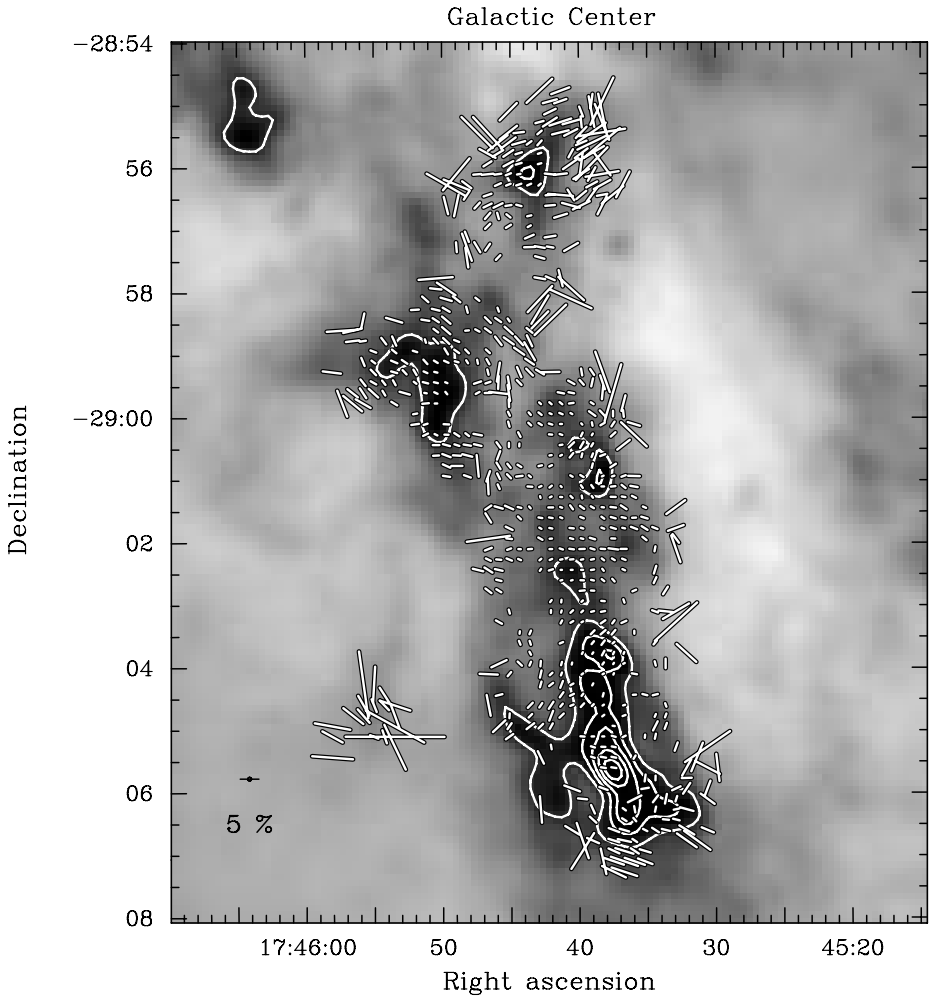

Figure 52. Compiled data toward the GC. The gray-scale map is a SCUBA calibrated map from Di Francesco et al. (2008). Contours range from 2 Jy beam^{-1} in steps of 1 Jy beam^{-1}. 850 μm polarization vectors are sampled on a 10″ grid. Vectors are plotted where $I > 0$, $p/dp > 2$, and $dp < 4\%$.

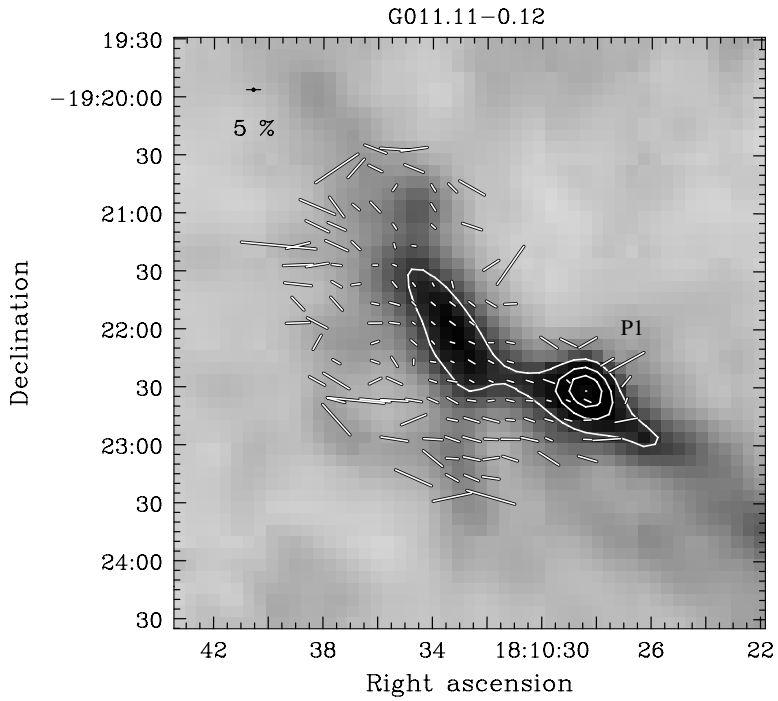

Figure 53. Compiled data toward the MSX dark filament G011.11-0.12. Contours range from 0.5 Jy beam^{-1} in steps of 0.25 Jy beam^{-1}. 850 μm polarization vectors are sampled on a 10″ grid. Vectors are plotted where $I > 0$, $p/dp > 2$, and $dp < 4\%$.

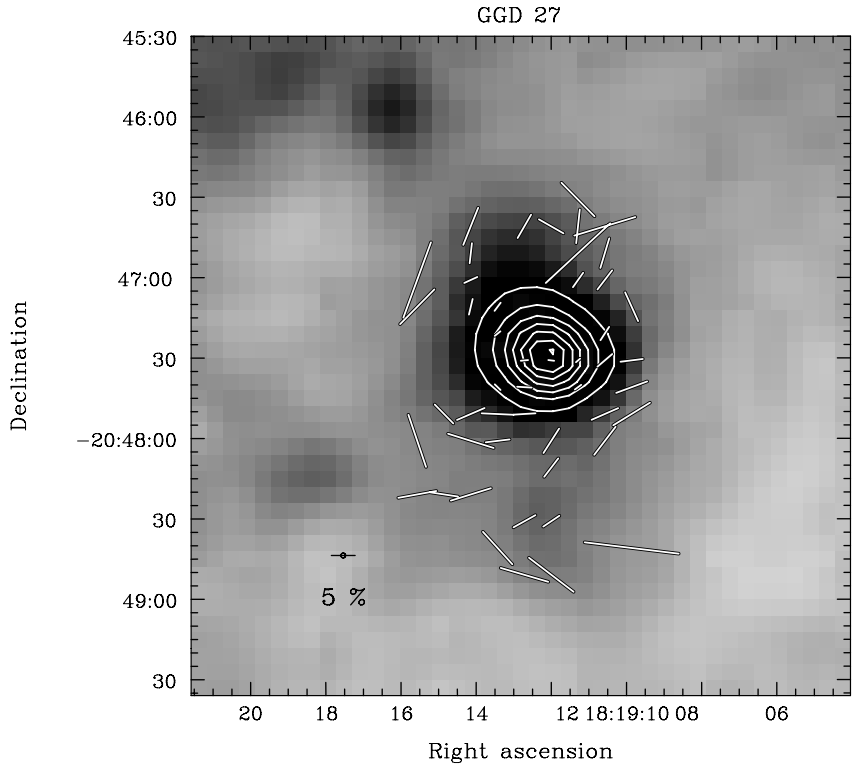

Figure 54. Compiled data toward the source GGD27 IRS1. Contours range from 0.5 Jy beam^{-1} in steps of 0.5 Jy beam^{-1}. 850 μm polarization vectors are sampled on a 10″ grid. Vectors are plotted where $I > 0$, $p/dp > 2$, and $dp < 4\%$.

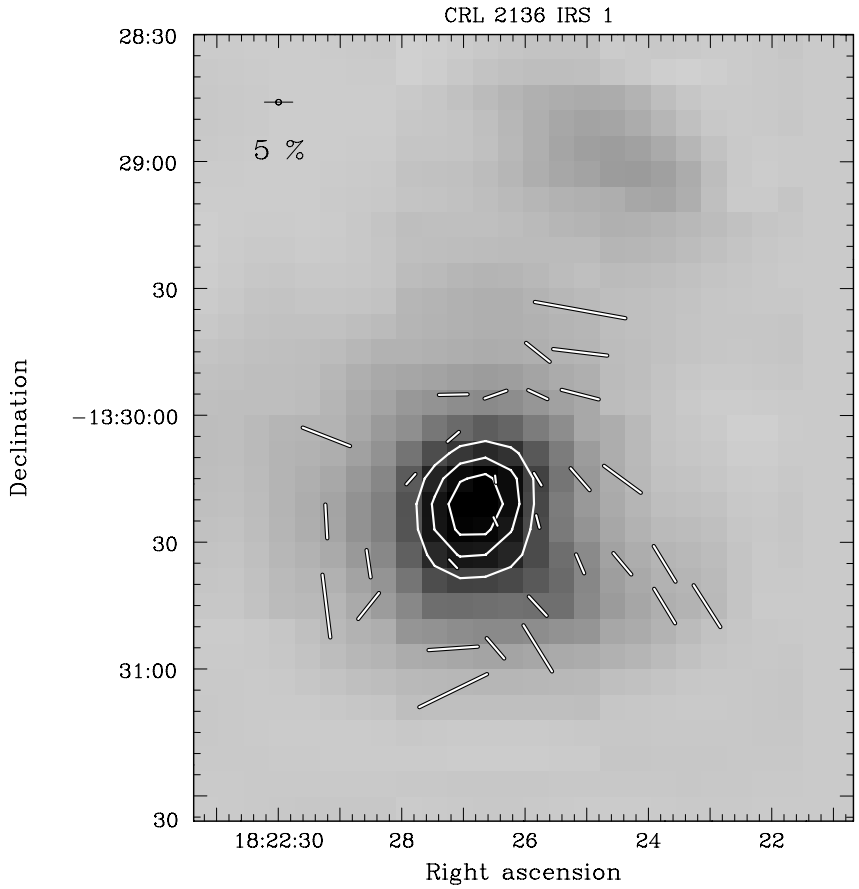

Figure 55. Compiled data toward the source CRL 2136 IRS 1. Contours range from 1.4 Jy beam^{-1} in steps of 0.4 Jy beam^{-1}. 850 μm polarization vectors are sampled on a 10″ grid. Vectors are plotted where $I > 0$, $p/dp > 2$, and $dp < 4\%$.

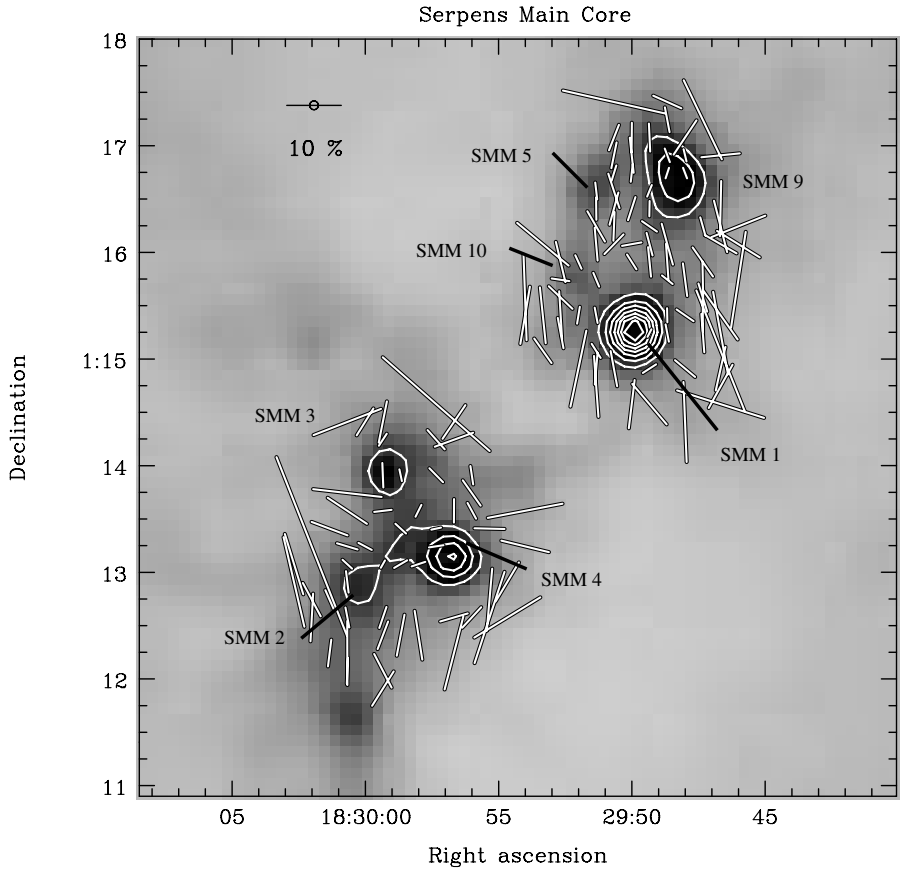

Figure 56. Compiled data toward the Serpens Main Core. Core desigations are taken from Davis et al. (1999). Contours range from 1 Jy beam^{-1} in steps of 0.5 Jy beam^{-1}. 850 μm polarization vectors are sampled on a 10″ grid. Vectors are plotted where $I > 0$, $p/dp > 3$, and $dp < 3\%$. The different vector selection criteria are due to the high number of noisy vectors that exist at the 2 σ cutoff.

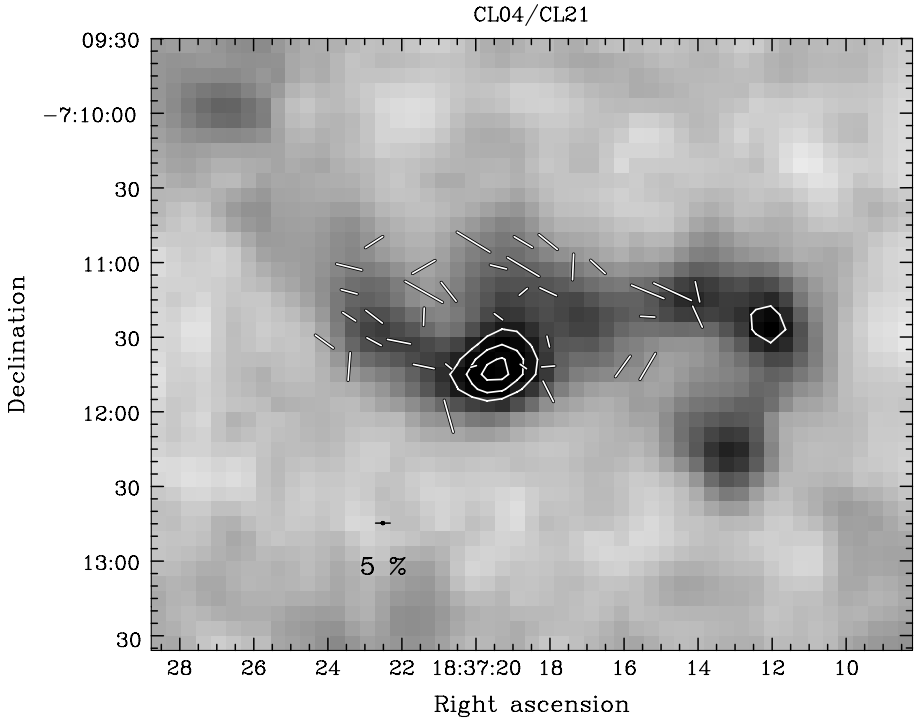

Figure 57. Compiled data toward the CL 04/CL 21 cloud. Contours range from 0.3 Jy beam^{-1} in steps of 0.1 Jy beam^{-1}. 850 μm polarization vectors are sampled on a 10″ grid. Vectors are plotted where $I > 0$, $p/dp > 2$, and $dp < 4\%$.

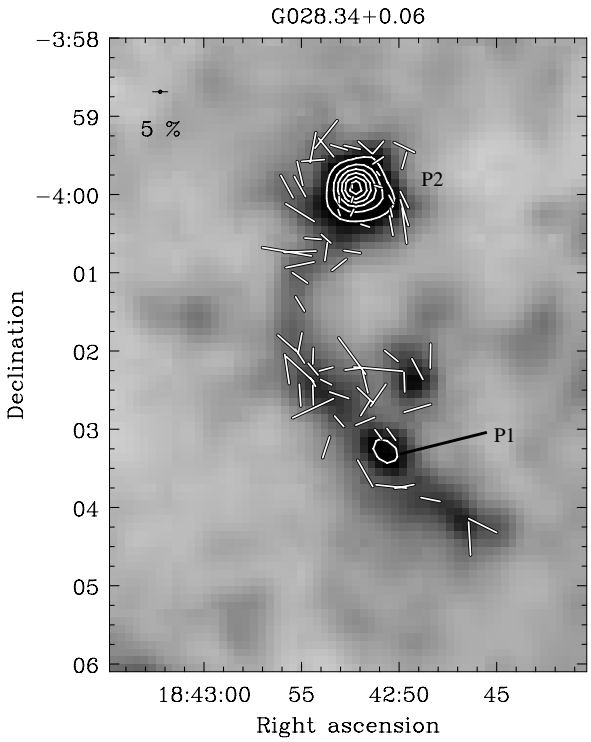

Figure 58. Compiled data toward the MSX dark cloud G028.34+0.06. Core designations from Carey et al. (2000). Contours range from 1 Jy beam^{-1} in steps of 0.5 Jy beam^{-1}. 850 μm polarization vectors are sampled on a 10″ grid. Vectors are plotted where $I > 0$, $p/dp > 2$, and $dp < 4\%$.

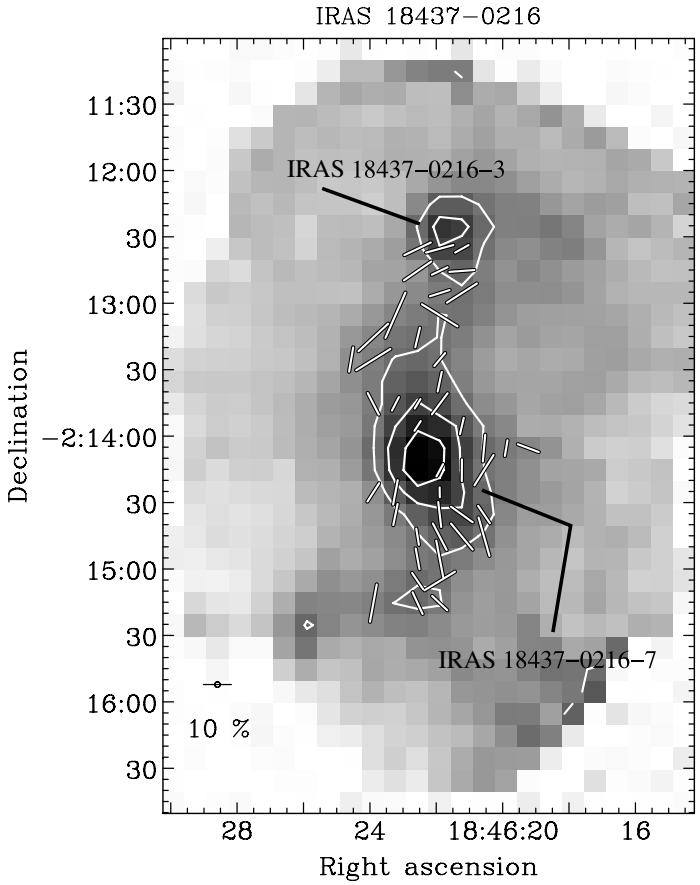

Figure 59. Compiled data toward the source IRAS 18437-0216. The cores are high-mass SC candidates 33 and 34, respectively, as identified by Sridharan et al. (2005). The intensity data are taken from SCUPOL data, rather than the SCUBA Legacy Catalog. Contours range from 0.5 Jy beam^{-1} in steps of 0.25 Jy beam^{-1} where we have used a flux conversion factor of 455 Jy beam^{-1} V^{-1}. 850 μm polarization vectors are sampled on a 10″ grid. Vectors are plotted where $I > 0$, $p/dp > 2$, and $dp < 4\%$. Although this source is in the SCUBA data archive Di Francesco et al. (2008), the polarimetry mapping was more extensive.

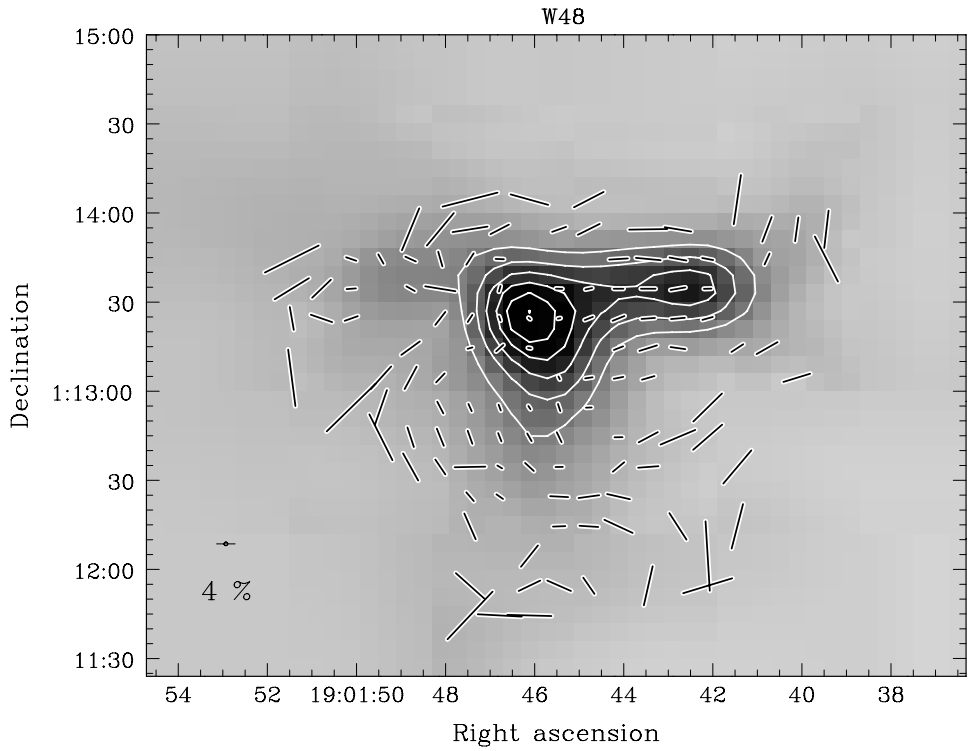

Figure 60. Compiled data toward the SFR W48. The western core, W48 West, is a candidate HMPO identified by Curran et al. (2004). Contours range from 2 Jy beam^{-1} in steps of 1 Jy beam^{-1}. 850 μm polarization vectors are sampled on a 10″ grid. Vectors are plotted where $I > 0$, $p/dp > 2$, and $dp < 4\%$.

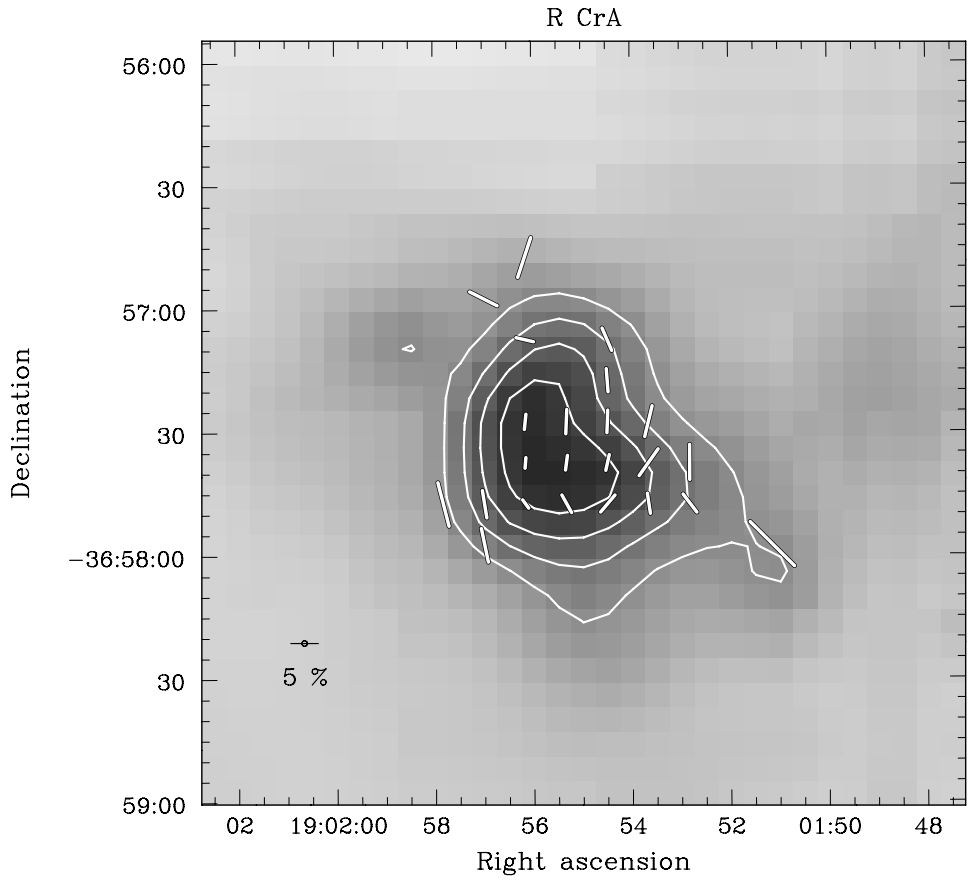

Figure 61. Compiled data toward the source R Corona Australis. Contours range from 1 Jy beam^{-1} in steps of 0.4 Jy beam^{-1}. 850 μm polarization vectors are sampled on a 10″ grid. Vectors are plotted where $I > 0$, $p/dp > 2$, and $dp < 4\%$.

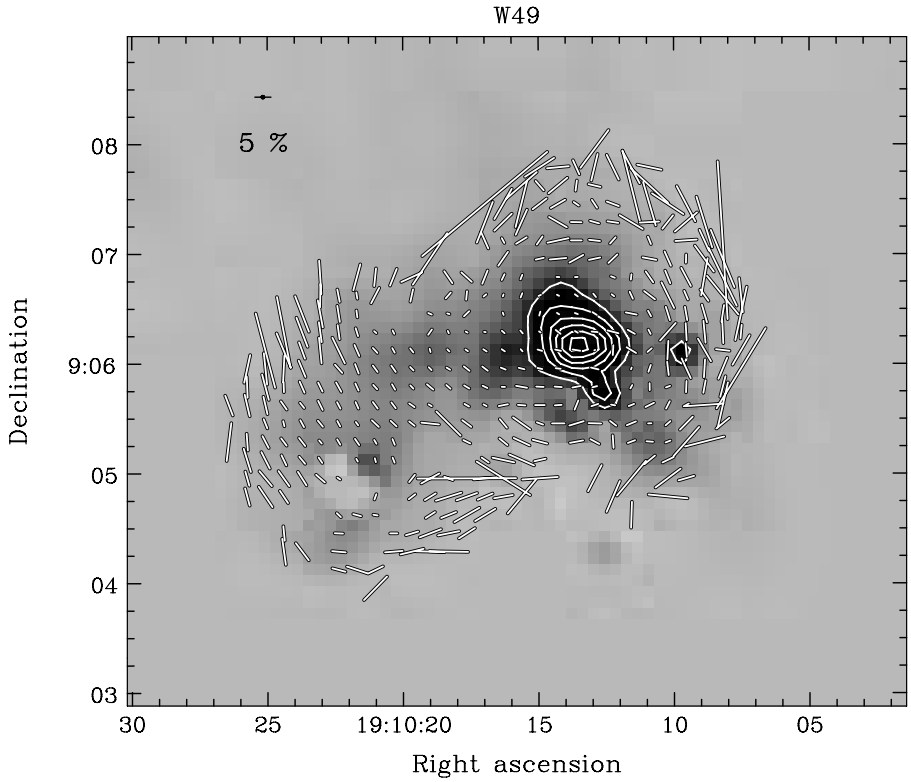

Figure 62. Compiled data toward the SFR W49. Contours range from 6 Jy beam^{-1} in steps of 3 Jy beam^{-1}. 850 μm polarization vectors are sampled on a 10″ grid. Vectors are plotted where $I > 0$, $p/dp > 2$, and $dp < 4\%$.

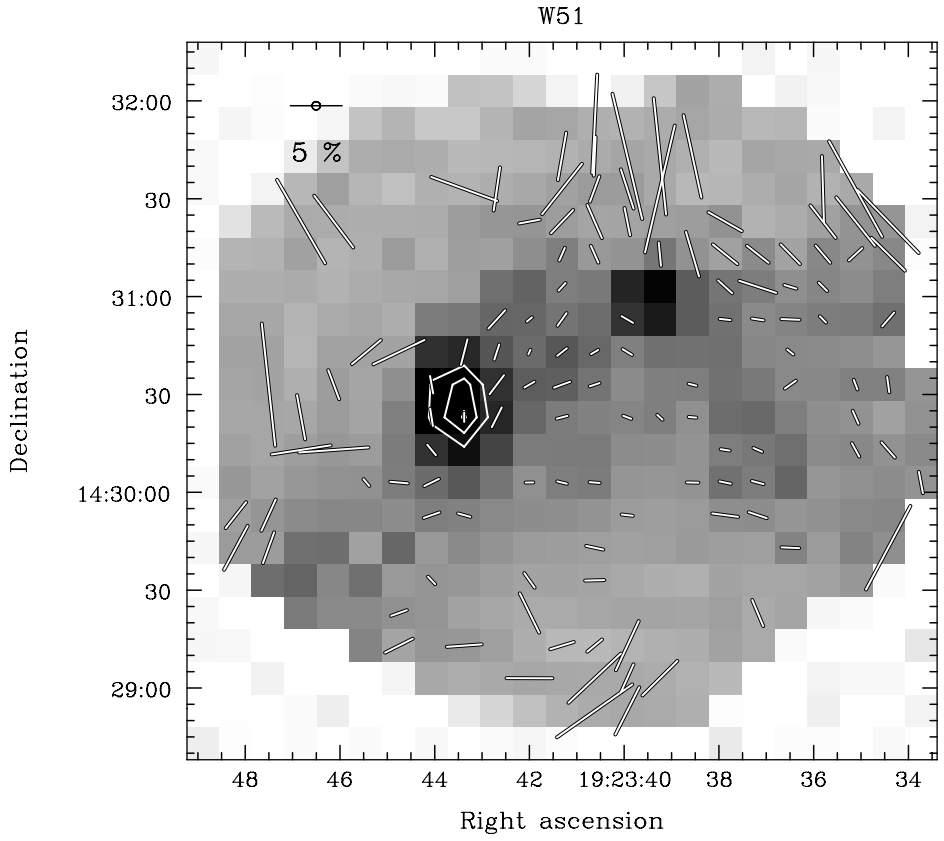

Figure 63. Compiled data toward the SFR W51. Contours range from 0.1 Jy beam^{-1} in steps of 0.025 Jy beam^{-1}. 850 μm polarization vectors are sampled on a 10″ grid. Vectors are plotted where $I > 0$, $p/dp > 2$, and $dp < 4\%$.

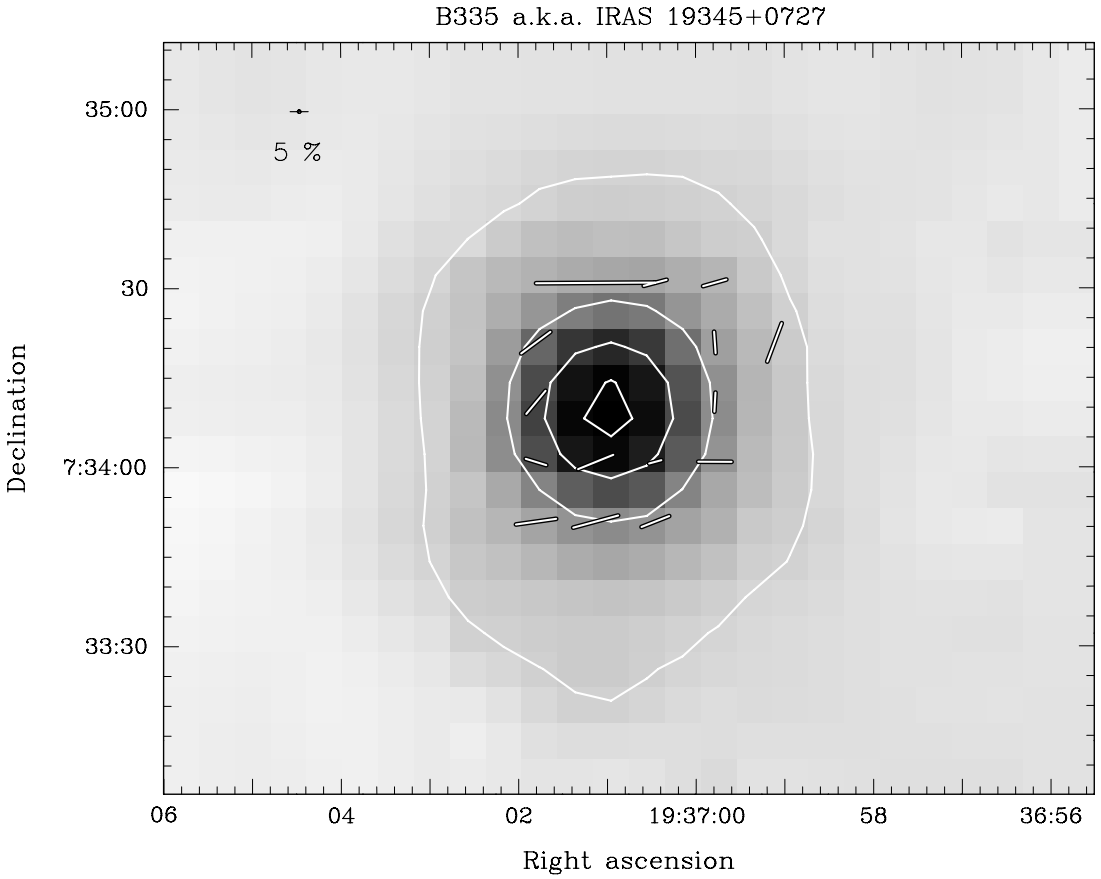

Figure 64. Compiled data toward the source B335. Contours range from 0.02 Jy beam^{-1} in steps of 0.2 Jy beam^{-1}. 850 μm polarization vectors are sampled on a 10″ grid. Vectors are plotted where $I > 0$, $p/dp > 2$, and $dp < 4\%$.

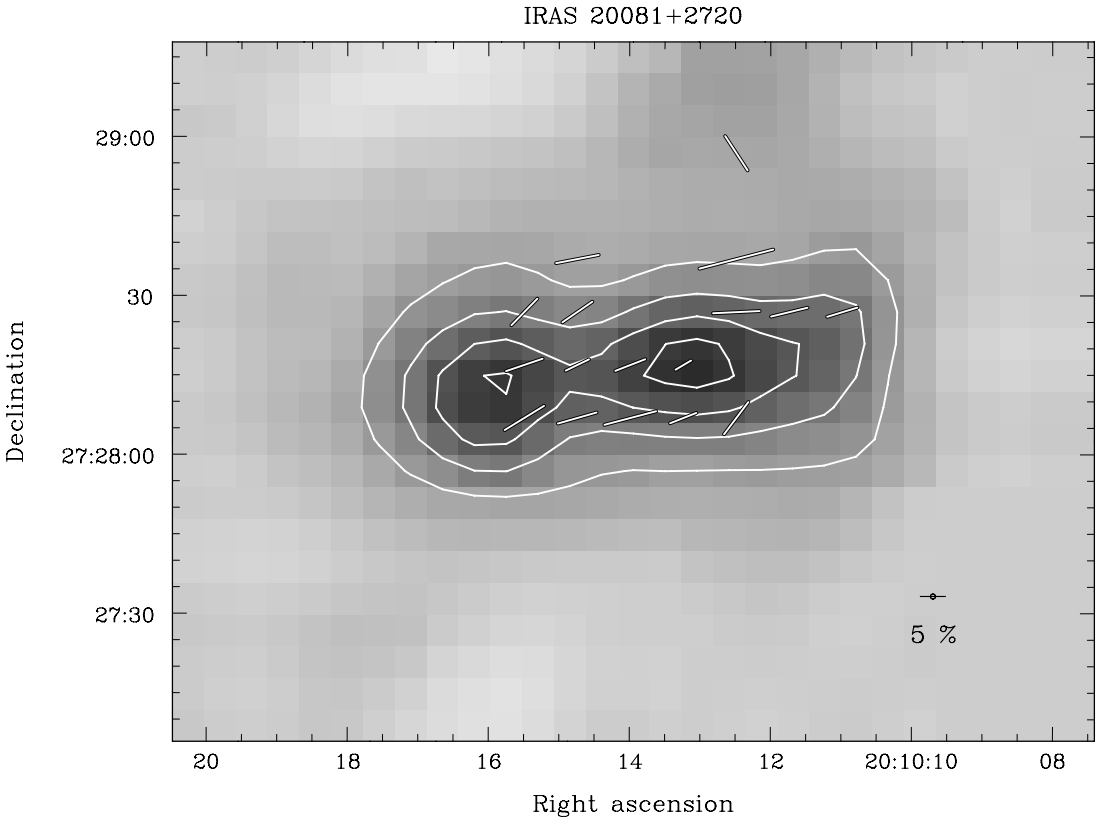

Figure 65. Compiled data toward the source IRAS 20081+2720. Contours range from 0.15 Jy beam^{-1} in steps of 0.1 Jy beam^{-1}. 850 μm polarization vectors are binned to 18.5″ spacing. Vectors are plotted where $I > 0$, $p/dp > 2$, and $dp < 4\%$.

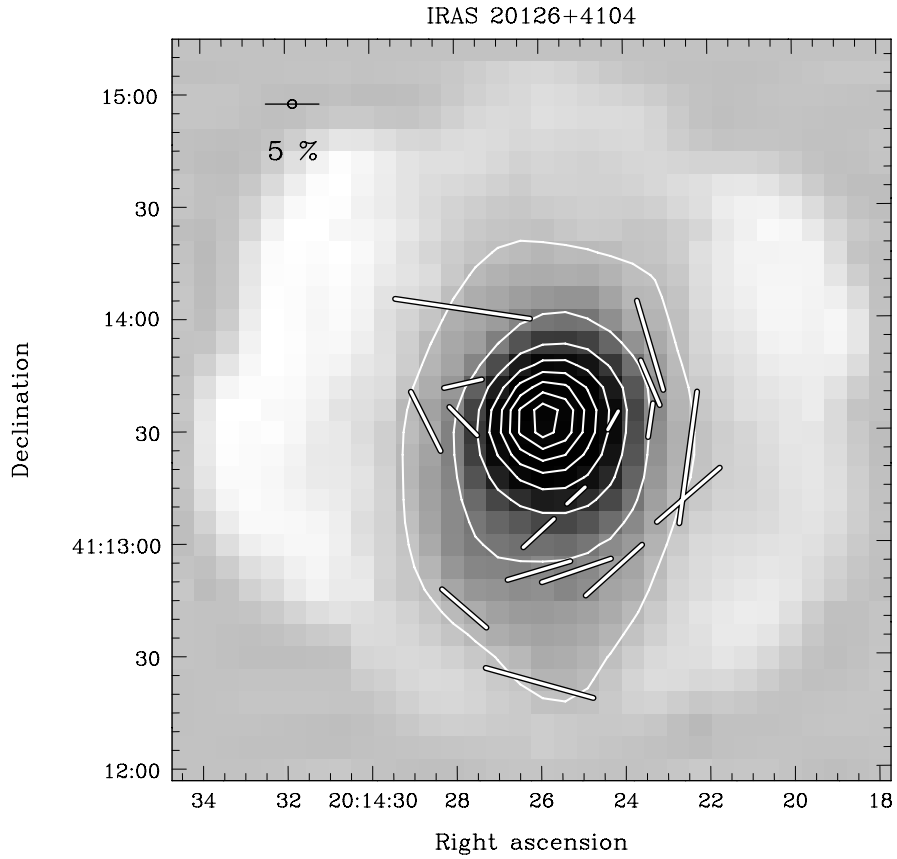

Figure 66. Compiled data toward the source IRAS 20126+4104. Contours range from 0.02 Jy beam^{-1} in steps of 0.04 Jy beam^{-1}. 850 μm polarization vectors are sampled on a 10″ grid. Vectors are plotted where $I > 0$, $p/dp > 2$, and $dp < 4\%$.

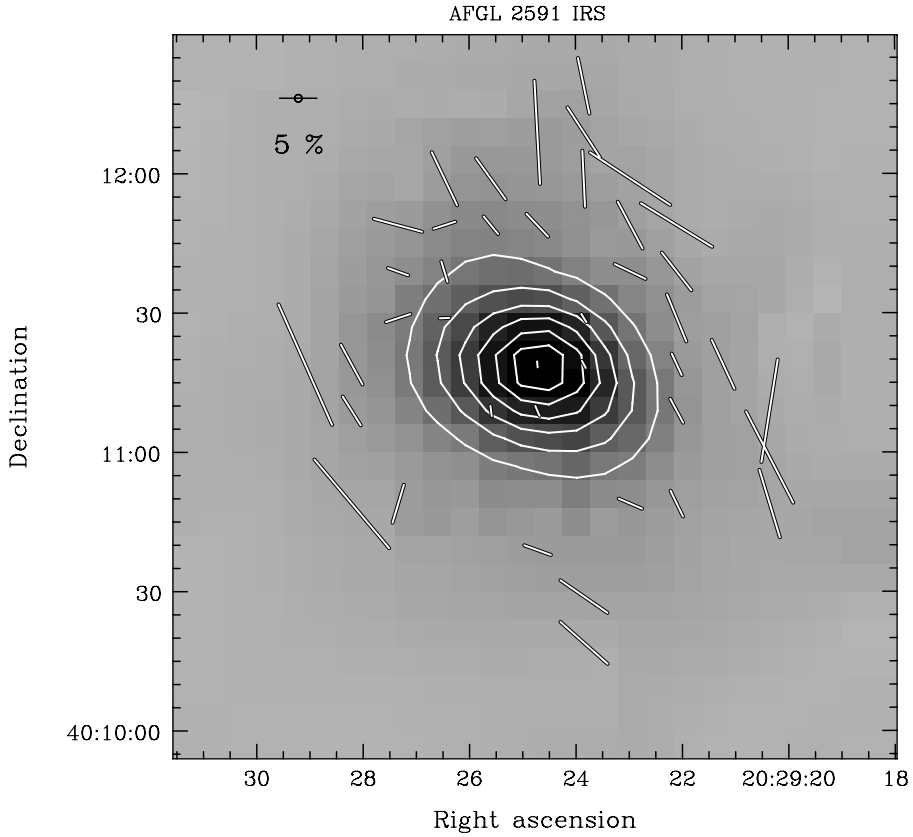

Figure 67. Compiled data toward the AFGL 2591 IRS source. Contours range from 1 Jy beam^{-1} in steps of 0.5 Jy beam^{-1}. 850 μm polarization vectors are sampled on a 10″ grid. Vectors are plotted where $I > 0$, $p/dp > 2$, and $dp < 4\%$.

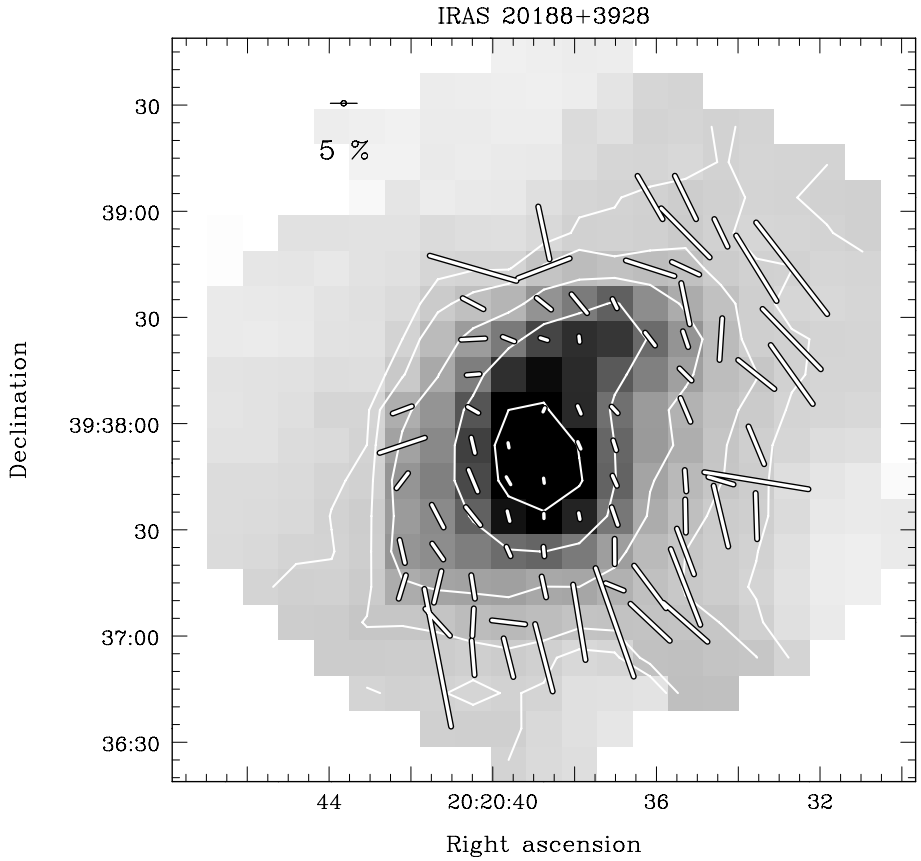

Figure 68. Compiled data toward the source IRAS 20188+3928. The intensity data are taken from SCUPOL data, rather than the SCUBA Legacy Catalog. Contours plotted have values of 0.72, 0.98, 1.8, 3.6 and 6.7 Jy beam^{-1} where we have used a flux conversion factor of 557 Jy beam^{-1} V^{-1}. 850 μm polarization vectors are sampled on a 10″ grid. Vectors are plotted where $I > 0$, $p/dp > 2$, and $dp < 4\%$.

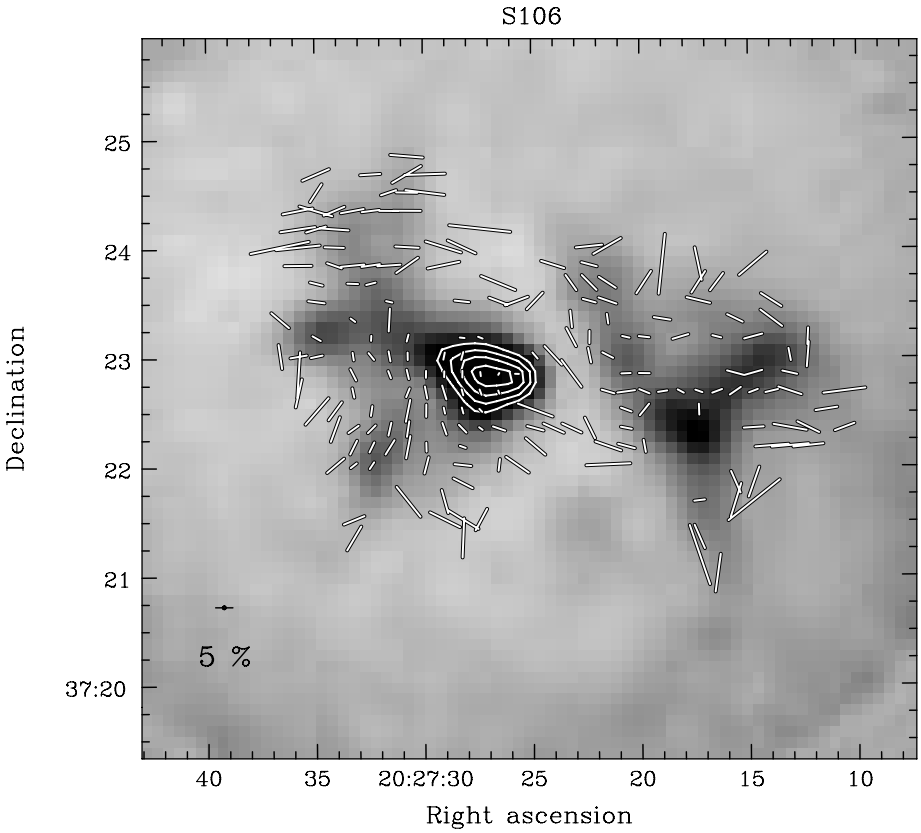

Figure 69. Compiled data toward the SFR S106. Contours range from 1.5 Jy beam^{-1} in steps of 0.5 Jy beam^{-1}. 850 μm polarization vectors are sampled on a 10″ grid. Vectors are plotted where $I > 0$, $p/dp > 2$, and $dp < 4\%$.

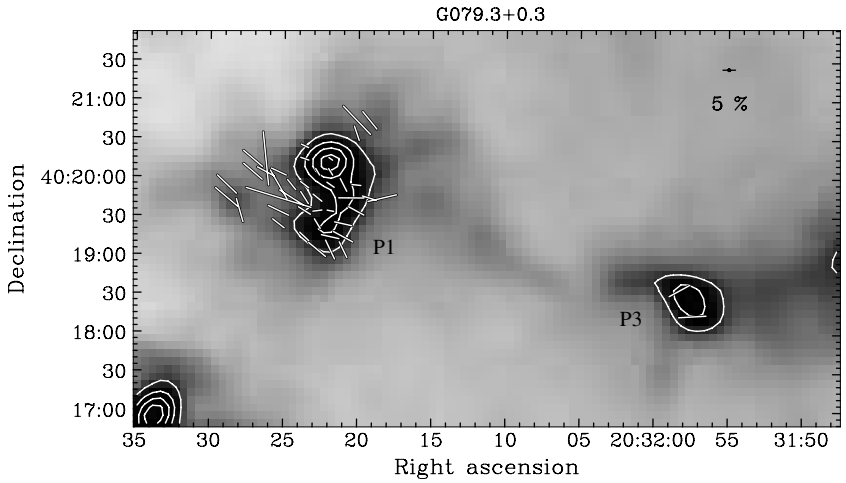

Figure 70. Compiled data toward the MSX cloud G079.3+0.3. Contours range from 0.5 Jy beam^{-1} in steps of 0.25 Jy beam^{-1}. 850 μm polarization vectors are sampled on a 10″ grid. Vectors are plotted where $I > 0$, $p/dp > 2$, and $dp < 4\%$.

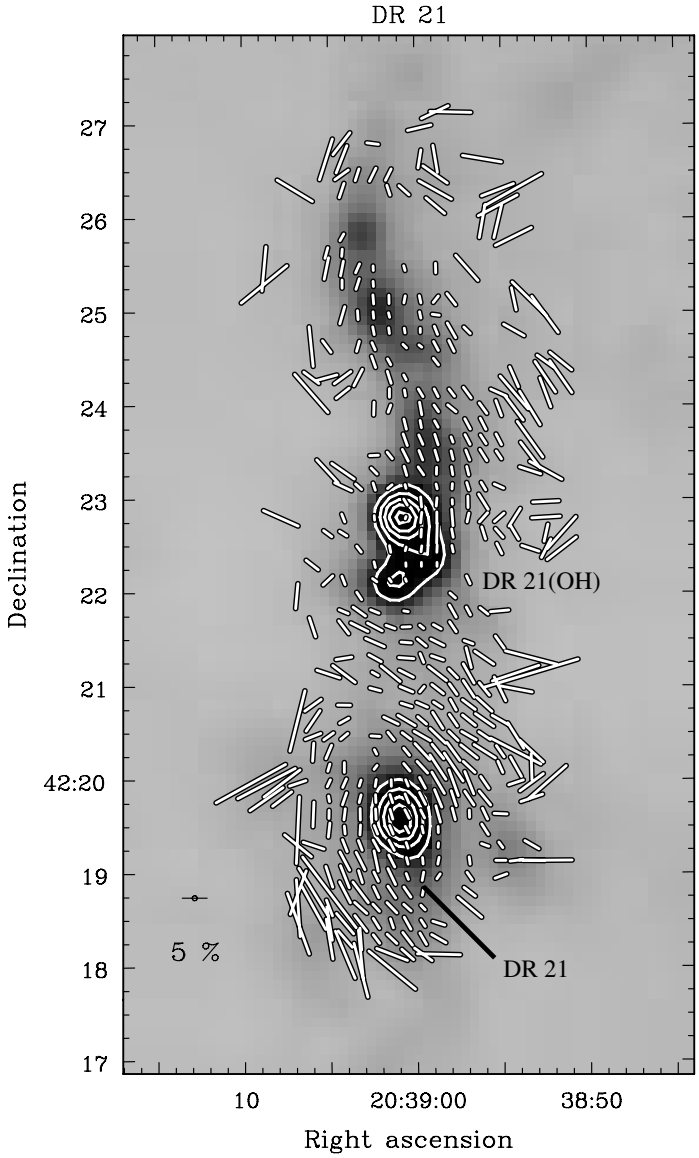

Figure 71. Compiled data toward the high-mass star-forming filament DR 21. Contours range from 5 Jy beam^{-1} in steps of 2.5 Jy beam^{-1}. 850 μm polarization vectors are sampled on a 10″ grid. Vectors are plotted where $I > 0$, $p/dp > 2$, and $dp < 4\%$.

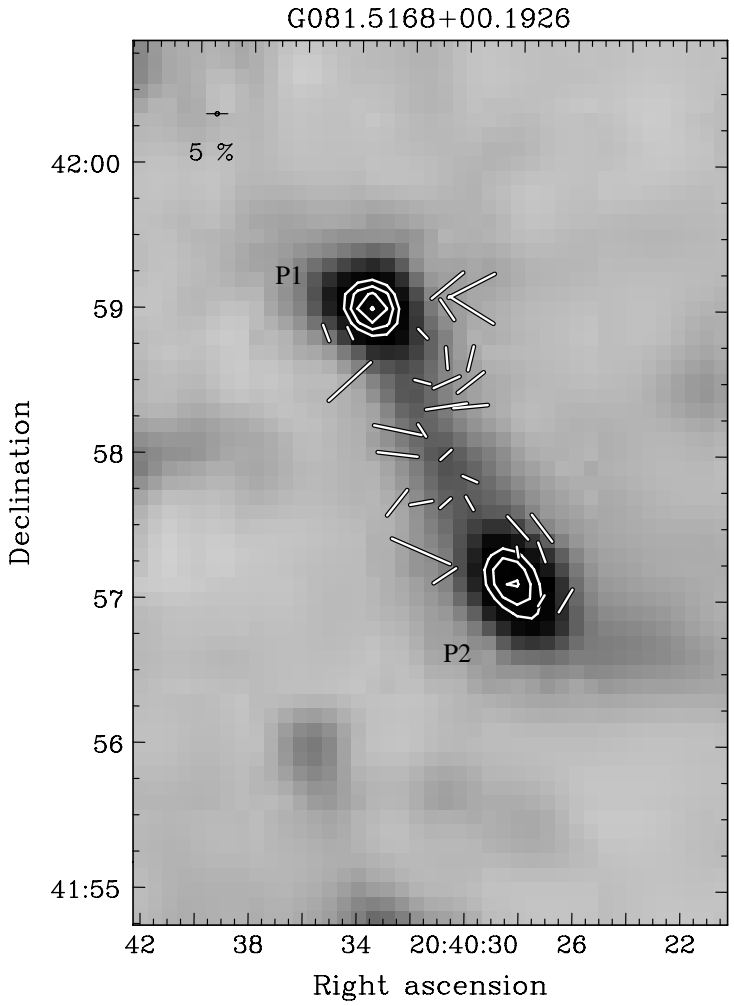

Figure 72. Compiled data toward the MSX cloud G81.56+0.10. Core designations are from Feldman et al. (2003). Contours range from 0.1 Jy beam^{-1} in steps of 0.2 Jy beam^{-1}. 850 μm polarization vectors are sampled on a 10″ grid. Vectors are plotted where $I > 0$, $p/dp > 2$, and $dp < 4\%$.

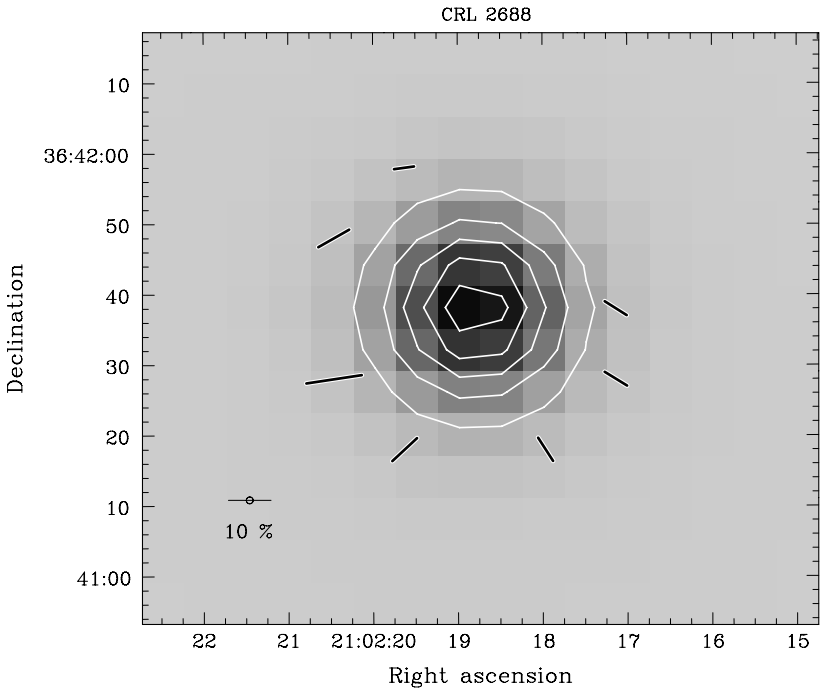

Figure 73. Compiled data toward the post-AGB star CRL 2688. Contours range from 0.5 Jy beam^{-1} in steps of 0.5 Jy beam^{-1}. 850 μm polarization vectors are sampled on a 10″ grid. Vectors are plotted where $I > 0$, $p/dp > 2$, and $dp < 4\%$.

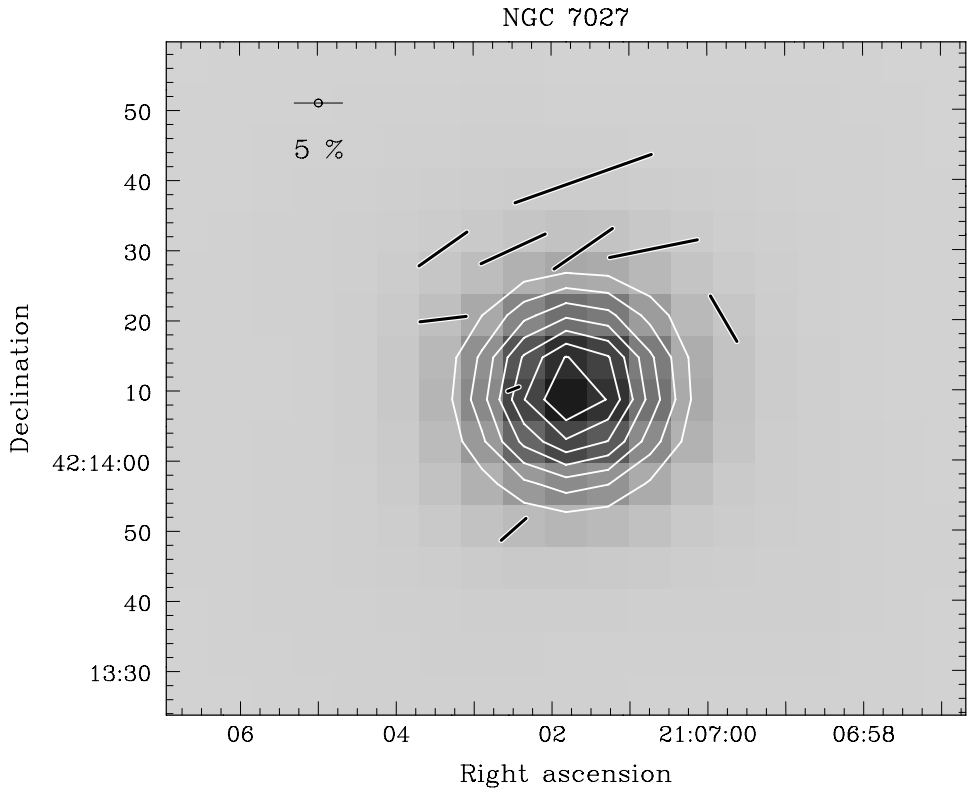

Figure 74. Compiled data toward the PN NGC 7027. Contours range from 0.5 Jy beam^{-1} in steps of 0.25 Jy beam^{-1}. 850 μm polarization vectors are sampled on a 10″ grid. Vectors are plotted where $I > 0$, $p/dp > 2$, and $dp < 4\%$.

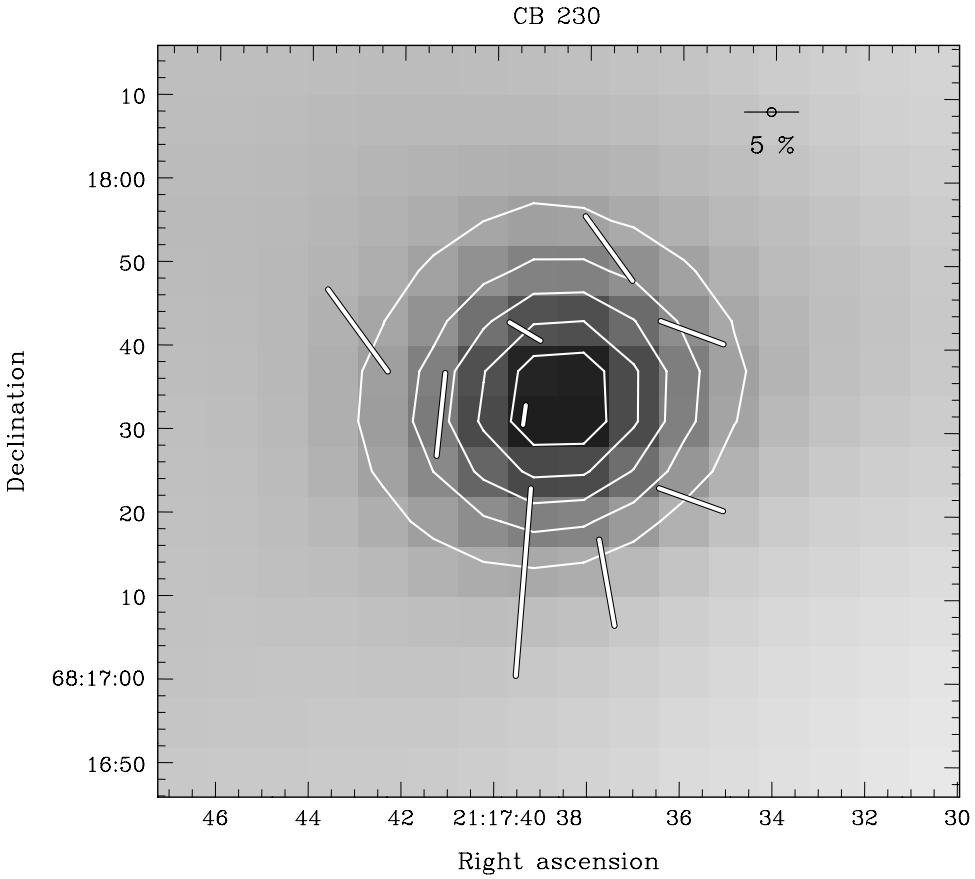

Figure 75. Compiled data toward the source CB 230. Contours range from 0.1 Jy beam^{-1} in steps of 0.1 Jy beam^{-1}. 850 μm polarization vectors are binned to 18.5″ spacing. Vectors are plotted where $I > 0$, $p/dp > 2$, and $dp < 4\%$.

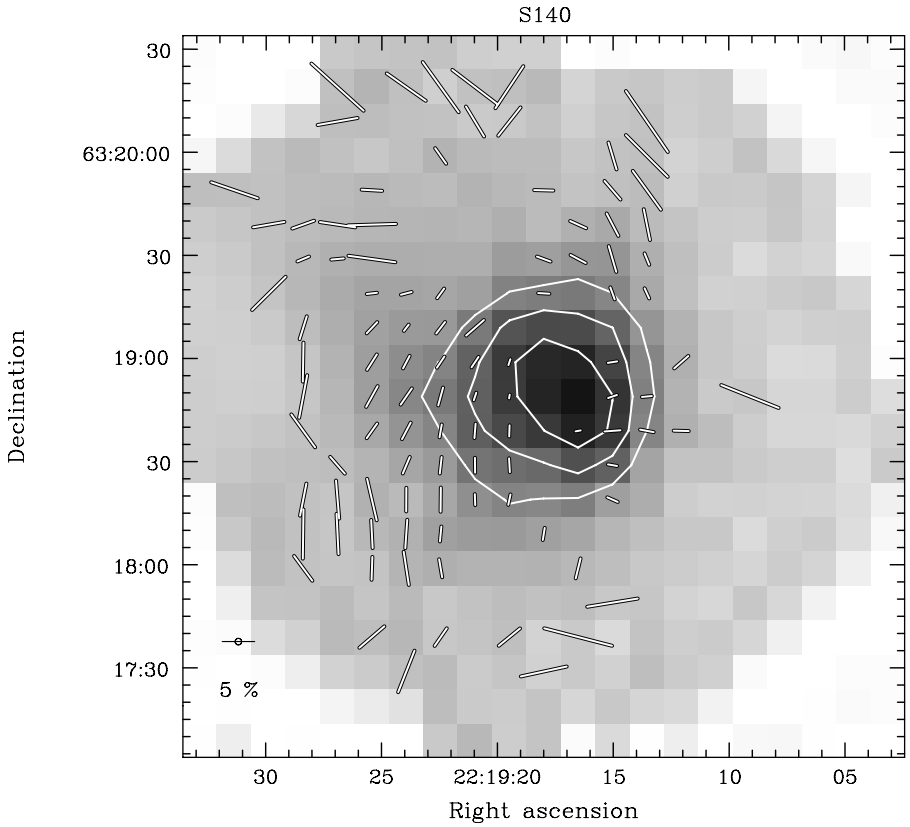

Figure 76. Compiled data toward the SFR S140. Contours range from 0.01 Jy beam^{-1} in steps of 0.005 Jy beam^{-1}. 850 μm polarization vectors are sampled on a 10″ grid. Vectors are plotted where $I > 0$, $p/dp > 2$, and $dp < 4\%$.

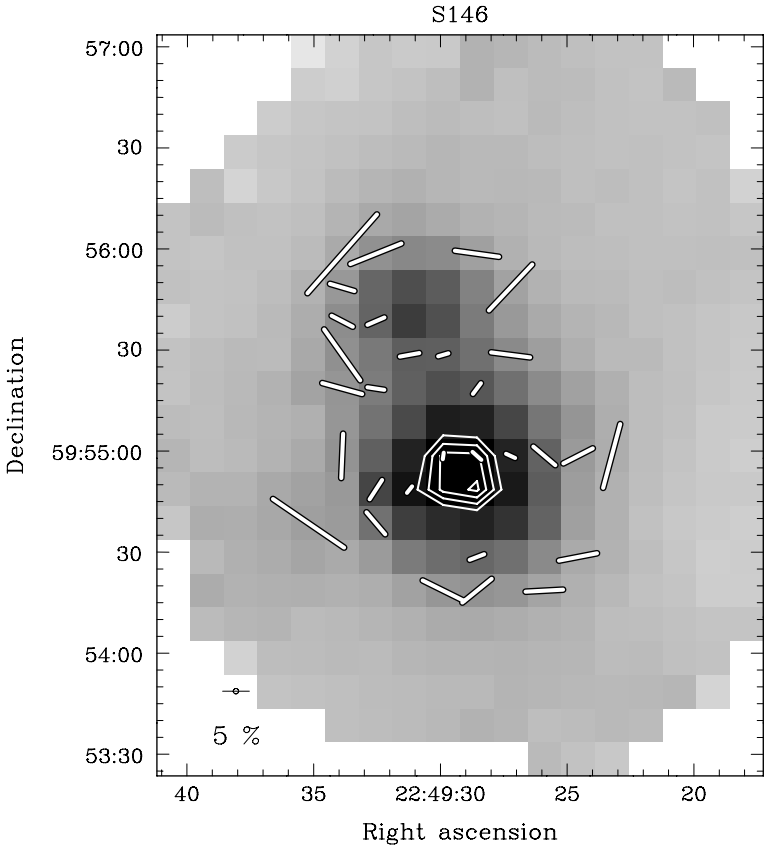

Figure 77. Compiled data toward the SFR S146. Contours range from 0.004 Jy beam^{-1} in steps of 0.00025 Jy beam^{-1}. 850 μm polarization vectors are sampled on a 10″ grid. Vectors are plotted where $I > 0$, $p/dp > 2$, and $dp < 4\%$.

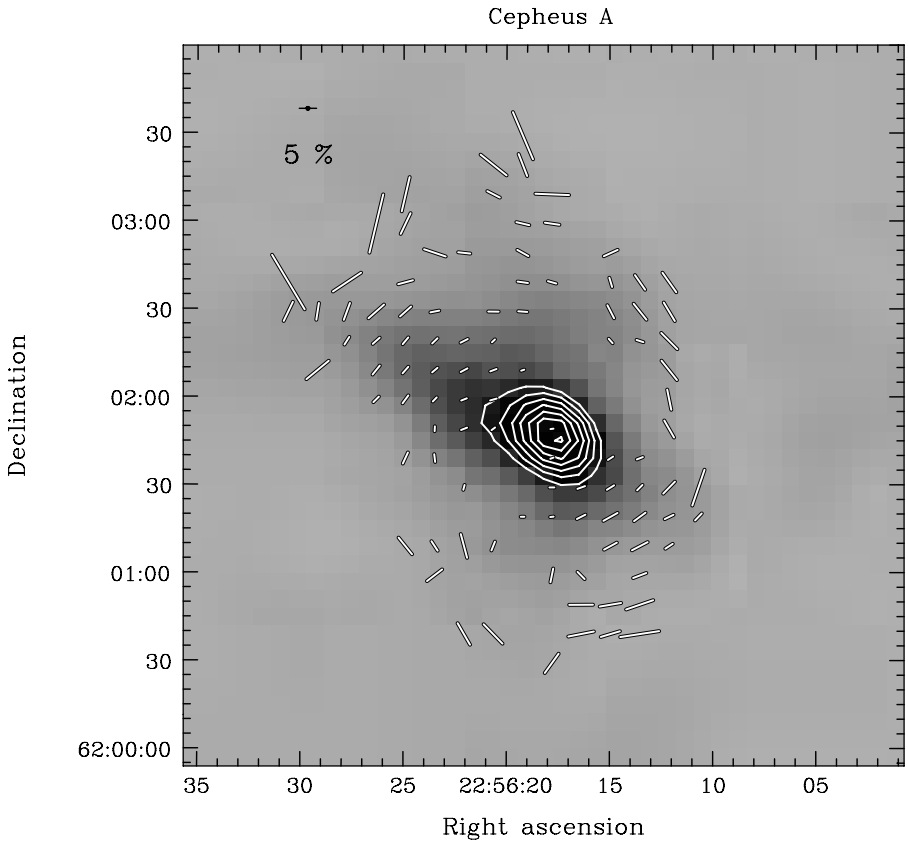

Figure 78. Compiled data toward the Class 0 source Cep A. Contours range from 5 Jy beam^{-1} in steps of 1 Jy beam^{-1}. 850 μm polarization vectors are sampled on a 10″ grid. Vectors are plotted where $I > 0$, $p/dp > 2$, and $dp < 4\%$.

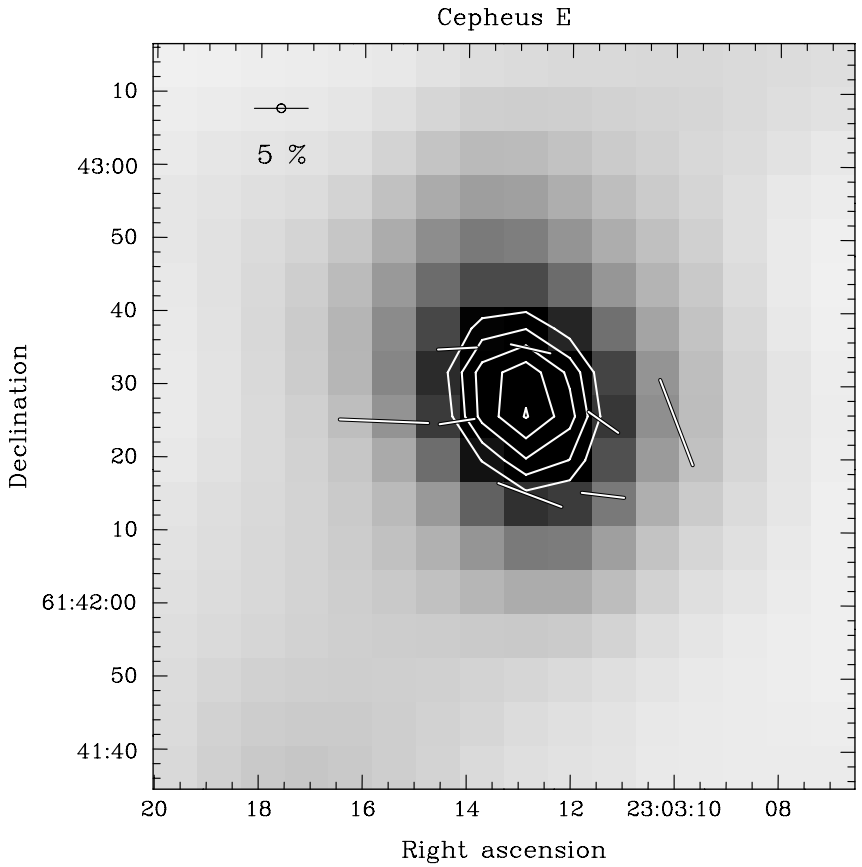

Figure 79. Compiled data toward the Class 0 source Cep E. Contours range from 0.6 Jy beam^{-1} in steps of 0.1 Jy beam^{-1}. 850 μm polarization vectors are sampled on a 10″ grid. Vectors are plotted where $I > 0$, $p/dp > 2$, and $dp < 4\%$.

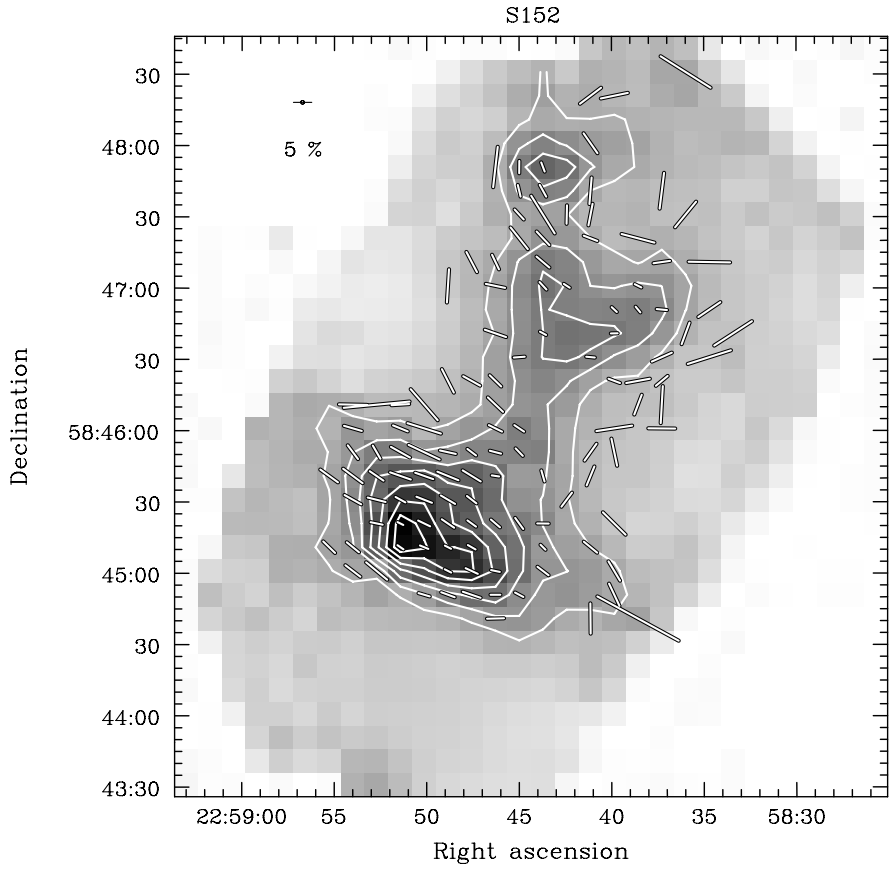

Figure 80. Compiled data toward the SFR S152. The intensity data are taken from SCUPOL data, rather than the SCUBA Legacy Catalog. Contours range from 0.91 Jy beam^{-1} in steps of 0.45 Jy beam^{-1} where we have used a flux conversion factor of 455 Jy beam^{-1} V^{-1}. 850 μm polarization vectors are sampled on a 10″ grid. Vectors are plotted where $I > 0$, $p/dp > 2$, and $dp < 4\%$.

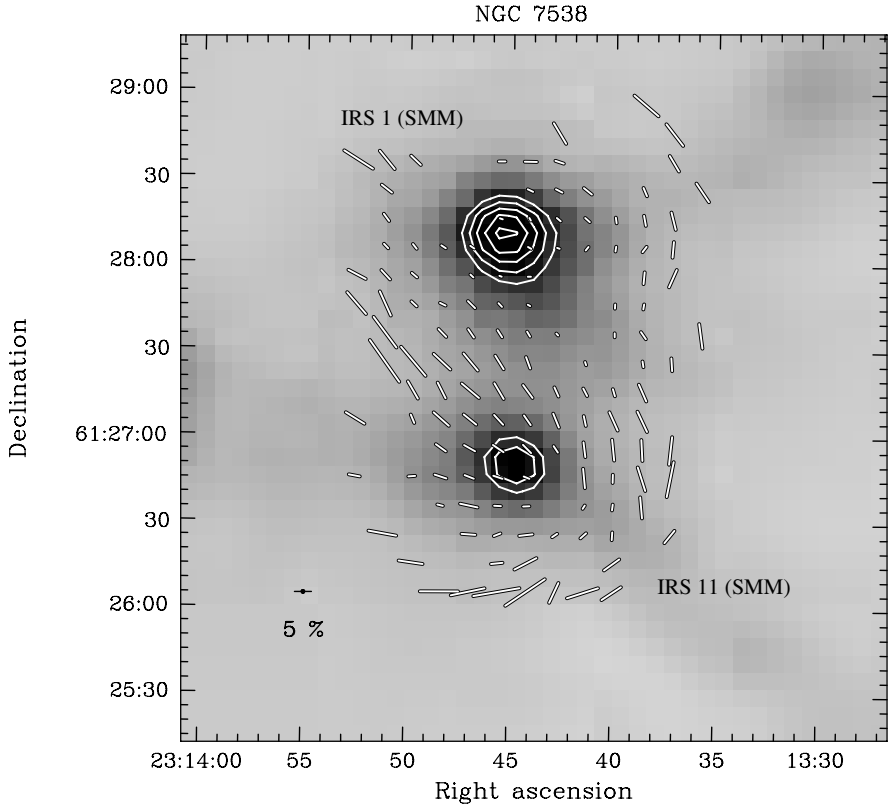

Figure 81. Compiled data toward the high-mass SFR NGC 7538. Contours range from 5 Jy beam^{-1} in steps of 1 Jy beam^{-1}. 850 μm polarization vectors are sampled on a 10″ grid. Vectors are plotted where $I > 0$, $p/dp > 2$, and $dp < 4\%$.

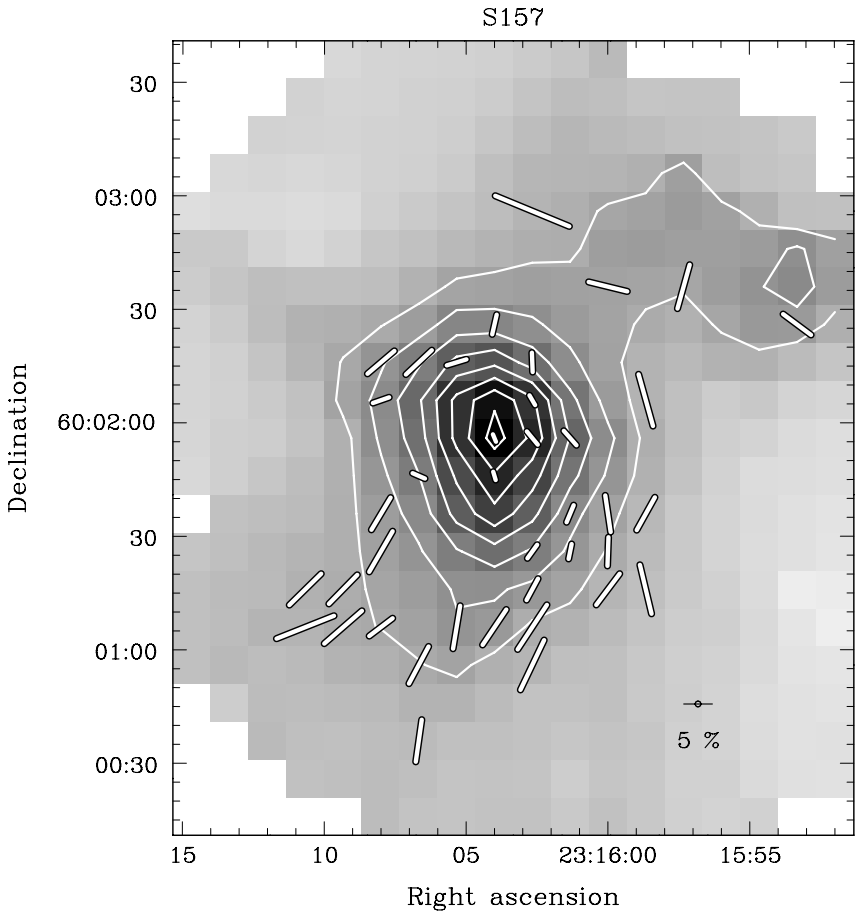

Figure 82. Compiled data toward the SFR S157. The intensity data are taken from SCUPOL data, rather than the SCUBA Legacy Catalog. Contours range from 0.91 Jy beam^{-1} in steps of 0.45 Jy beam^{-1} where we have used a flux conversion factor of 455 Jy beam^{-1} V^{-1}. 850 μm polarization vectors are sampled on a 10″ grid. Vectors are plotted where $I > 0$, $p/dp > 2$, and $dp < 4\%$.

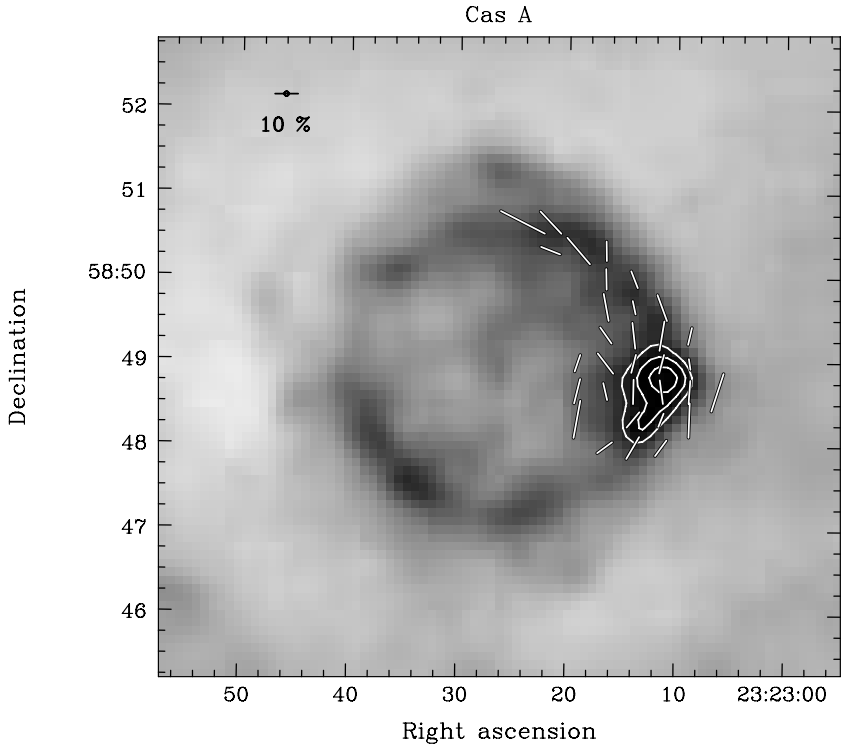

Figure 83. Compiled data toward the SNR Cas A. Contours range from 0.2 Jy beam^{-1} in steps of 0.05 Jy beam^{-1}. 850 μm polarization vectors are sampled on a 20″ grid (binned from a 10″ grid). Vectors are plotted where $I > 0$, $p/dp > 2$, and $dp < 4\%$.

Table 5
Results Summary

Source/ Region	Object Type	Figure Number	Distance (kpc)	Distance Reference	First Publication?	Previous SCUPOL Publication(s)	Other Polarized Dust Emission Publication(s)
CB 3	BG	2	2.5	Launhardt & Henning (1997)	Y	Vallée et al. (2000) (single point)	
L1287	SC/PC	3	0.850	Yang et al. (1991)	N	Curran & Chrysostomou (2007)	
W3 Main	SFR	4	1.95	Xu et al. (2006)	N	Greaves et al. (2003)	Dotson et al. (2000); Schleuning et al. (2000); Schleuning et al. (2000); Greaves et al. (1999)
W3 North	SFR	5	1.95	Xu et al. (2006)	Y		
W3 OH	SFR	6	1.95	Xu et al. (2006)	Y		Glenn et al. (1999)
AFGL 333	SFR	7	1.95	Xu et al. (2006)	Y		
GL 437	SFR	8	~2	Arquilla & Goldsmith (1984)	N	Curran & Chrysostomou (2007)	
L1448	YSO	9	0.250 ± 0.050	Enoch et al. (2006)	Y		Kwon et al. (2006)
L1455	SFR	10	0.250 ± 0.050	Enoch et al. (2006)	Y		
NGC 1333	SFR	11	0.320	de Zeeuw et al. (1999)	Y	Chrysostomou et al. (2004); Curran et al. (2007) (IRAS 2 only)	Curran et al. (2007); Girart et al. (2006, 1999); Glenn et al. (1999)
IRAS 03282+3035	YSO	12	0.3	Motte & André (2001)	Y		
Barnard 1	SFR	13	0.250 ± 0.050	Enoch et al. (2006)	N	Matthews & Wilson (2002b)	Matthews et al. (2003, 2008)
HH211/IC348	SFR	14	0.250 ± 0.050	Enoch et al. (2006)	N	Chrysostomou et al. (2004); Curran et al. (2007)	
CB 17	BG	15	0.300	Launhardt & Henning (1997)	Y		
L1498	SC/PC		0.140 ± 0.020	Elias (1978); Ungerechts & Thaddeus (1987); Kenyon et al. (1994)	N	Kirk et al. (2006)	
L1551	YSO	17	0.140 ± 0.010	Kenyon et al. (1994)	Y		Glenn et al. (1999)
L1527	YSO	18	0.140 ± 0.010	Kenyon et al. (1994)	Y		
IRAM 04191+1522	YSO	19	0.140 ± 0.010	Kenyon et al. (1994)	Y		
L1517B	SC/PC	20	0.140 ± 0.020	Elias (1978); Ungerechts & Thaddeus (1987); Kenyon et al. (1994)	N	Kirk et al. (2006)	
CB 26	BG	21	0.140	Launhardt & Sargent (2001)	N	Henning et al. (2001); Wolf et al. (2004)	
L1544	SC/PC	22	0.140 ± 0.010	Kenyon et al. (1994)	N	Ward-Thompson et al. (2000);	Crutcher et al. (2004); Nutter et al. (2004); Crutcher (2004)
RNO 43	YSO	23	0.4	Zinnecker et al. (1992)	Y		
Crab Nebula	SNR	24	2.0	Trimble (1973)	Y	Greaves et al. (2003) (raster map mode only)	

Table 5
(Continued)

Source/ Region	Object Type	Figure Number	Distance (kpc)	Distance Reference	First Publication?	Previous SCUPOL Publication(s)	Other Polarized Dust Emission Publication(s)
OMC-1	SFR	25	0.414 ± 0.007	Menten et al. (2007)	N	Coppin et al. (2000); Vallée & Fiege (2007a)	Vaillancourt et al. (2008); Vallée & Fiege (2007a); Houde et al. (2004); Vaillancourt (2002); Dotson et al. (2000); Schleuning (1998); Glenn et al. (1999); Rao et al. (1998); Dragovan (1986); Hildebrand et al. (1984)
OMC-2 & OMC-3	SFR	26	0.414 ± 0.007	Menten et al. (2007)	Y	Matthews & Wilson (2000); Matthews et al. (2001a) (OMC-3 only)	Houde et al. (2004); Matthews et al. (2005)
VLA1 IRS2	YSO	27	0.414 ± 0.007	Menten et al. (2007)	Y		
NGC 2024	SFR	28	0.400	Anthony-Twarog (1982)	N	Matthews et al. (2002, 2003)	Dotson et al. (2000); Lai et al. (2002)
LBS 23	SFR	29	0.400	Anthony-Twarog (1982)	Y	Matthews et al. (2002) (LBS 23S only)	
NGC 2068	SFR	30	0.400	Anthony-Twarog (1982)	N	Matthews & Wilson (2002a)	
CB 34	BG	31	1.5	Launhardt & Henning (1997)	Y	Vallée et al. (2000) (nondetection)	
NGC 2071 IR	SFR	32	0.400	Anthony-Twarog (1982)	N	Matthews et al. (2002)	Cortes et al. (2006); Dotson et al. (2009)
HH 111	YSO	33	0.400	Anthony-Twarog (1982)	Y		
IRAS 05490+2658	SFR	34	2.1	Snell et al. (1990)	Y		
Mon R2 IRS	SFR	35	0.950	Racine & van de Bergh (1970)	N	Curran & Chrysostomou (2007); Curran et al. (2007)	Glenn et al. (1999); Greaves et al. (1999)
IRAS 06381+1039	SFR	36	0.800	Walker (1956)	Y	Dotson et al. (2009)	
MON IRAS 12	SFR	37	0.800	Walker (1956)	Y		Dotson et al. (2009)
CB 54	BG	38	1.1	Brand & Blitz (1993)	N	Wolf et al. (2004); Henning et al. (2001); Vallée et al. (2000)	
IRAS 08076-3556	SFR	39	0.2	Knude et al. (1999) - 0.45 Brandt et al. (1971)	Y		
IRC +10216	AGB	40	0.11 - 0.15	Groenewegen et al. (1998)	Y		Vallée & Bastien (2000)
M82	GAL	41	3250	Tammann & Sandage (1968)	N	Greaves et al. (2000b, 2000a);	Greaves & Holland (2002)
M87	GAL	42	21100	Gavazzi et al. (1999)	Y		

Table 5
(Continued)

Source/ Region	Object Type	Figure Number	Distance (kpc)	Distance Reference	First Publication?	Previous SCUPOL Publication(s)	Other Polarized Dust Emission Publication(s)
L183	SC/PC	43	0.15	Ward-Thompson et al. (1999)	N	Ward-Thompson et al. (2000); Crutcher et al. (2004)	
ρ Oph A	SFR	44	0.139	Mamajek (2008)	N	Tamura (1999); Green et al. (2004)	Holland et al. (1996); Greaves et al. (1994)
ρ Oph C	SFR	45	0.139	Mamajek (2008)	Y		
ρ Oph B2	SFR	46	0.139	Mamajek (2008)	Y	Matthews et al. (2001b) (partial data set)	
IRAS 16293-2422	YSO	47	0.12	de Geus et al. (1989); Knude & Hog (1998)	Y		
L43	SC/PC	48	0.17	Ward-Thompson et al. (1999)	N	Ward-Thompson et al. (2000); Crutcher et al. (2004)	
CB 68	BG	49	0.160	Launhardt & Henning (1997)	N	Vallée et al. (2000, 2003); Vallée & Fiege (2007b)	
NGC 6302	PN	50	1.17	Meaburn et al. (2008)	Y	Sabin et al. (2007a, 2007b) (450 μm only)	
NGC 6334A	SFR	51	1.7	Neckel (1978)	N	Curran & Chrysostomou (2007); Curran et al. (2007)	
Galactic Center	GC	52	8	Genzel et al. (2000)	N	Aitken et al. (2000); Greaves & Holland (2002)	Chuss et al. (2003); Dotson et al. (2000); Bower et al. (2001, 2003)
G011.11-0.12	SFR	53	3.6	Carey et al. (2000)	Y		
GGD 27	SFR	54	1.7	Rodriguez et al. (1980)	Y	Curran & Chrysostomou (2007) (partial data set)	
CRL 2136 IRS 1	SFR	55	~2	Kastner et al. (1992)	Y		
Serpens Main Core	SFR	56	0.310	de Lara et al. (1991)	N	Davis et al. (2000)	
CL 04/CL 21	SFR	57	0.770	Webster & Ryle (1976)	Y		
G28.34+0.06	SFR	58	~4.8	Carey et al. (2000)	Y		
IRAS 18437-0216	SFR	59	6.6	Sridharan et al. (2005)	Y		
W48	SFR	60	3.4	Vallée & MacLeod (1990)	N	Curran et al. (2004, 2005)	
R Cr A	SFR	61	0.130	Marraco & Rydgren (1981)	N	Curran & Chrysostomou (2007)	Clark et al. (2000)
W49	SFR	62	11.4	Gwinn et al. (1992)	N	Curran & Chrysostomou (2007)	
W51	SFR	63	7.5	Genzel et al. (1981)	N	Chrysostomou et al. (2002, 2004)	Lai et al. (2001); Dotson et al. (2000)
B335	BG	64	~0.250	Tomita et al. (1979); Frerking et al. (1987)	N	Wolf et al. (2004, 2003a, 2003b)	

Table 5
(Continued)

Source/ Region	Object Type	Figure Number	Distance (kpc)	Distance Reference	First Publication?	Previous SCUPOL Publication(s)	Other Polarized Dust Emission Publication(s)
IRAS 20081+2720	SFR	65	0.700	Wilking et al. (1989)	Y		
IRAS 20126+4104	SFR	66	1.7	Wilking et al. (1989)	N	Curran & Chrysostomou (2007)	
AFGL 2591 IRS	SFR	67	1.5	Wendker & Baars (1974)	N	Curran & Chrysostomou (2007)	Vallée & Bastien (2000); Glenn et al. (1999)
IRAS 20188+3928	SFR	68	0.4 – 4	Little et al. (1988)	N	Curran & Chrysostomou (2007)	
S106	SFR	69	0.600	Staude et al. (1982)	N	Vallée & Fiege (2005)	Dotson et al. (2000)
G079.3+0.3	SFR	70	1	Carey et al. (2000)	Y		
DR 21	SFR	71	3	Campbell et al. (1982)	Y	Vallée & Fiege (2006); Curran & Chrysostomou (2007) (DR 21 OH only)	Dotson et al. (2000); Lai et al. (2003); Glenn et al. (1999); Greaves et al. (1999)
G81.56+0.10	SFR	72	1.7	Schneider et al. (2006)	Y		
CRL 2688	AGB	73	1	Ney et al. (1975)	N	Greaves (2002); Sabin et al. (2007a, 2007b)	
NGC 7027	PN	74	1	Zijlstra et al. (2008)	N	Greaves (2002); Sabin et al. (2007b)	
CB 230	BG	75	0.400 ± 0.100	Launhardt & Henning (1997); Kun (1998)	N	Wolf et al. (2004, 2003a, 2003b)	
S140	SFR	76	0.900	Preibisch & Smith (2002)	N	Chrysostomou et al. (2003); Curran & Chrysostomou (2007)	Glenn et al. (1999)
S146	SFR	77	5.2	Wu et al. (2005)	N	Curran & Chrysostomou (2007)	
Cepheus A	YSO	78	0.730	Blaauw, Hiltner & Johnson (1959)	N	Chrysostomou et al. (2003); Curran & Chrysostomou (2007); Curran et al. (2007)	Glenn et al. (1999)
Cepheus E	YSO	79	0.730	Blaauw, Hiltner & Johnson (1959)	N		
S152	SFR	80	5	Wouterloot et al. (1993)	N	Curran et al. (2004, 2005)	
NGC 7538	SFR	81	2.8	Blitz et al. (1982)	N	Momose et al. (2001)	Dotson et al. (2000)
S157	SFR	82	2.5	Shirley et al. (2003)	N	Curran & Chrysostomou (2007)	
Cas A	SNR	83	3.4	Reed et al. (1995)	N	Dunne et al. (2009)	
CB 244	BG	84	$\sim$0.180	Kun (1998)	N	Wolf et al. (2004, 2003a, 2003b)	

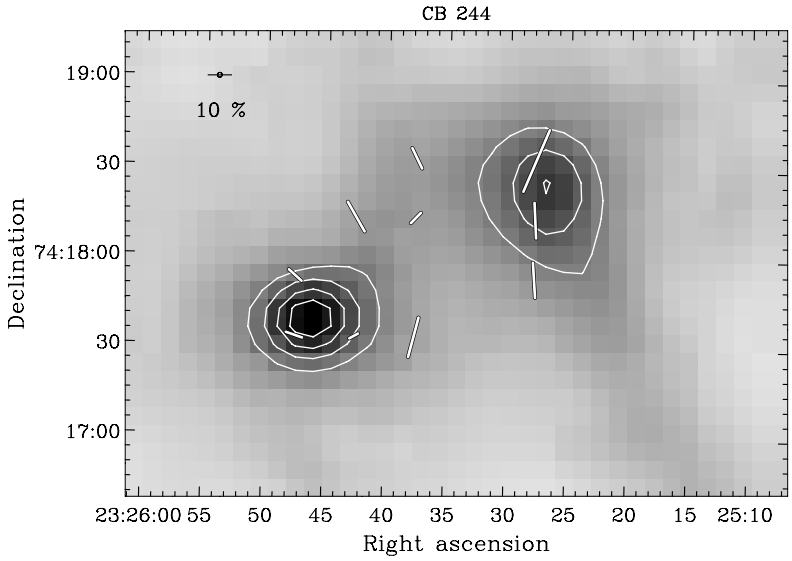

Figure 84. Compiled data toward the source CB 244. Contours range from 0.1 Jy beam^{-1} in steps of 0.05 Jy beam^{-1}. 850 μm polarization vectors are sampled on a 20″ grid (binned from a 10″ grid). Vectors are plotted where $I > 0$, $p/dp > 2$, and $dp < 4\%$.

In total, 104 regions and objects were observed in the jiggle-mapping mode with SCUPOL. For many of the regions, some or all of the data presented here have already been published; however, for 39 regions (indicated in Table 5), this is the first publication of some or all of the SCUPOL data.

Polarization vectors were plotted when $p/dp > 2, dp < 4\%$ and values of total intensity $I > 0$, although more stringent selection has been used in few regions where the density of vectors is high. We have also binned the data by a factor of 2 in some regions where vector density was very high, or S/N improvement was significant. The figures are intended to be used to allow assessment of the data quality rather than for detailed modeling or as a basis for scientific conclusions, tasks for which more stringent selection criteria might be adopted. Table 6 contains the positions, intensities, polarization percentages, and position angles (with uncertainties) for all of the vectors plotted in the figures. The coordinates are given in arcsecond offsets from the reference coordinate for the field given in Table 1 and in absolute R.A. and decl. (J2000) coordinates. Should a different degree of binning be required, the Stokes IQU fits cubes are required to generate the vectors after binning is done using Equations (1)–(5). The authors are amenable to generating such data sets in collaboration with interested researchers. The data cubes and tabulated data for all observed fields with good data have been incorporated into the CADC archive in tabular form and quick-look figures. We describe how to access these data in Section 4.

In most cases, we have plotted vectors indicating measured polarization (i.e., the "E-vector") over larger, calibrated SCUBA maps of Di Francesco et al. (2008). The polarization percentage is indicated by vector length, while the orientation gives the polarization position angle. In several cases, no SCUBA map exists, while in a few others, the extent of the SCUBA maps is less than the polarization maps. In these cases, we have overlaid the polarization vectors on the Stokes I maps from the polarization data themselves. We have adopted fiducial flux conversion factors for the conversion of Stokes I from volts to Jy beam^{-1} for the purposes of the figures. The values adopted are taken from Jenness et al. (2002) and are specified in each individual case. The adoption of a flux conversion factor to calibrate the SCUPOL intensity maps was only required in eight cases. We have not presented flux calibrated intensities in Table 6. Since flux calibration varies with epoch, and we do not have polarization planetary calibration data for each night of SCUPOL observations, we have opted not to flux calibrate the individual data sets. Instead, we have combined the raw voltage data. While this can introduce some systematic error, likely no more than 20%, each application of a flux conversion factor per night would carry a comparable uncertainty which could cumulatively exceed the uncertainty of not flux calibrating at all. Our expectation is that, since polarization vectors are based on ratios of fluxes, these uncertainties will have minimal effect on the final ratios.

The planetary maps are presented in Figures 85–88. The data are also tabulated in Table 7.

4. HOW TO USE THESE DATA

The figures and tables included in this paper may not meet the needs of all researchers in their present form. In some cases, more binning may be desirable to increase the signal to noise, or more stringent selection criteria will need to be applied. We caution readers from scientific interpretation of the data presented without keeping these two important points in mind.

In some cases, significant polarization results have been published in the literature toward regions listed as nondetections or having "no good data" in Table 1. In most cases, this is due to our exclusion of photometry data from this study. Examples include DG Tau and GM Aur for which detections from photometric polarimetry do appear in the literature (Tamura et al. 1999). In other cases, data were omitted which were included in published papers due to an absence of a tau solution, i.e., Barnard 1 (Matthews & Wilson 2002b). Where data are omitted because they are "nonstandard," we suggest interested researchers contact the authors of published SCUPOL papers where they exist.

To make effective use of the data products presented here, we have archived the Stokes I, Q, and U data cubes at a site hosted by the CADC[8] from which the data cubes themselves can be downloaded in FITS or NDF formats.

[8] http://www.cadc-ccda.hia-iha.nrc-cnrc.gc.ca/community/scupollegacy/.

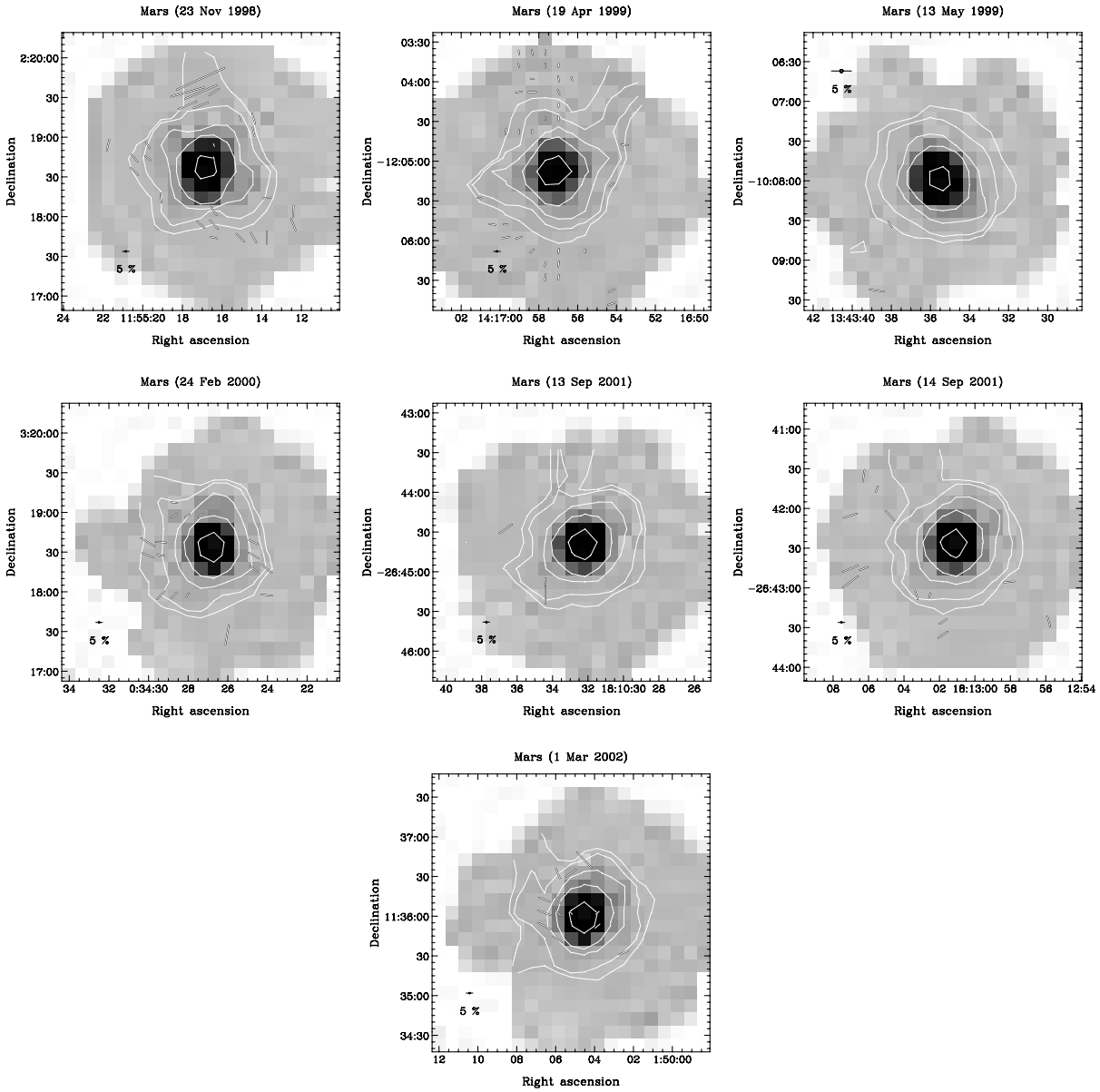

Figure 85. Reduced calibration observations of the planet Mars taken with SCUPOL. Contours are plotted at 70, 80, 90, 95, and 99th percentiles of the peak. 850 μm polarization vectors are sampled on a 10″ grid. Vectors are plotted where $I > 0$, $p/dp > 2$, and $dp < 4\%$.

Table 6
SCUPOL Polarization Data Table

Object/ Region	R.A.[a] Offset	Decl.[a] Offset	R.A. (J2000)	Decl. (J2000)	I (Volts)	dI (Volts)	p (%)	dp (%)	θ (°)	$d\theta$ (°)
CB3	5.0	−15.0	00:28:42.10	+56:41:49.9	2.612e-03	2.407e-05	4.2	1.0	−16.3	8.3
CB3	−5.0	−5.0	00:28:40.89	+56:41:59.9	2.356e-03	4.387e-05	6.5	2.5	−32.8	7.6
CB3	15.0	5.0	00:28:43.31	+56:42:09.9	1.502e-03	2.325e-05	4.4	1.8	21.6	10.9
CB3	15.0	15.0	00:28:43.31	+56:42:19.9	1.107e-03	1.830e-05	8.2	2.8	14.7	7.8
L1287	35.0	5.0	00:36:51.48	+63:29:02.1	2.719e-03	4.896e-05	5.3	2.6	−50.0	11.2
L1287	25.0	5.0	00:36:49.99	+63:29:02.1	4.976e-03	4.588e-05	5.2	1.2	−51.6	7.7
L1287	−25.0	5.0	00:36:42.52	+63:29:02.1	2.810e-03	6.317e-05	8.0	2.9	−35.1	9.0
L1287	35.0	25.0	00:36:51.48	+63:29:22.1	2.589e-03	5.651e-05	5.9	2.9	−60.4	12.8
L1287	45.0	35.0	00:36:52.97	+63:29:32.1	1.703e-03	3.946e-05	15.2	3.9	−45.5	6.7
L1287	25.0	35.0	00:36:49.99	+63:29:32.1	2.385e-03	4.908e-05	8.5	3.6	−62.7	12.1

Notes.
[a] Arcsecond offsets from reference coordinates given in Table 1.
[b] Beam (after smoothing and regridding) sampling, 20″.
[c] Nonstandard selection criteria used. See figure caption.
(This table is available in its entirety in a machine-readable form in the online journal. A portion is shown here for guidance regarding its form and content.)

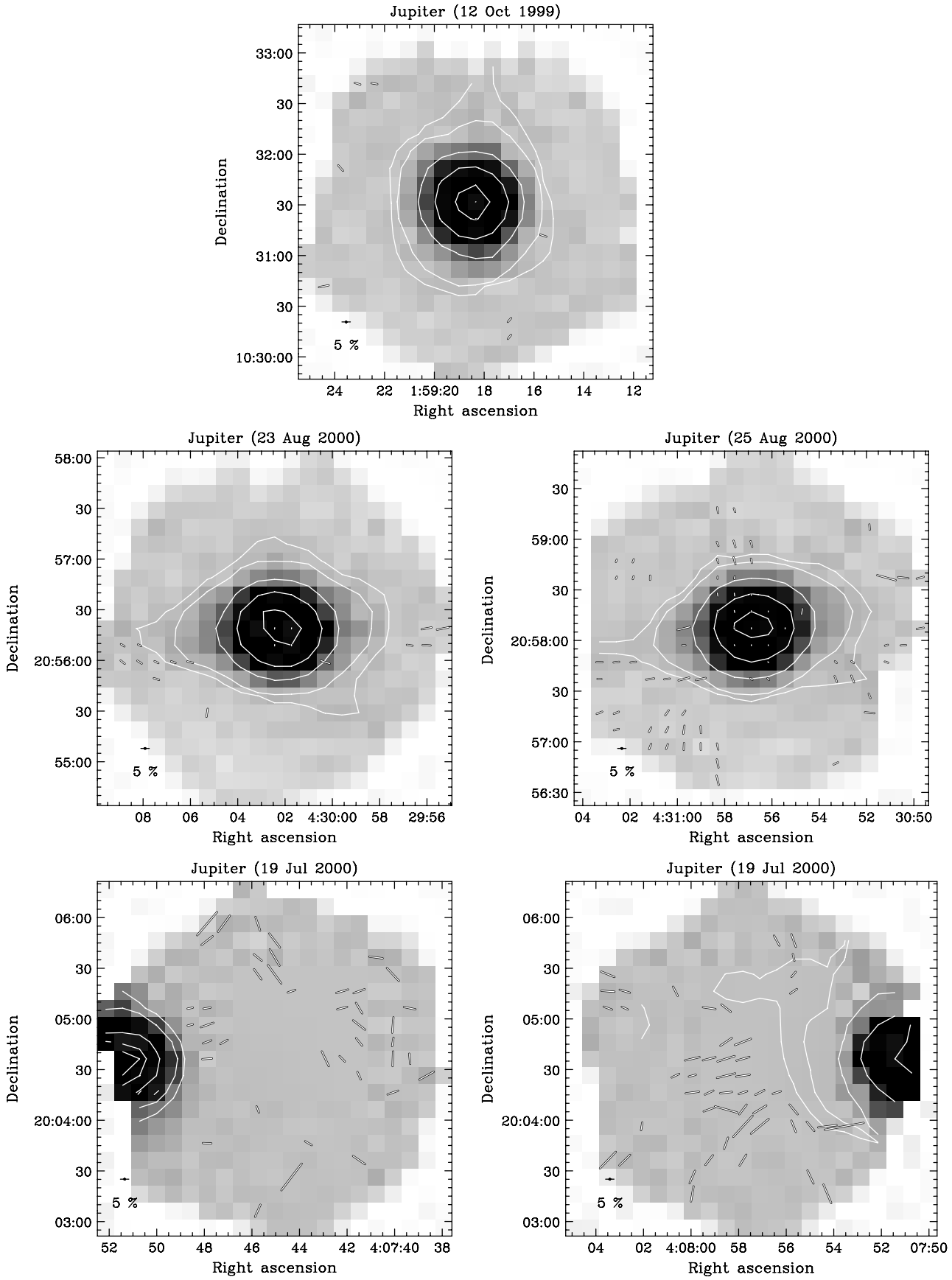

Figure 86. Reduced calibration observations of the planet Jupiter taken with SCUPOL. Contours are plotted at 70, 80, 90, 95, and 99th percentiles of the peak. 850 μm polarization vectors are sampled on a 10″ grid. Vectors are plotted where $I > 0$, $p/dp > 2$, and $dp < 4\%$.

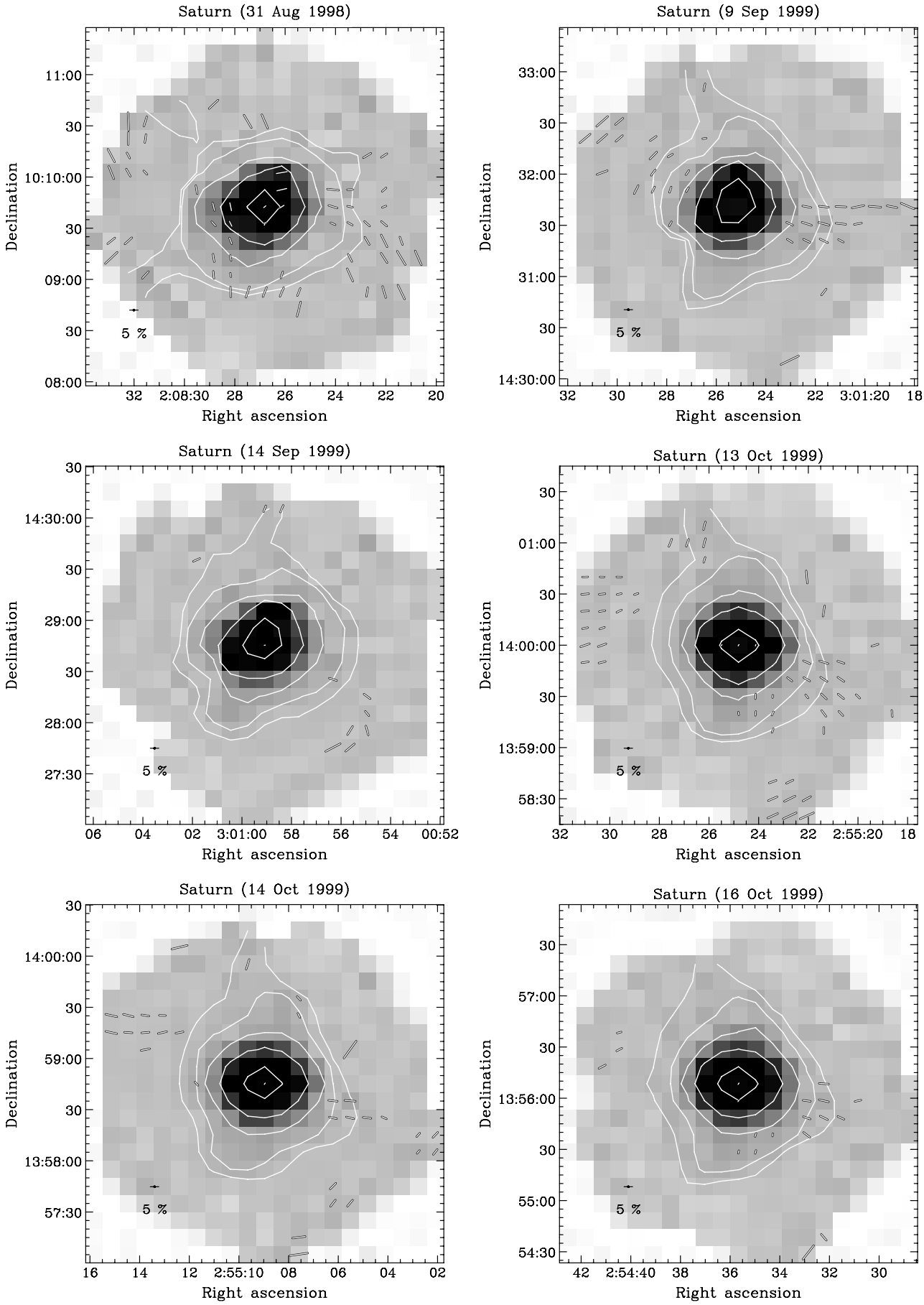

Figure 87. Reduced calibration observations of the planet Saturn taken with SCUPOL. Contours are plotted at 70, 80, 90, 95, and 99th percentiles of the peak. 850 μm polarization vectors are sampled on a 10″ grid. Vectors are plotted where $I > 0$, $p/dp > 2$, and $dp < 4\%$.

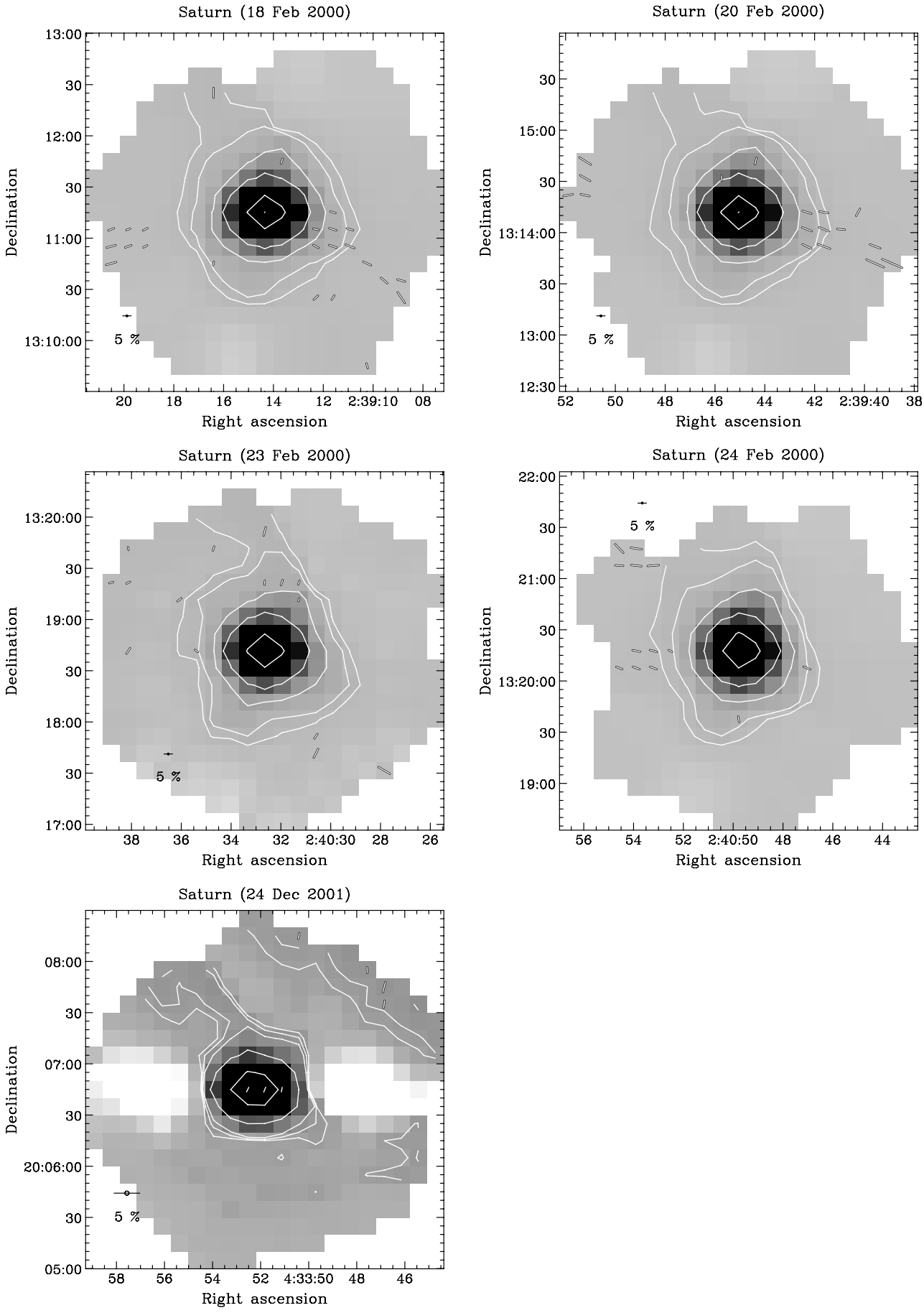

Figure 87. (Continued)

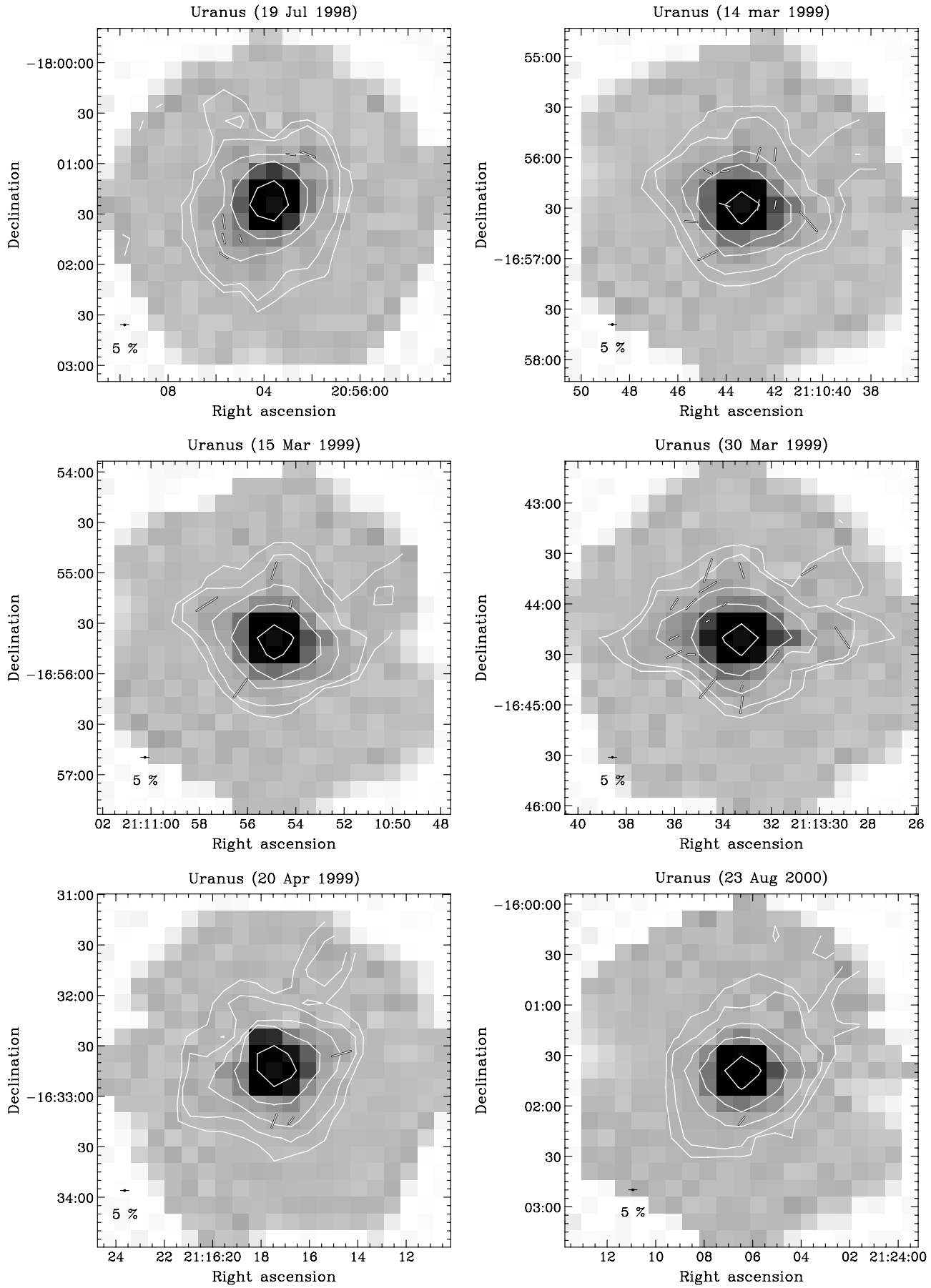

Figure 88. Reduced calibration observations of the planet Uranus taken with SCUPOL. Contours are plotted at 70, 80, 90, 95, and 99th percentiles of the peak. 850 μm polarization vectors are sampled on a 10″ grid. Vectors are plotted where $I > 0$, $p/dp > 2$, and $dp < 4\%$.

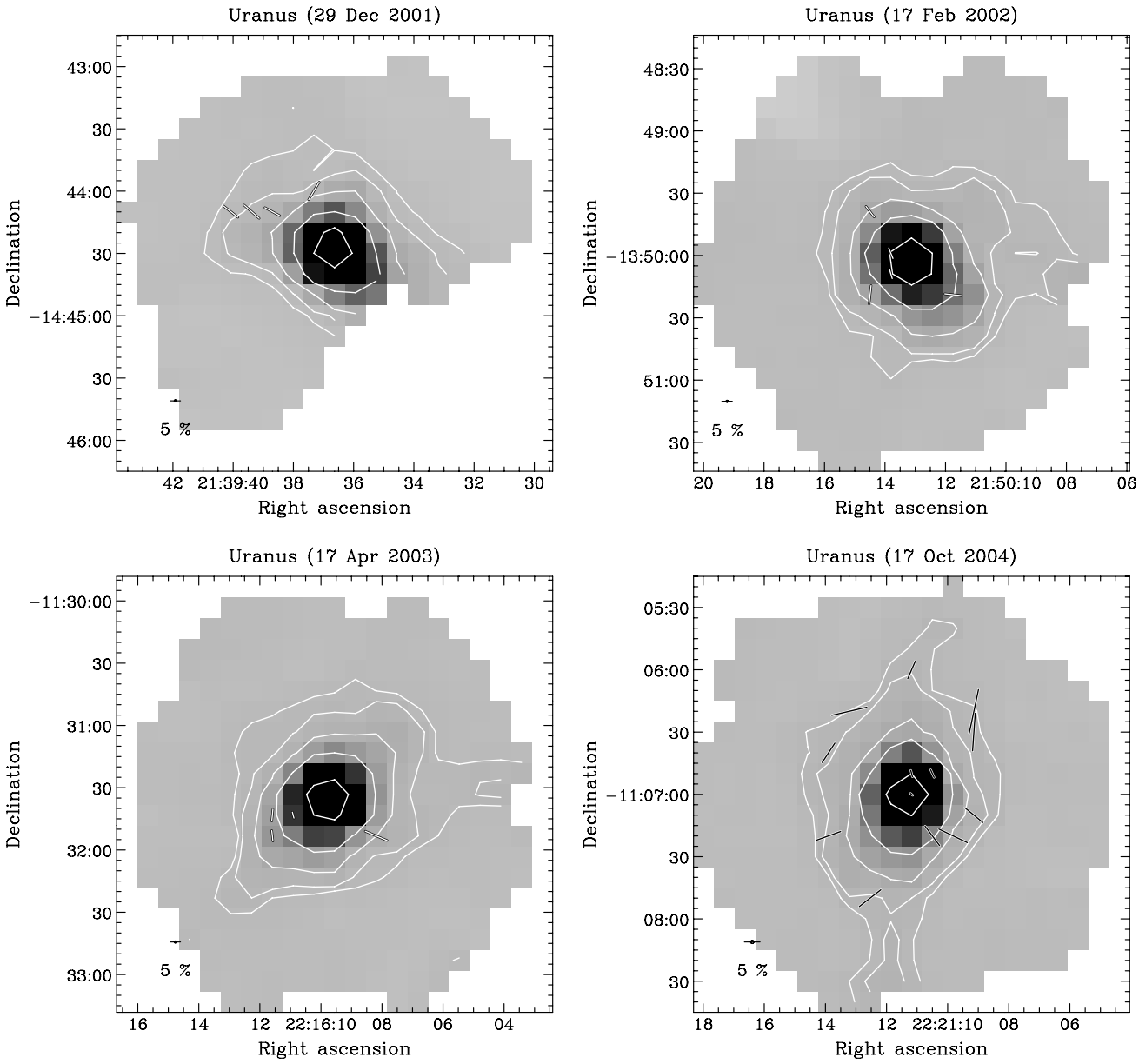

Figure 88. (Continued)

Table 7
SCUPOL Planetary Polarization Data Table

Object/ Region	Observing Date	R.A.[a] Offset	Decl.[a] Offset	I (Volts)	dI (Volts)	p (%)	dp (%)	θ (°)	$d\theta$ (°)
Mars	1998Nov23	−5.0	−55.0	2.829e-03	4.124e-05	4.8	2.0	77.6	11.1
Mars	1998Nov23	−25.0	−55.0	2.384e-03	4.074e-05	8.3	2.2	46.4	8.4
Mars	1998Nov23	−35.0	−55.0	2.071e-03	4.751e-05	8.4	2.9	30.0	11.3
Mars	1998Nov23	−45.0	−55.0	1.995e-03	6.102e-05	9.2	3.4	0.6	10.9
Mars	1998Nov23	5.0	−45.0	3.962e-03	5.349e-05	7.6	1.6	47.7	12.6
Mars	1998Nov23	−5.0	−45.0	3.679e-03	6.681e-05	8.9	2.0	42.6	6.6
Mars	1998Nov23	−65.0	−45.0	1.539e-03	4.176e-05	9.6	3.5	21.1	9.8
Mars	1998Nov23	−5.0	−35.0	4.910e-03	1.339e-04	7.2	2.7	34.0	11.6
Mars	1998Nov23	−65.0	−35.0	1.900e-03	3.875e-05	8.2	3.1	-3.4	8.8
Mars	1998Nov23	35.0	−25.0	5.425e-03	8.360e-05	7.0	2.1	6.7	7.2

Notes.
[a] Arcsecond offsets from planetary position.
(This table is available in its entirety in a machine-readable form in the online journal. A portion is shown here for guidance regarding its form and content.)

5. SUMMARY

The data assembled in this paper represent the bulk of the data taken with the SCUPOL instrument over its eight-year lifetime. The aim of this project has been to systematically reduce and compile all the jiggle map data for objects imaged with SCUPOL in order to provide a comprehensive data set to the community. The data summarized in Tables 1 and 3 is a complete accounting of all these *imaging data*. We note that data which were not used may in some cases be fine, but do not conform to the standard observing mode eventually adopted for the instrument and therefore require nonstandard reduction techniques not employed in our analysis (i.e., there is a difference between nonstandard and "bad" data). In most cases, data excluded for this reason were taken early in SCUPOL's lifetime, before the standard techniques were adopted. Specific details about why datafiles were excluded from the final maps can be obtained from the authors.

We have compiled, reduced and presented all SCUPOL imaging data to measure the polarized thermal emission from dust in the jiggle-mapping mode over the lifetime of the instrument. In all, 104 individual regions were mapped. Of these, 83 regions had useable data which yielded significant detections. Ten regions had useable data with no significant detections and 11 regions contained no useable (or only nonstandard) data.

The 83 regions with significant detections are primarily galactic star-forming regions or objects. The sample is comprised of 48 star-forming regions, 11 individual YSOs (or T Tauri stars), nine Bok globules, six starless or prestellar cores, two post-AGB stars, two planetary nebulae, two supernova remnants, two external galaxies and our own Galactic center. For 39 regions, this publication represents the first publication of the SCUPOL data, in whole or in part.

B.C.M. acknowledges the ongoing software support of T. Jenness and D. Berry at the Joint Astronomy Centre. The efforts of J. Greaves, A. Chrysostomou G. Schieven, J. Kirk, D. Ward-Thompson, R. Redman, P. Bastien, and F. Poidevin in consulting observing logs and data reduction records are appreciated.

C.A.M. and L.M.F. acknowledge support of the Herzberg Institute of Astrophysics co-operative program for undergraduates.

R.L.C. acknowledges funding from Science Foundation Ireland under grant number 04/BRG/P02741 and from the Marie Curie Fellowship Contract No. MTKD-CT-2005-029768 of the project "Young Stellar Objects, Their Surroundings and Jets: Advanced Observational and MHD Studies."

The JCMT is supported by the Science and Technology Facilities Council, the National Research Council Canada, and the Netherlands Organisation for Scientific Research.

This research used the facilities of the Canadian Astronomy Data Centre operated by the National Research Council of Canada with the support of the Canadian Space Agency.

REFERENCES

Aitken, D. K., Greaves, J., Chrysostomou, A., Jenness, T., Holland, W., Hough, J. H., Pierce-Price, D., & Richer, J. 2000, ApJ, 534, L173
Alves, J., Lada, C. J., & Lada, E. A. 1999, ApJ, 515, 265
Anthony-Twarog, B. J. 1982, AJ, 87, 1213
Archibald, E. N., et al. 2002, MNRAS, 336, 1
Arquilla, R., & Goldsmith, P. F. 1984, ApJ, 279, 664
Blaauw, A., Hiltner, W. A., & Johnson, H. L. 1959, ApJ, 130, 69
Blitz, L., Fich, M., & Stark, A. A. 1982, ApJS, 49, 183
Bower, G. C., Wright, M. C. H., Falcke, H., & Backer, D. C. 2001, ApJ, 555, 103
Bower, G. C., Wright, M. C. H., Falcke, H., & Backer, D. C. 2003, ApJ, 588, 331
Brand, J., & Blitz, L. 1993, A&A, 275, 67
Brandt, J. C., Stechter, T. P., Crawford, D. L., & Maran, S. P. 1971, ApJ, 163, L99
Campbell, M. F., Niles, D., Nawfel, R., Hawrylycz, M., Hoffmann, W. F., & Thronson, H. A., Jr. 1982, ApJ, 261, 550
Carey, S. J., Feldman, P. A., Redman, R. O., Egan, M. P., MacLeod, J. M., & Price, S. D. 2000, ApJ, 543, L157
Carlqvist, P., & Kristen, H. 1997, A&A, 324, 1115
Chrysostomou, A., Aitken, D. K., Jenness, T., Davis, C. J., Hough, J. H., Curran, R., & Tamura, M. 2002, A&A, 385, 1014
Chrysostomou, A., Curran, R., & Aitken, D. 2004, Ap&SS, 292, 509
Chrysostomou, A., Curran, R., Aitken, D., Jenness, T., & Davis, C. 2003, Ap&SS, 287, 161
Chuss, D. T., Davidson, J. A., Dotson, J. L., Dowell, C. D., Hildebrand, R. H., Novak, G., & Vaillancourt, J. E. 2003, ApJ, 599, 1116
Clark, S., et al. 2000, MNRAS, 319, 337
Coppin, K. E. K., Greaves, J. S., Jenness, T., & Holland, W. S. 2000, A&A, 356, 1031
Cortes, P. C., Crutcher, R. M., & Matthews, B. C. 2006, ApJ, 650, 246
Crutcher, R. M., Nutter, D. J., Ward-Thompson, D., & Kirk, J. M. 2004, ApJ, 600, 279
Crutcher, R. M. 2004, Ap&SS, 292, 225
Curran, R., Chrysostomou, A., Collett, J., Aitken, D., & Jenness, T. 2005, in ASP Conf. Ser. 343, Astronomical Polarimetry: Current Status and Future Directions, ed. A. Adamson et.al. (San Francisco, CA: ASP), 185
Curran, R. L., & Chrysostomou, A. 2007, MNRAS, 382, 699
Curran, R. L., Chrysostomou, A., Collett, J. L., Jenness, T., & Aitken, D. K. 2004, A&A, 421, 195
Curran, R. L., Chrysostomou, A., & Matthews, B. C. 2007, in in IAU Symp. 243, Submillimetre Polarimetric Observations of Magnetic Fields in Star-forming regions, ed. J. Bouvier & I. Appenzeller (Dordrecht: Kluwer), 63
Davis, C. J., Chrysostomou, A., Matthews, H. E., Jenness, T., & Ray, T. P. 2000, ApJ, 530, L115
Davis, C. J., Matthews, H. E., Ray, T. P., Dent, W. R. F., & Richer, J. S. 1999, MNRAS, 309, 141
de Geus, E. J., de Zeeuw, P. T., & Lub, J. 1989, A&A, 216, 44
de Lara, E., Chavarria-K., C., & Lopez-Molina, G. 1991, A&A, 243, 139
de Zeeuw, P. T., Hoogerwerf, R., de Bruijne, J. H. J., Brown, A. G. A., & Blaauw, A. 1999, AJ, 117, 354
Di Francesco, J., Johnstone, D., Kirk, H., MacKenzie, T., & Ledowsinska, E. 2008, ApJS, 175, 277
Dotson, J. L., Davidson, J., Dowell, C. D., Kirby, L., Hildebrand, R. H., & Vaillancourt, J. E. 2009, ApJS, submitted
Dotson, J. L., Davidson, J., Dowell, C. D., Schleuning, D. A., & Hildebrand, R. H. 2000, ApJS, 128, 335
Draine, B. T., & Weingartner, J. C. 1996, ApJ, 470, 551
Draine, B. T., & Weingartner, J. C. 1997, ApJ, 480, 633
Dragovan, M. 1986, ApJ, 308, 270
Dunne, L., et al. 2009, MNRAS, 394, 1307
Elias, J. H. 1978, ApJ, 224, 857
Enoch, M. L., et al. 2006, ApJ, 638, 293
Feldman, P. A., Redman, R. O., Carey, S. J., & Wyrowski, F. 2003, in SFChem 2002: Chemistry as a Diagnostic of Star Formation, ed. C. L. Curry & M. Fich (Ottawa: NRC Press), 292
Fiege, J. D., & Henricksen, R. N. 1996, MNRAS, 281, 1038
Fiege, J. D., & Pudritz, R. E. 2000a, MNRAS, 311, 85
Fiege, J. D., & Pudritz, R. E. 2000b, ApJ, 544, 830
Flett, A. M., & Murray, A. G. 1991, MNRAS, 249, 4P
Frerking, M. A., Langer, W. D., & Wilson, R. W. 1987, ApJ, 313, 320
Gavazzi, G., Boselli, A., Scodeggio, M., Pierini, D., & Belsole, E. 1999, MNRAS, 304, 595
Genzel, R., Pichon, C., Eckart, A., Gerhard, O. E., & Ott, T. 2000, MNRAS, 317, 348
Genzel, R., et al. 1981, ApJ, 247, 1039
Girart, J. M., Crutcher, R. M., & Rao, R. 1999, ApJ, 525, 109
Girart, J. M., Rao, R., & Marrone, D. P. 2006, Science, 313, 812
Glenn, J., Walker, C. K., & Young, E. T. 1999, ApJ, 511, 812
Greaves, J. S. 2002, A&A, 392, L1
Greaves, J. S., & Holland, W. S. 2002, in AIP Conf. Proc. 609, Astrophysical Polarized Backgrounds, ed. S. Cecchini et al. (New York: AIP), 267
Greaves, J. S., Holland, W. S., Jenness, T., & Hawarden, T. G. 2000a, Nature, 404, 732

Greaves, J. S., Jenness, T., Chrysostomou, A. C., Holland, W. S., & Berry, D. S. 2000b, in ASP Conf. Ser. 217, Imaging at Radio through Submillimeter Wavelengths, ed. J. G. Mangum & S. J. E. Radford (San Francisco, CA: ASP), 150
Greaves, J. S., Holland, W. S., Minchin, N. R., Murray, A. G., & Stevens, J. A. 1999, A&A, 344, 668
Greaves, J. S., Murray, A. G., & Holland, W. S. 1994, A&A, 284, L19
Greaves, J. S., et al. 2003, MNRAS, 340, 353
Green, D. A., Tuffs, R. J., & Popescu, C. C. 2004, MNRAS, 355, 1315
Groenewegen, M. A. T., van der Veen, W. E. C. J., & Matthews, H. E. 1998, A&A, 338, 491
Gwinn, C. R., Moran, J. M., & Reid, M. J. 1992, ApJ, 393, 149
Henning, T., Wolf, S., Launhardt, R., & Waters, R. 2001, ApJ, 561, 871
Hildebrand, R. H. 1988, QJRAS, 29, 327
Hildebrand, R. H., Dotson, J. L., Dowell, C. D., Novak, G., Schleuning, D. A., & Vaillancourt, J. 1998, Proc. SPIE, 3357, 289
Hildebrand, R. H., Dragovan, M., & Novak, G. 1984, ApJ, 284, L51
Holland, W. S., Greaves, J. S., Ward-Thompson, D., & André, P. 1996, A&A, 309, 267
Holland, W. S., et al. 1999, MNRAS, 303, 659
Houde, M., Dowell, D., Hildebrand, R. H., Dotson, J. L., Vaillancourt, J. E., Phillips, T. G., Ruisheng, P., & Bastien, P. 2004, ApJ, 604, 717
Jenness, T., Lightfoot, J. F., & Holland, W. S. 1998, Proc. SPIE, 3357, 548
Jenness, T., Lightfoot, J. F., Holland, W. S., Greaves, J. S., & Economou, F. 2000, in ASP Conf. Ser. 217, Imaging at Radio through Submillimeter Wavelengths, ed. J. G. Mangum & S. J. E. Radford (San Francisco, CA: ASP), 205
Jenness, T., Stevens, J. A., Archibald, E. N., Economou, F., Jessop, N. E., & Robson, E. I. 2002, MNRAS, 336, 14
Johnstone, D., & Bally, J. 1999, ApJ, 510, L49
Kastner, J. H., Weintraub, D. A., & Aspin, C. 1992, ApJ, 389, 357
Kenyon, S. J., Dobrzycka, D., & Hartmann, L. 1994, AJ, 108, 1872
Kirk, J. M., Ward-Thompson, D., & Crutcher, R. M. 2006, MNRAS, 369, 1445
Knude, J., & Hog, E. 1998, A&A, 338, 897
Knude, J., Jønch-Sørensen, H., & Neilsen, A. S. 1999, A&A, 350, 985
Kun, M. 1998, ApJS, 115, 59
Kwon, W., Looney, L. W., Crutcher, R. M., & Kirk, J. M. 2006, ApJ, 653, 1358
Lada, C., Alves, J., & Lada, E. 1999, ApJ, 512, 250
Lai, S.-P., Crutcher, R. M., Girart, J. M., & Rao, R. 2001, ApJ, 561, 864
Lai, S.-P., Crutcher, R. M., Girart, J. M., & Rao, R. 2002, ApJ, 566, 925
Lai, S.-P., Girtart, J. M., & Crutcher, R. M. 2003, ApJ, 598, 392
Launhardt, R., & Henning, T. 1997, A&A, 326, 329
Launhardt, R., & Sargent, A. I. 2001, ApJ, 562, L173
Lazarian, A. 2007, J. Quant. Spectrosc. Radiat. Transfer, 106, 225
Little, L. T., et al. 1988, A&A, 205, 129-134
Mamajek, E. E. 2008, Astron. Nachr., 329, 10
Marraco, H. G., & Rydgren, A. E. 1981, AJ, 86, 62
Matthews, B., Bergin, E., Crapsi, A., Hogerheijde, M., Jørgensen, J., Marrone, D., & Rao, R. 2008, Ap&SS, 313, 65
Matthews, B. C., & Wilson, C. D. 2000, ApJ, 531, 868
Matthews, B. C., & Wilson, C. D. 2002a, ApJ, 571, 356
Matthews, B. C., & Wilson, C. D. 2002b, ApJ, 574, 822
Matthews, B. C., Wilson, C. D., & Fiege, J. D. 2001a, ApJ, 562, 400
Matthews, B. C., Wilson, C. D., & Fiege, J. D. G. L., Pilbratt, et al. 2001b, in The Promise of the Herschel Space Observatory, (ESA-SP 460; Noordwijk: ESA Publications Division), 463
Matthews, B. C., Fiege, J. D., & Moriarty-Schieven, G. 2002, ApJ, 569, 304
Matthews, B. C., Crutcher, R. M., Lai, S.-P., & Wilson, C. D. 2003, in IAU Symp. 221, Is the Magnetic Field Preserved during Core Fragmentation? ed. M. Burton, R. Jayawardhana, & T. Bourke (Dordrecht: Kluwer), 199
Matthews, B. C., Chuss, D., Dotson, J., Dowell, D., Hildebrand, R., Johnstone, D., & Vaillancourt, J. 2003, SFChem 2002: Chemistry as a Diagnostic of Star Formation ed. C. L. Curry & M. Fich (Ottawa: NRC Press), 145
Matthews, B. C. 2005, in ASP Conf. Ser. 343, Astronomical Polarimetry: Current Status and Future Directions, ed. A. Adamson et al. (San Francisco, CA: ASP), 99
Matthews, B. C., Lai, S.-P., Crutcher, R. M., & Wilson, C. D. 2005, ApJ, 626, 959
McKee, C. F., & Ostriker, E. C. 2007, ARA&A, 45, 565
Meaburn, J., Lloyd, M., Vaytet, N. M. H., & López, J. A. 2008, MNRAS, 385, 269
Menten, K. M., Reid, M. J., Forbrich, J., & Brunthaler, A. 2007, A&A, 474, 515
Mitchell, G. F., Johnstone, D., Moriarty-Schieven, G., Fich, M., & Tothill, N. F. H. 2001, ApJ, 556, 215
Momose, M., Tamura, M., Kameya, O., Greaves, J. S., Chrysostomou, A., Hough, J. H., & Morino, J. I. 2001, ApJ, 555, 855
Motte, F., & André, P. 2001, A&A, 365, 440
Nakamura, F., Hanawa, T., & Nakano, T. 1993, PASJ, 45, 551
Neckel, T. 1978, A&A, 69, 51
Ney, E. P., Merrill, K. M., Becklin, E. E., Neugebauer, G., & Wynn-Williams, C. G. 1975, ApJ, 198, L129
Nutter, D. J., Ward-Thompson, D., Crutcher, R. M., & Kirk, J. M. 2004, Ap&SS, 292, 179
Pravdo, S. H., Rodriguez, L. F., Curiel, S., Canto, J., Torrelles, J. M., Becker, R. H., & Sellgren, K. 1985, ApJ, 293, L35
Preibisch, T., & Smith, M. D. 2002, A&A, 383, 540
Pudritz, R. E. 1985, ApJ, 293, 216
Racine, R., & van de Bergh, S. 1970, in IAU Symp. 38, The Spiral Structure of Our Galaxy, ed. W. Becker & G. Contopoulos (Dordrecht: Reidel), 219
Rao, R., Crutcher, R. M., Plambeck, R. L., & Wright, M. C. H. 1998, ApJ, 502, L75
Reed, J. E., Hester, J. J., Fabian, A. C., & Winkler, P. F. 1995, ApJ, 440, 706
Rodriguez, L. F., Moran, J. M., Ho, P. T. P., & Gottlieb, E. W. 1980, ApJ, 235, 845
Sabin, L., Zijlstra, A. A., & Greaves, J. S. 2007a, in ASP Conf. Ser. 378, Why Galaxies Care About AGB Stars: Their Importance as Actors and Probes, ed. F. Kerschbaum, C. Charbonnel, & R. F. Wing (San Francisco, CA: ASP), 337
Sabin, L., Zijlstra, A. A., & Greaves, J. S. 2007b, MNRAS, 376, 378
Schleuning, D. A. 1998, ApJ, 493, 811
Schleuning, D. A., Vaillancourt, J. E., Hildebrand, R. H., Dowell, C. D., Novak, G., Dotson, J. L., & Davidson, J. A. 2000, ApJ, 535, 913
Schneider, N., Bontemps, S., Simon, R., Jakob, H., Motte, F., Miller, M., Kramer, C., & Stutzki, J. 2006, A&A, 458, 855
Shirley, Y. L., Evans, N. J. II, Young, K. E., Knez, C., & Jaffe, D. T. 2003, ApJS, 149, 375
Shu, F., Najita, J., Ostriker, E., Wilkin, F., Ruden, S., & Lizano, S. 1994, ApJ, 429, 781
Shu, F. H., Adams, F. C., & Lizano, S. 1987, ARA&A, 25, 23
Snell, R. L., Dickman, R. L., & Huang, Y.-L. 1990, ApJ, 352, 139
Sridharan, T. K., Beuther, H., Saito, M., Wyrowski, F., & Schilke, P. 2005, ApJ, 634, L57
Staude, H. J., Lenzen, R., Dyck, H. M., & Schmidt, G. D. 1982, ApJ, 255, 95
Tammann, G. A., & Sandage, A. 1968, ApJ, 151, 825
Tamura, M. 1999, in Proc. of Star Formation 1999, held in Nagoya, Japan, June 21–25, 1999, ed. T. Nakamoto (Nobeyama Radio Observatory), 212
Tamura, M., Hough, J. H., Greaves, J. S., Morino, J. I., Chrysostomou, A., Holland, W. S., & Momose, M. 1999, ApJ, 525, 832
Tomita, Y., Saito, T., & Ohtani, H. 1979, PASJ, 31, 407
Trimble, V. 1973, PASP, 85, 579
Uchida, Y., & Shibata, K. 1985, PASJ, 37, 515
Ungerechts, H., & Thaddeus, P. 1987, ApJS, 63, 645
Vaillancourt, J. E. 2002, ApJS, 142, 53
Vaillancourt, J. E. 2006, PASP, 118, 1340
Vaillancourt, J. E., et al. 2008, ApJ, 679, L25
Vallée, J. P., & Bastien, P. 2000, ApJ, 530, 806
Vallée, J. P., Bastien, P., & Greaves, J. S. 2000, ApJ, 542, 352
Vallée, J. P., & Fiege, J. D. 2005, ApJ, 627, 263
Vallée, J. P., & Fiege, J. D. 2006, ApJ, 636, 332
Vallée, J. P., & Fiege, J. D. 2007a, AJ, 133, 1012
Vallée, J. P., & Fiege, J. D. 2007b, AJ, 134, 628
Vallée, J. P., Greaves, J. S., & Fiege, J. D. 2003, ApJ, 588, 910
Vallée, J. P., & MacLeod, J. M. 1990, ApJ, 358, 183
Walker, M. F. 1956, ApJS, 2, 365
Ward-Thompson, D., Kirk, J. M., Crutcher, R. M., Greaves, J. S., Holland, W. S., & André, P. 2000, ApJ, 537, L135
Ward-Thompson, D., Motte, F., & Andre, P. 1999, MNRAS, 305, 143
Webster, A. S., & Ryle, M. 1976, MNRAS, 175, 95
Wendker, H. J., & Baars, J. W. M. 1974, A&A, 33, 157
Wilking, B. A., Mundy, L. G., Blackwell, J. H., & Howe, J. E. 1989, ApJ, 345, 257
Wolf, S., Launhardt, R., & Henning, T. 2003a, ApJ, 592, 233
Wolf, S., Launhardt, R., & Henning, T. 2004, Ap&SS, 292, 239
Wolf, S., Stecklum, B., Henning, T., Launhardt, R., & Zinnecker, H. 2003b, Proc. SPIE, 4843, 533
Wolf-Chase, G., Moriarty-Schieven, G., Fich, M., & Barsony, M. 2003, MNRAS, 344, 809
Wouterloot, J. G. A., Brand, J., & Fiegle, K. 1993, A&AS, 98, 589
Wu, Y., Zhang, Q., Chen, H., Yang, C., Wei, Y., & Ho, P. T. P. 2005, AJ, 129, 330
Xu, Y., Reid, M.J., Zheng, X.W., & Menten, K.M. 2006, Science, 311, 54
Yang, J., Umemoto, T., Iwata, T., & Fukui, Y. 1991, ApJ, 373, 137
Zemcov, M., Halpern, M., & Pierpaoli, E. 2005, MNRAS, 359, 447
Zijlstra, A. A., van Hoof, P. A. M., & Perley, R. A. 2008, ApJ, 681, 1296
Zinnecker, H., Bastien, P., Arcoragi, J.-P., & Yorke, H. W. 1992, A&A, 265, 726